Micro- and Nano-patterned Gold Structures for Selective Immobilization of Proteins

Vorgelegt von

M.Sc. Manar Arafeh

aus Amman

Von der Fakultät II - Mathematik und Naturwissenschaften

der Technischen Universität Berlin

zur Erlangung des akademischen Grades

Doktor der Naturwissenschaften

Dr. rer. nat.

genehmigte Dissertation

Promotionsausschuss:

Vorsitzender: Prof. Dr. rer. nat. Reinhard Schomäcker

Gutachterin: Prof. Dr. Ir. Marga C. Lensen

Gutachterin: Prof. Dr. Ulla Wollenberger

Tag der wissenschaftlichen Aussprache: 25. March 2014

Berlin 2014

D 83

Table of Contents

List of abbreviations

AcI: acetyl chloride

AFM: atomic force microscope

$AgNO_3$: silver nitrate

Ag NPs: silver nanoparticles

amu: atomic mass unit

Au NPs: gold nanoparticles

BCM: block copolymer micelle

$CDCl_3$: deuterated chloroform

CDI: carbonyldiimidazolide

CH_2Cl_2: dichloromethane

^{13}C NMR: carbon-13 nuclear magnetic resonance

CTAB: cetyltrimethylammonium bromide

1D: one dimensional

2D: two dimensional

3D: three dimensional

D: translational diffusion coefficient

d: doublet

DCC: N,N′-Dicyclohexylcarbodiimide

DCM: dichloromethane

d(H): hydrodynamic radius

DLS: dynamic light scattering

DMAP: dimethylaminopyridine

DMF: dimethylformamide

DNA: deoxyribonucleic acid

E: Young's Modulus

EDTA: ethylenediaminetetraacetate

EDX: energy-dispersive X-ray diffraction

EG: ethylene glycol

FIMIC: fill molding in capillaries

FLIM: fluorescence lifetime imaging microscopy

FRET: Förster resonance energy transfer

G': Storage Modulus

GFP: green fluorescent proteins

$HAuCl_4.3H_2O$: gold (III) chloride trihydrate

HCl: hydrochloric acid

His-tag proteins: hexahistidine-tag proteins

^{1}H NMR: proton nuclear magnetic resonance

HOAc: acetic acid

HOMO: highest occupied molecular orbital

Hz: Hertz

IC: internal conversion

IR: infrared radiation

ISC: intersystem crossing

J: coupling constant

k: Boltzmann's constant

kf: fluorescence rate constant

LSPR: localized surface plasmon resonance

LUMO: lowest unoccupied molecular orbital

m: multiplet

$MgSO_4$: magnesium sulfate

Mwt: molecular weight

$NaBH_4$: sodium bronium hydride

NaCl: sodium chloride

NaOH: sodium hydroxide

Near IR: near infrared

NH_2NH_2: hydrazine

$NH_2OH.HCl$: hydroxylamine hydrochloride

$NiCl_2$: nickel chloride

NMR: nuclear magnetic resonance

NPs: nanoparticles

NTA: nitrilotriacetic acid

PDMS: polydimethylsiloxane

PEG: polyethylene glycol

PET: photoinduced electron transfer

PI: photoinitiator

PS-b-P2VP: polystyrene-block-poly(2-vinyl pyridine)

PVA: polyvinyl alcohol

PVP: polyvinyl pyrrolidone

Redox proteins: reductive oxidative proteins

RET: resonance energy transfer

s: singlet

SAMs: self-assembled monolayer

SAXS: small-angle X-ray scattering

SEM: scanning electron microscope

Si-Au NPs: gold nanoparticles on silicon substrate

$SOCl_2$: thionyl chloride

SPR: surface plasmon resonance

T: temperature

t: triplet

τ: lifetime

TEG: triethylene glycol

TEM: transmission electron microscope

UV-Vis: Ultra violet – visible

Zn: zinc

μCP: micro-contact printing

η: viscosity of the solution

γ: deformation value

δ: chemical shift

Φ: quantum yield

Scope and Organization of the Thesis

Concept of the project: Protein immobilization through cofactor assembly on gold surfaces

The aim of this study is twofold: 1) The fabrication of gold nanostructures with patterned surfaces, defined nanoparticle size, shape, and separation between the nanoparticles for proteins immobilization. 2) The creation of a model that is based on linker molecules with dual functionalities The function on one side is selective binding to gold nanoparticles patterned onto two dimensional substrates, and on the other, specific binding to biofunctional molecules. An illustration of the concept in biofunctional molecules immobilization strategy is shown in Figure 1.

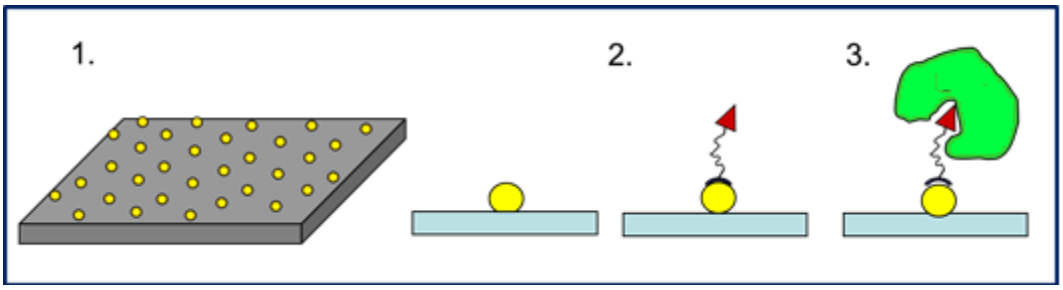

Figure 1: Biofunctional molecules immobilization onto patterned gold nanostructures

The first challenge we must face throughout the course of this study is the optimization of patterning techniques in order to achieve certain control over nanoparticle size, shape and interparticle distance. Additionally, the development of new techniques to pattern gold nanoparticles in a micro-pattern will also present difficulty. A third challenge is manipulating the support matrix or background substrate to cover a wide range of substrates, from hard inorganic silicon to soft polymeric hydrogel.

We are also going to construct a fluorescein-based model system to be immobilized onto our patterned gold nanoparticles. The model composed of fluorescein molecule will perform as an example of biofunctional molecules possessing fluorophore in their structures and accompanied by a specific linker molecule. The linker has the ability to bind itself to gold nanostructures from one side as well as the complement functionality to immobilize certain biofunctional molecules from the other side.

Accordingly, arrays of patterned gold nanoparticles on 2D substrate (silicon or polyethylene glycol hydrogel) with well-defined size, shape and position will be prepared. Nanoparticles serve as anchoring points, or specific immobilization sites, for the immobilization process, as well as offering a high surface area, which is crucial in increasing the loading capacity of the substrate and therefore the loading capacity of the biofunctional molecules. Spacers with adjustable length are used to position the protein with the proper orientation away from the surface and towards the solution in order to retain the accessibility of the active site. This positioning avoids losing the activity of the protein and achieving optimal performance for the intended application. The functionality of both sides of the spacer are also adjusted to have selectivity for the conjugation reaction to gold nanoparticle surface, as well as the specificity to bind itself to the receptor biomolecule from the other side through site-specific interaction.[16]

In summary, the ultimate aim of this research is to construct a model for enzyme immobilization to control the specific orientation of the enzyme in such a way that its particular performance is retained and which fits a specific application. The aim is to create uniformly oriented proteins on 2D-nanopatterned gold nanoparticles with an array in which their catalytic efficiency and stability will be maintained.

The outline of this thesis is as follows:

Chapter 1 focuses on a general introduction to the main topic of biofunctional molecules immobilization. Discussion is included of the various immobilization strategies that have been reported and a brief description of the main advantages and drawbacks accompanying each method. Other related aspects are presented such as the idea behind the conjugation strategy based on ligand-receptor binding, as well as some parameters influencing biofunctional molecules binding to gold nanostructures.

Chapter 2 will introduce the wet chemical synthesis of different morphologies of metal nanostructures and the subsequent characterization with a brief discussion of their main physical and chemical properties. Additionally, the relationship between size and shape variations of metal nanoparticles and their biofunctionalization will be clarified as well.

Chapter 3 will focus on optimizing the different parameters for a number of patterning strategies for nanostructures onto silicon substrate in order to achieve control over size, position and interparticle space.

Chapter 4 introduces the extension of the patterning concept of gold nanostructures, which was performed on silicon substrate, to be applied on polymer substrates composed of polyethylene glycol hydrogel.

Chapter 5 involves a model system of fluorescein-based dye acting as a biofunctional molecule for immobilization onto patterned gold nanoparticles on the substrates through a well-designed linker molecule.

Chapter 6 summarizes our main achievements and addresses our future outlook in extending the work of this project by applying our techniques in nanoparticle patterning to immobilize biomolecules such as green fluorescent proteins.

Chapter 1

General introduction

A general introduction is given in this chapter in order to provide background information about the aspects related to the topic of the research at hand. We will start by identifying the main scope of this work in biofunctional molecules immobilization, then we will provide a brief overview of the main immobilization strategies that have been reported with a short discussion of their advantages and limitations. Furthermore, we will attempt to set up a general frame for the project through both short and long term objectives. We will therefore highlight the potential value of our model in immobilizing biofunctional molecules in order to overcome the current limitations associated with immobilization strategies.

1. Aim of the project: immobilization of biofunctional molecules

1.1 Immobilization of Proteins

Protein or enzyme immobilization has witnessed great progress during the second half of last century thanks to specific features of enzymes used as biological catalysts. Such features include high activity, selectivity and specificity, in addition to the mild reaction conditions required in the application processes to achieve the desired performance of enzymes, which enables them to be applied in the manufacturing of a huge number of products.[1,2]

Protein immobilization is defined as: the localization or fixation of proteins on a defined position on a substrate in such way that its catalytic activity is retained.[3]

In general, the driving forces behind protein immobilization vary according to the intended use of that protein. Some proteins are immobilized for stabilization purposes, or with the intention of recovery once the reaction is complete. This is particularly useful in cases of catalytic enzymes, which might be intended for repeated reuse, thus achieving a longer half-life, less degradation in the reaction environment and a highly purified product, as well as reduction in the economic cost.[4–7]

1.2 Different approaches to protein immobilization

Immobilized enzyme systems consist primarily of enzyme, support and the mode of binding through which the enzyme is fixed to the support.

Support material is classified into organic and inorganic categories. Organic supports are mainly polymers, which are then further divided into natural polymers, such as cellulose and synthetic ones, such as polystyrene. On the other hand, inorganic supports can be also classified as natural minerals, such as silica and synthetic or processed materials, like glass and silicon wafer.[2,4]

In order to achieve the best performance in enzyme immobilization, support material should possess a number of characteristics; it should be inert, strong and have the ability to increase enzyme specificity and/or activity.[4] Furthermore, it should have the required capacity to achieve higher loading of the immobilized enzyme.[8]

Both physical and chemical properties of support material, such as degree of hydrophilicity and hydrophobicity, binding chemistry or charge, strongly influence the catalytic properties of the enzyme, such as stability and activity.[9]

Approaches toward enzymes immobilization are classified according to the mode of interaction between the support material and the enzyme. There are four main modes of interaction used for immobilization process: adsorption, covalent binding, entrapment and crosslinking.

- **Adsorption:** this method is the simplest for immobilization, since it depends on the physical interaction between the support material and the enzyme. This interaction is either hydrophobic or ionic, based on charge-charge interaction. Some characteristics of this type of interaction are its reversibility, simplicity and cheapness,[10] as indicated by Figure 2. However, its main limitation is the risk that the enzyme may detach from the support and go into the solution.[6,11] Moreover, adsorption of the enzyme to the support is highly influenced by the protein's environment, such as pH, ionic strength and proteins pI.[12]

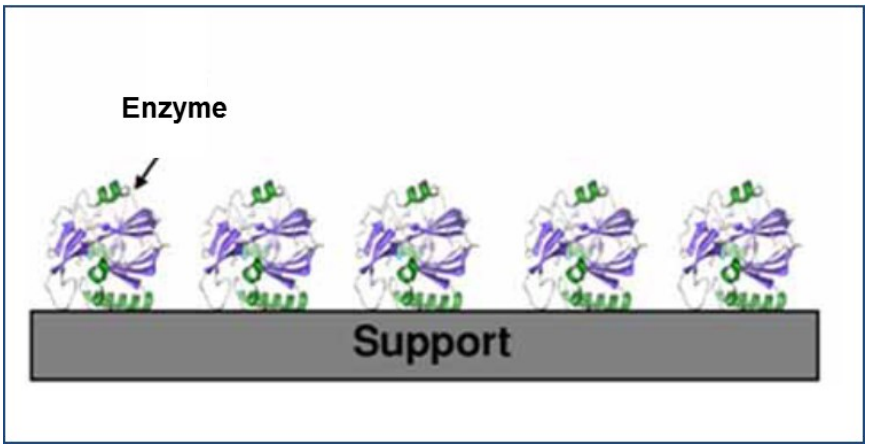

Figure 2: Schematic representation of physical adsorption of enzymes onto a support material[6]

- Covalent binding: this kind of interaction is a strong, stable and irreversible interaction,[13] which is advantageous because the immobilized enzyme cannot be released into the solution,[5] therefore guaranteeing the absence of the enzyme in the product solution. Furthermore, due to the strong interaction that binds the enzyme to the support, the enzyme is stabilized, an issue in many cases. However, disadvantages can also arise from this mode of interaction, such as a reduction in the activity of the enzyme as a consequence of its strong, covalent binding to the support. Three factors affect enzyme activity through its covalent binding modes: the

number of bonds involved in the covalent binding, the position and the nature of that bond.[2] Due to the covalent nature of the link between the immobilized enzyme and the support, the whole system must be discarded as soon as the activity of the enzyme decreases, resulting in economical loss Figure 3 illustrates this type of enzyme immobilization.

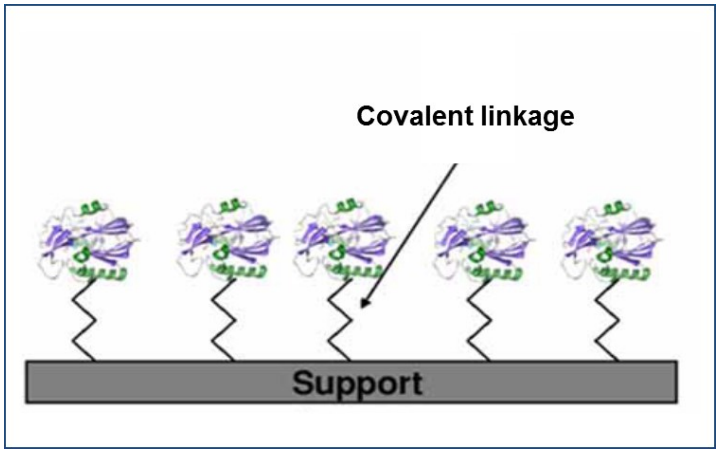

Figure 3: Enzyme immobilization onto support material through covalent binding[6]

- Entrapment: this method of enzyme immobilization concerns physical or non-physical confinement of the enzyme within a polymeric matrix, which both substrate and product can permeate, but which is impermeable to the enzyme. The polymer matrix can be composed of a natural material, such as starch, or it can be synthetic, such as polyvinyl alcohol (PVP). This method provides a good separation between the enzyme and the product. The main disadvantage of this method is the mass transfer limitation of substrate/analyte through the polymer matrix.[6] Other disadvantages are easy leakage and lower loading than other immobilized enzymes.[10] Drawbacks result out of entrapment technique can be solved using pre- and post- immobilization strategies in order to prolong the half-life of the immobilized enzyme, preventing the total loss of the enzyme, and avoiding decrease in enzyme's activity[14,15]. Figure 4 shows this type of enzyme immobilization.

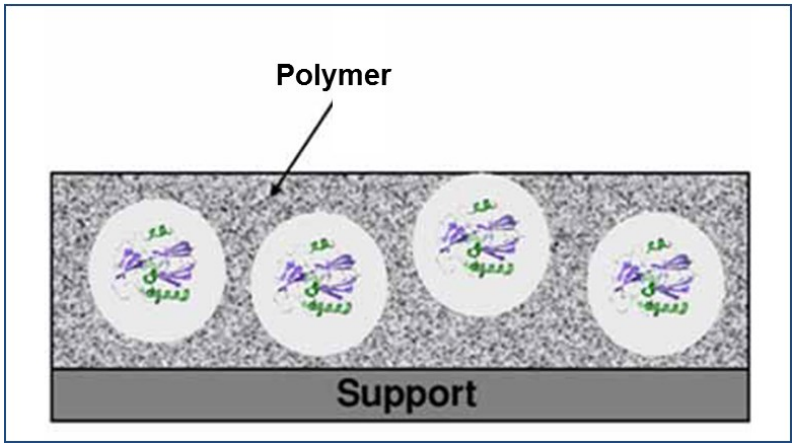

Figure 4: Enzyme immobilization onto support by entrapment[6]

- Membrane confinement or encapsulation: The main advantage of this method lies in its ability to protect the enzyme from the external environment. The disadvantage is its mass transfer limitation.[10,11] Membrane confinement or encapsulation can also be considered as a subcategory of the entrapment method (see above). See Figure 5 for this mode of immobilization.

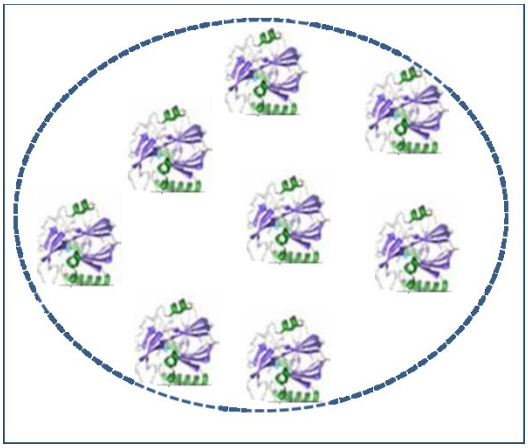

Figure 5: Membrane encapsulation of enzyme as a mode of immobilization (adapted from ref[10]***)***

- Crosslinking: This mode of interaction involves crosslinking of the enzyme on films or membranes to avoid enzyme leakage into the substrate solution.[6] See Figure 6.

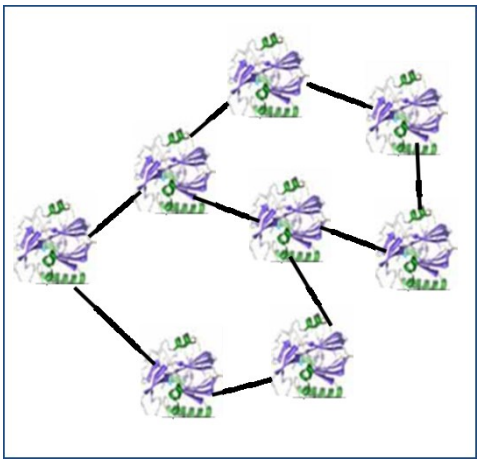

Figure 6: Enzymes molecules crosslinking as a mode of enzyme immobilization (adapted from ref[3])

In general, the main challenge is to select the appropriate immobilization approach that corresponds well to the intended enzyme function and/or to the desired application. The ultimate aim of enzymes immobilization is to improve their activity, stability and selectivity, an aim that is reached by choosing the suitable immobilization method.[2] Additional challenges and limitations arise as consequences of the immobilization process, such as a reduction in the biological activity of the protein. This reduction can result due to the random orientation of the immobilized protein over the support matrix that influences the protein's active site.[16]

1.3 Self-assembled monolayer (SAMs) of biofunctional molecules onto surfaces

(SAMs) of biofunctional molecules onto surfaces represent an excellent approach to the immobilization of proteins on a variety of surfaces, allowing immobilization at a molecular level. This strategy is highly attractive due to its simplicity and flexibility, as well as its ability to tailor the functionality of the end groups, which compose the organic film on the surface and can be adjusted for specific protein's immobilization.[16]

1.4 Protein immobilization with nanostructures

Due to the rapid progress in nanotechnology in the last few decades, nanostructures perform excellently as support material,[17,18] solving issues related to enzyme immobilization. These issues include mass transfer limitation in addition to some general properties of nanostructures, such as a high surface area to volume ratio. Sub categories of this type of immobilization are the same as those of other well-known immobilization techniques:

- Non-specific immobilization: including techniques such as adsorption, non-specific covalent binding entrapment and encapsulation.

- Specific immobilization; these methods are also subdivided into non-covalent and covalent immobilization. Specific non-covalent immobilization, which will be our tool in this project (see section 2 of this chapter), utilizes the specific stable interaction, for example between polyhistidine and bivalent metal, such as Ni^{2+}. Specific covalent immobilization also includes a number of methods, such as click reaction and covalent ligation immobilization through Cysteine residues.[19]

1.5 Protein immobilization onto metal nanostructures

Metal nanostructures have been recognized as useful platforms for biofunctional molecules immobilization. However, the nonspecific mode of immobilization through hydrophobic and electrostatic interaction may be problematic, since this kind of weak physical interaction can lead to protein leaching inside the solution (as previously described). Nevertheless, the attractive physical and chemical properties of gold and silver nanostructures, including electron conductivity and large surface area, make them excellent candidates for the immobilization of redox enzymes, among other applications.[20] Moreover, metal nanoparticles show specific reactivity with the sulfanyl functional group, forming a strong covalent bond between the metal surface and the sulfanyl group. Furthermore, gold shows resistance to oxidation alongside and has localized surface plasmon resonance (LSPR) that can be implemented as a monitor for molecular binding through its position shift.[21] In another words, metal nanoparticles surfaces are considered to be “transducers” for molecular binding.[22] Metal nanostructures form successful site-specific points for protein immobilization, which allows a high degree of control in the nanoscale.[23]

2. Heterogeneous catalysis and bioelectrocatalysis

Studying the mechanism by which electrons directly transfer between redox proteins and the surface of the electrode has caught the attention of many researchers. This topic is so attractive because it could provide useful information about electronic paths inside biological systems, as well as having many applications in the biotechnological research field, including biosensors, bioreactors and bio-fuel cells.[24,25]

The major challenge that arises is that the rate of electron transfer between redox proteins and the electrode surface is slow and difficult to detect.[26] Detection proves problematic because the redox centers of such proteins are hidden inside their structures,[27] leading to a lack of fundamental information about many of the biological processes that depend on electron transfer.[24,26]

To solve this issue, effort must be focused towards finding a suitable approach for the immobilization of these biofunctional molecules onto the electrode surface. The optimal immobilization approach must satisfy a number of requirements, including the prevention of protein crowding on the surface, which can then lead to inaccessible active sites. The approach must also involve general properties of the electrode material helping to detect the electrical current resulting from redox processes.[8] Furthermore, using an appropriately functionalized linker between the protein and the electrode surface could enhance conductivity between the redox proteins and the electrode surface, while retaining the biofunctionality of the proteins in a well-oriented molecular structure.[28]

A suitable immobilization approach should satisfy a number of criteria to allow direct electron transfer between redox proteins and the surface of the electrode. The active site should be positioned in a way that can enhance electron transfer. Moreover, the ideal close-packed monolayer arrangement of the enzyme should be achieved.[11]

The immobilization strategies, which were previously described as general immobilization techniques for proteins and enzymes, can also be applied here. The application in this case would be the immobilization of redox proteins to the electrode surface, considering the potential advantages and disadvantages for each method, this kind of protein must also transfer electrons to the electrodes surface, making some immobilization strategies more advantageous than others. For example,

another possible limitation of the entrapment or encapsulation strategies is the physical separation between the protein and the surface of the electrode caused by the impedance of the protein inside an isolating membrane or polymer matrix. This impedance results in the reduction of protein activity due to the retardation of the electronic current between the enzyme and the electrode surface.

Further immobilization strategies for redox proteins can be implemented by the formation of a self-assembled monolayer (SAM) of alkane thiol on gold surface. This monolayer creates a high affinity between (–SH) moiety in alkane thiol and the gold surface, followed by the functionalization of the head group of alkane thiol using different functionalities to achieve different polarities. Hydrophobicity and charge serve as anchoring points for different enzyme immobilization via non-covalent hydrophilic, hydrophobic or electrostatic interactions between the alkane thiol monolayer and the enzyme.

It is worth mentioning that the nature of alkane thiol head groups would influence the surface properties of the gold electrode and therefore, electron transfer. It is then necessary to optimize those parameters in order to achieve efficient electron transfer reactions.[29]

In general, the immobilization strategy should be designed in order to enhance catalytic activity as well as the stability of redox proteins, fitting with the special requirement of redox proteins for electron transfer. In other words, the strategy should increase the efficiency of the electronic current between the enzyme and the electrode's surface.

3. Conjugation strategy, ligand receptor binding and cofactor reconstitution

Choosing the optimal conjugation strategy, which must fit with certain biomolecules to achieve the desired application, is crucial. The driving force behind this choice should be the ease for creating such a conjugation and its stability during the application process.[30]

The conjugation strategy which will be employed in this project takes advantage of the metal-ligand affinity interaction between (Ni-NTA) and Hexahistidine-tag (His-tag). The strategy therefore uses Ni^{2+} as a bivalent metal ion to create non-covalent, site specific conjugation between Ni-NTA from one side and Histag proteins from the other.[31,32]

His-tagged proteins with six consecutive histidine moieties are very popular due to their reversible binding, high affinity, stability and specificity as a chelating agent for Ni-NTA, in addition to their potential to complete ″oriented-attachment″ without affecting the protein's activity.[31–33]

Nitrilotriacetic acid (NTA) is a tetradentate ligand which is commonly used in selective purification as well as in immobilization of His-tagged proteins.[34]

Binding of His-tag proteins to NTA, facilitated by Ni^{2+} will take place by means of an octahedral complex formation between one molecule of NTA-ligand and two histidine residues of His-tagged protein in order to occupy all the six coordination sites of Ni(II) ion.[32,35] Dissociation of this complex can be achieved by adding a competitor ligand such as imidazole or ethylenediaminetetraacetate (EDTA).[33,35]

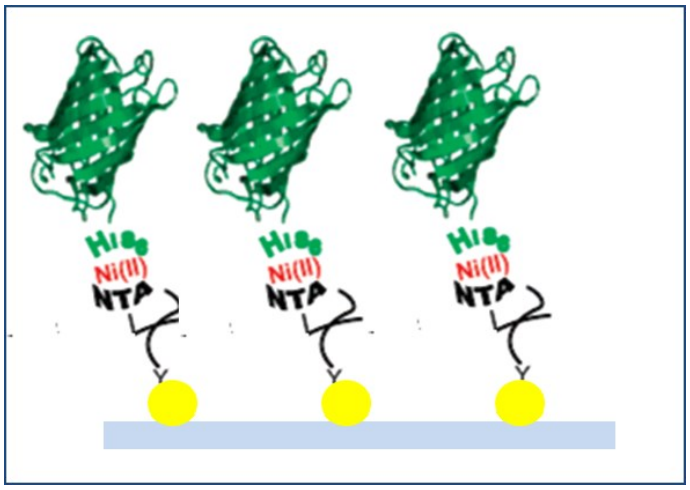

Figure 7 NTA-Histagged proteins immobilized onto gold nanostructures (adapted from ref[36])

NTA functionalized by thiol functionality is used to anchor proteins to the gold surface where NTA itself resides at the end of the spacer for being more accessible to His-tag proteins. NTA molecule will then chelate to the metal center thus providing ligands for his-tag proteins.[37] Figure 7 illustrates the principle.

4. Biofunctional molecules on gold surface

Surface biofunctionalization constitutes the basis for diverse applications in both biology and material science, and is experiencing an increase in the number of studies related to the field.[38] The surface of gold nanoparticles is widely used for biofunctionalization since it can be ″easily and efficiently modified″.[39]

In the scope of this study, gold surface functionalization is an important step in achieving the final aim of protein immobilization. A number of parameters play a role in this regard, and will be discussed in more detail in the following chapters.

4.1 Effects of density gradient (or surface density) on the immobilized biofunctional molecules

Surface density will be obtained by dividing the amount of immobilized biofunctional molecules by the apparent surface area of the substrate.[40]

Better control over density gradient of the biofunctional molecules on the gold nanoparticles could be achieved by increasing the amount of available binding sites (nanoparticles) per surface area unit. The surface area able to be occupied by immobilized proteins can in turn be enhanced by decreasing the spaces between the nanoparticles.

4.2 Effects of the nanoparticle size

Size control of gold nanoparticles acting as binding sites for immobilization will influence the number of ligands or linker molecules existing on each site (nanoparticle). Therefore, to ensure that there is only one single biofunctional molecule occupying each binding site, control over the size of the particle must be exercised.[41] The resulting particle size should be comparable to the size of the biofunctional molecule.

4.3 Effects of the shape of the nanoparticles

Biofunctionalization of gold nanoparticles with non-spherical shapes has an effect on the chemical environment expressed by change in the dielectric constant, which in turn has a strong effect on the localized surface plasmon resonance (LSPR) peak position.[39] (Details are given in **chapter 2**)

4.4 Effects of the chemistry of the biofunctionality bound to the nanoparticles

There are a number of chemical functionalities which show high affinity and selective binding to gold nanoparticles. (–SH) functionality is the most popular, due its ability to form a strong covalent interaction between the gold surface on one side and the biofunctional molecule on the other. Conversely, primary amine (-NH_2) possesses the weakest interaction between biofunctional molecules and the gold surface.[42] There are other functionalities with a high affinity towards the gold surface interaction, such as sulfide (-S-) and disulfide (-S-S-) moieties. The interaction between both (-S-) and (-S-S-) to gold surface is weaker comparing to (-SH) functionality but stronger than amines (-NH_2).

4.5 Stability of the biofunctional molecules on gold nanoparticles

The retention of the biofunctional activity of immobilized biofunctional molecules on the gold surface is considered to be an important requirement of the immobilization process. This includes their ability to couple with their ″complementary binding partners″. This coupling requires a rational and careful design for the spacer molecule as well as for the immobilizing surface in order to give the immobilized biofunctional molecules the required orientation to get the needed accessibility of their active sites.[43]

4.6 Effect of introducing a linker molecule

An appropriate linker molecule must have dual functionality, that of selective binding to the gold surface from one side and of specific binding or anchoring of biofunctional molecule from the other side. Such a linker molecule has a strong effect on the spatial orientation of the protein (see below). On the other hand, it can also prevent direct biomolecule-surface interaction, which can affect the stability of the protein.[44] (stability of biofunctional molecules discussion above)

4.7 Spatial orientation of the biofunctional molecules

This requirement implies that the spacer head group should have good accessibility for binding to its complementary biofunctional molecule.[37] Moreover, the protein's spatial orientation in the application environment should be controlled in such way that its active site is exposed to the application environment, thus avoiding loss of its

biofunctionality. This can be achieved by employing a linker molecule between the protein and the immobilizing surface in order to give the immobilized biofunctional molecule a measure of flexibility.[28]

4.8 Coverage of the biofunctional molecules

The word coverage means the ratio of bound biofunctional molecules to the available binding sites. Theoretically, 100% is an achievable full monolayer coverage percent, indicating that the binding sites on the surface are fully occupied by biofunctional molecules. Coverage less than 100% indicates that the bound molecules couldn't form a complete monolayer.[45]

Several factors have an influence on the degree of saturation of the bound biofunctional molecules. These factors are the concentration of the adsorbed molecules (the higher the concentration, the greater the coverage), and the size and flexibility of the adsorbed molecules (The larger the size and higher the flexibility, the greater the coverage).[43]

4.9 Spacing between the biofunctional molecules

The control of this parameter is important in order to minimize steric and electrostatic hindrance between biofunctional molecules, caused by the crowding effect.[43] With minimal steric and electrostatic hindrance, better orientation for the biofunctional molecules is also achieved, in turn making their active sites more accessible for specific binding.

4.10 Crowding effect

Clustered biomolecules on the surface will decrease binding site accessibility, therefore inactivating further biomolecules due to steric hindrance effect.[45]

5. Bibliography

(1) Nisha, S.; Arun Karthick, S.; Gobi, N. *Chem. Sci. Rev. Lett.* **2012**, *1*, 148–155.

(2) Cao, L. In *Carrier-bound Immobilized Enzymes: Principles, Application and Design*; WILEY-VCH Verlag GmbH & Co. KGaA: Weinheim, **2005**; pp. 1–37.

(3) Brena, B. M.; Batista-Viera, F. In *Methods in Biotechnology: Immobilization of Enzymes and Cells*; Guisan, J. M., Ed.; Humana Press Inc.: Totowa, **2006**; Vol. 1051, pp. 15–30.

(4) Datta, S.; Christena, L. R.; Rani, Y.; Rajaram, S. *Biotechnology* **2013**, *3*, 1–9.

(5) Torres-salas, P.; Monte-martinez, A.; Cutiño-avila, B.; Rodriguez-colinas, B.; Alcalde, M.; Ballesteros, A. O.; Plou, F. J. *Adv. Mater.* **2011**, *23*, 5275–5282.

(6) Spahn, C.; Minteer, S. D. *Recent Patents Eng.* **2008**, *2*, 195–200.

(7) Meena, K.; Raja, T. K. *Indian J. Biotechnol.* **2004**, *3*, 606–608.

(8) Frasca, S.; Von Graberg, T.; Feng, J.; Thomas, A.; Smarsly, B. M.; Weidinger, I. M.; Scheller, F. W.; Hildebrandt, P.; Wollenberger, U. *ChemCatChem* **2010**, *2*, 839–845.

(9) Hinberg, I.; Kapoulas, A.; Korus, R.; O'Driscoll, K. *Biotechnol. Bioeng.* **1974**, *XVI*, 159–168.

(10) Fernández-fernández, M.; Sanromán, M. Á.; Moldes, D. *Biotechnol. Adv.* **2012**.

(11) Betancor, L.; Johnson, G. R.; Luckarift, H. R. *ChemCatChem* **2013**, *5*, 46–60.

(12) James, A. E.; Driskell, J. D. *Analyst* **2013**, *138*, 1212–1218.

(13) Hong, J.; Xu, D.; Gong, P.; Yu, J.; Ma, H.; Yao, S. *Microporous Mesoporous Mater.* **2008**, *109*, 470–477.

(14) Akgol, S.; Kacar, Y.; Denizli, A.; Arica, M. *Food Chem.* **2001**, *74*, 281–288.

(15) Wilson, L.; Illanes, A.; Pessela, B.; Abian, O.; Fernandez-Lafuente, R.; Guisan, J. *Biotechnol Bioeng* **2004**, *86*, 558–562.

(16) Tan, Y. H.; Pandey, B.; Sharma, A.; Bhattarai, J.; Stine, K. J. *Glob. J. Biochem.* **2012**, *3*, 1–21.

(17) Siqueira Jr., J. R.; Caseli, L.; Crespilho, F. N.; Zucolotto, V.; Oliveira Jr., O. N. *Biosens. Bioelectron.* **2010**, *25*, 1254–1263.

(18) Tan, Y. H.; Liu, M.; Nolting, B.; Go, J. G.; Gervay-hague, J.; Liu, G. *ACS Nano* **2008**, *2*, 2374–2384.

(19) Liu, W.; Wang, L.; Jiang, R. *Top. Catal.* **2012**, *55*, 1146–1156.

(20) Petkova, G. A.; Záruba, K.; Žvátora, P.; Král, V. *Nanoscale Res. Lett.* **2012**, *7*, 287–296.

(21) Yoshimoto, K.; Hirase, T.; Nemoto, S.; Hatta, T.; Nagasaki, Y. *Langmuir* **2008**, *24*, 9623–9629.

(22) Mercier, D.; Boujday, S.; Annabi, C.; Villanneau, R.; Pradier, C.; Proust, A. *J. Phys. Chem. C* **2012**, *116*, 13217–13224.

(23) Peissker, T.; Deschaume, O.; Rand, D. R.; Boyen, G.; Conard, T.; Van Bael, M. J.; Bartic, C. *Langmuir* **2013**.

(24) Saadati, S.; Salimi, A.; Hallaj, R.; Rostami, A. *Anal. Chim. Acta* **2012**, *753*, 32–41.

(25) Kamitaka, Y.; Tsujimura, S.; Kataoka, K.; Sakurai, T.; Ikeda, T.; Kano, K. *J. Electroanal. Chem.* **2007**, *601*, 119–124.

(26) Tominaga, M.; Nomura, S.; Taniguchi, I. *Electrochem. commun.* **2008**, *10*, 888–890.

(27) Spricigo, R.; Dronov, R.; Rajagopalan, K. V.; Lisdat, F.; Leimkühler, S.; Scheller, F. W.; Wollenberger, U. *Soft Matter* **2008**, *4*, 972–978.

(28) Baldacchini, C.; Herrero Chamorro, M. A.; Prato, M.; Cannistraro, S. *Adv. Funct. Mater.* **2011**, *21*, 153–157.

(29) Ferapontova, E. E.; Ruzgas, T.; Gorton, L. *Anal. Chem.* **2003**, *75*, 4841–4850.

(30) Kalia, J.; Raines, R. T. *Curr. Org. Chem.* **2010**, *14*, 138–147.

(31) Shimada, J.; Maruyama, T.; Kitaoka, M.; Kamiya, N.; Goto, M. *Anal. Biochem.* **2012**, *421*, 541–546.

(32) De, M.; Rana, S.; Rotello, V. M. *Macromol. Biosci.* **2009**, *9*, 174–178.

(33) Chen, Y.; Chen, C.; Hung, Y.; Chou, C.; Liu, T.; Liang, M.; Chen, C.; Mou, C. *J. Am. Chem. Soc.* **2013**, *135*, 1516–1523.

(34) Abdul Kadir, M.; Park, J.; Lee, J.; Lee, C.; Lee, S. H.; Lee, S.; Paik, H. *Macromol. Chem. Phys.* **2013**, *214*, 2027–2035.

(35) Niemeyer, C. M. *Angew. Chem. Int. Ed. Engl.* **2010**, *49*, 1200–1216.

(36) Huang, G.; Endrizzi, B. J.; Hlady, V.; Stewart, R. J. *Macromolecules* **2008**, *41*, 448–452.

(37) Lukac, R.; Kauerova, Z.; Masek, J.; Bartheldyova, E.; Kulich, P.; Koudelka, S.; Korvasova, Z.; Plockova, J.; Papousek, F.; Kolar, F.; Schmidt, R.; Turanek, J. *Langmuir* **2011**, *27*, 4829–4837.

(38) Zhang, X.; Tretjakov, A.; Hovestaedt, M.; Sun, G.; Syritski, V.; Reut, J.; Volkmer, R.; Hinrichs, K.; Rappich, J. *Acta Biomater.* **2013**, *9*, 5838–5844.

(39) Wang, B. C.; Ma, Z.; Wang, T.; Su, Z. *Adv. Funct. Mater.* **2006**, *16*, 1673–1678.

(40) Son, K. J.; Ahn, S. H.; Kim, J. H.; Koh, W. *ACS Appl. Mater. Interfaces* **2011**, *3*, 573–581.

(41) Arnold, M.; Schwieder, M.; Blümmel, J.; Cavalcanti-adam, E. A.; Lopez-Garcia, M.; Kessler, H.; Geiger, B.; Spatz, J. P. *Soft Matter* **2009**, *5*, 72–77.

(42) Kim, H. J.; Kwon, S.; Kim, K. *Electrochem. commun.* **2012**, *20*, 52–55.

(43) Schlapak, R.; Danzberger, J.; Armitage, D.; Morgan, D.; Ebner, A.; Hinterdorfer, P.; Pollheimer, P.; Gruber, H. J.; Schäffler, F.; Howorka, S. *Small* **2012**, *8*, 89–97.

(44) Caiazzo, M.; Alessandrini, A.; Facci, P. *ACS Appl. Mater. Interfaces* **2009**, *1*, 514–518.

(45) Ihalainen, P.; Peltonen, J. *Sensors Actuators B* **2004**, *102*, 207–218.

Chapter 2

Synthesis of multiple shapes and sizes of gold and silver nanoparticles

A series of different shapes and sizes of gold and silver nanoparticles has been synthesized in order to provide a diverse tool box to pattern them on different types of substrates. These substrates range from hard inorganic silicon to soft polymeric polyethylene glycol hydrogel, thus developing a wide variety of templates with controlled nanoparticle type, size, shape and position for proteins immobilization.

1. Introduction

1.1 Nanotechnology and nanoparticles in history

Nanotechnology is considered to be relatively new science applying physical, chemical and biological concepts, which have been observed in macroscale systems, to the manipulation and engineering of matter on a small scale. This scale ranges from single atoms or molecules to submicron dimensions (i.e, nanoscale regime)[1]. Many of organizations including IUPAC define nanoparticles as being particles with a diameter of 1-100 nm[2,3]

Suspension of metal nanoparticles (gold and silver nanoparticles) has been employed since middle ages in stained glass, painted ceramics and forged steel[2,4]. The intense ruby red color produced by gold and the deep yellow from silver nanoparticles were valued as painting agents.

The first documented use of the synthesis of gold colloids was recorded by Michael Faraday in 1857[5] and the first book on colloidal gold was published in 1618 by F. Antonii. presented data describing how to create colloidal gold and its medicinal applications,[6] however, the basis of nanotechnology as a modern science was truly formed after 1959, as a consequence of Richard Feynman's talk "There's Plenty of Room at the Bottom." This talk took place in late 1959 at the annual meeting of the American Physical Society when Feynman pointed out "the problem in controlling and manipulating things on a small scale"[7]. Feynman's talk is considered an important turning point in research concerning engineering and manipulating objects at the nanoscale. He directed the attention of the research community toward the possibility of working on small scale and brought to light the value of investing research efforts in this field. This redirection of attention and investment would highly influence and serve other fields such as biology, chemistry and computer science.

1.2 Properties and applications of gold and silver metal nanoparticles

Despite being a young science, nanotechnology has witnessed rapid progress in thousands of studies related to nanoparticles research in general, and metal nanoparticles in particular. (the focus of this study). Metal nanoparticles, due to their physical, chemical and biological properties, which differ significantly from their bulk material, are highly influenced by size and shape[8–11].

One of the most interesting properties of metal nanoparticles related to an optical property results due to their localized surface plasmon resonance (LSPR). LSPR originates from the excitation of electrons near the surface of the metal stimulated by an external source leading to resonance coupling of the stimuli wavelength. The collective oscillations of the conducting electrons exhibit an absorption plasmon peak in the visible to near IR region.[12,13] This plasmon peak is responsible for the observed intense color of metal nanoparticles, observed in stained glass and painted pottery.[4] Accordingly, colors ranging from violet to red appear for silver as well as gold nanoparticles,[11] depending on the position of their plasmon peak in the spectrum. The position of the plasmon peak is sensitive to the particle size, shape and metal composition as well as to the surrounding medium refractive index.[10,14–16]

It is of great importance to tune LSPR absorption peak of metal nanoparticles to near IR region "therapeutic optical window" where the maximum transmission of human tissue is. This achievement would be of high value for both therapeutic and imaging applications in tissue.[10]

As a consequence of the fascinating properties of metal nanoparticles, they possess a wide spectrum of applications ranging from use in cancer therapy,[8,17]plasmonic applications[18] (such as surface enhanced Raman spectroscopy),[19,20] catalysis,[21,22] sensing and biomedical imaging techniques,[14] in addition to use in drug delivery and photothermal therapy.[23]

1.3 Synthetic approaches for metal nanoparticles

The rapid development of the synthetic methods for metal nanoparticle fabrication allows a high degree of control over size, shape and dispersing medium. The most popular current synthetic protocols for shape and size control involve physical methods such as laser ablation,[24,25] proton beam irradiation[26] and ultrasonic irradiation.[27] Also popular are biological methods from either plant resources[28,29] or biological organisms,[30] in addition to the classical method of chemical reactions or "wet chemical synthesis".[31,32] Wet chemical synthesis offers a method in which nanoparticles can be produced in large amounts, and where no special or expensive equipment is needed[33]. However, polydisperse sizes and shapes can be produced, which have side effects in decreasing the yield of the intended morphology as well as broadening the LSPR peak.

Size and shape control of metal nanoparticles has emerged as an urgent requirement to increase "functionality and selectivity"[33] of the material. This urgency is due to the unique chemical and physical properties that different morphologies of nanoparticles possess, which might in turn serve many potential applications of nanoparticles in different fields.

However, full understanding of the exact mechanism explaining shape control reactions of metal nanoparticles is still challenging.[5]

1.4 Functionalization of metal nanoparticles

Metal nanoparticles of gold and silver offer a useable surface for the conjugation of biomolecules through either physical adsorption or chemical coupling through Au-S bond.[34] Both Au and Ag nanoparticles show a high affinity toward thiol and amine functionality,[17] which allows the possibility for a large number of chemical and biological molecules ranging from simple organic molecules (e.g. alkane thiols) to antibodies, DNA and proteins to be conjugated with metal nanoparticles[17] This potential gives them high value in either stabilization of unstable molecules or in the ability to immobilize proteins and enzymes for further study of single molecule per nanoparticle.

As previously described, among the factors that affect plasmon resonance is the local dielectric environment. Small changes in local refractive index can be converted by the plasmonic nanoparticles into spectral shifts in the extinction and scattering spectra.[34] Conversely, some reports revealed, either theoretically or experimentally, the pronounced effect of size, shape and structure of metal nanoparticles on the relationship between plasmon resonance and the dielectric environment (i,e the local refractive index). The dependence of LSPR spectral shift on the sensitivity factor can be explained by the following mathematical expression[35,36]:

$$\Delta\lambda = m\,(n_{adsorbate} - n_{medium})\,(1 - e^{-2d / ld})$$

Where: $\Delta\lambda$**:** LSPR spectral shift

m: sensitivity factor in (nm per **r**efractive **i**ndex **u**nit (RIU))

$n_{adsorbate}$**:** refractive index of the adsorbate in (RIU)

n_{medium}**:** refractive index of the medium in (RIU)

d: the effective thickness of the adsorbate layer in (nm)

l_d: electric field decay length in (nm).

Where **m** can be optimized by careful selection of the nanoparticles size, shape and composition, Δ**n** results as a consequence of molecular adsorption and can be achieved by using larger molecules and resonant labels.

As plasmon resonance depends on the dielectric environment which includes molecules attached to the nanoparticle's surface, the binding of molecules to the nanoparticle's surface causes an increase in the local refractive index. This increase occurs because biomolecules have higher refractive index than buffer solution. Increasing in the local refractive index would cause red-shift of the plasmon resonance wavelength.

This effect of plasmon resonance peak shift upon molecular binding to the metal surface has been successfully utilized as an optical input signal in biosensor applications. Such applications are used to detect molecular binding events and changes in molecular conformation, although the usage of high resolution localized surface plasmon resonance to gather information about the dynamics of protein conformational changes still presents a challenge.

2. Experimental section

2.1 Spherical citrate-capped gold nanoparticles

2.1.1 Synthesis of < 5 nm size citrate-capped gold nanoparticles[37]

50 ml of aqueous solution containing 2.5×10^{-4} M $HAuCl_4$ and 2.5×10^{-4} M trisodium citrate was prepared at room temperature. 1.5 ml of freshly prepared 0.1 M $NaBH_4$ was added to the above stirred solution. The color of the solution changed to pink upon addition of $NaBH_4$, indicating the formation of gold nanoparticles.

2.1.2 Synthesis of 13 nm size citrate-capped gold nanoparticles[38]

150 ml of 2.2 mM sodium citrate aqueous solution was heated under reflux for 15 min then 1.0 ml of 25 mM $HAuCl_4$ solution was injected The color of the solution changed from yellow to bluish grey, and then to soft pink in 10 min.

2.1.3 Synthesis of 20 nm size citrate-capped gold nanoparticles[39]

130 ml of 0.1 M $HAuCl_4$ aqueous solution was brought to reflux then another solution of 0.2 M trisodium citrate was added to the first solution. The reflux was continued for another 15 minutes. The solution color changed to ruby red.

2.2. Synthesis of gold nanorods[40]

Seed solution: 5.0 ml of 0.5 mM $HAuCl_4$ solution was mixed with 5.0 ml of 0.2 M CTAB solution then 0.6 ml of freshly prepared 0.01 M $NaBH_4$ solution was diluted to 1.0 ml with water and was then injected into the above mixture under vigorous stirring. The color of the solution changed from yellow to brownish-yellow. The stirring was continued for 2-5 min. The seed solution was used 1 hr after preparation.

Growth solution: 9.0 g of CTAB together with 1.1 g of 5-bromosalicylic acid was dissolved in 250 ml of warm water at 60 $^{\circ}$C then the solution was allowed to cool down to 30 $^{\circ}$C at which time 12 ml of 4 mM $AgNO_3$ solution was added. The mixture was kept undisturbed at 30 $^{\circ}$C for 20 minutes then 250 ml of 1.0 mM $HAuCl_4$ solution was added.

2.0 ml of 0.064 M ascorbic acid was added after 15 min. of slow stirring, and then the solution was vigorously stirred for one additional minute until it became colorless. Finally, 0.8 ml of seed solution was injected into the growth solution. The resultant

mixture was then stirred for one more minute and left undisturbed in a water bath at 30 °C for 12 hr. for nanorod growth. The nanorods solution was centrifuged at 8500 rpm for 25 min. The precipitate was isolated and redispersed in 10 ml of water.

2.3 Synthesis of decahedral gold nanoparticles[31]

0.25 g of polyvinylpyrrolidone (PVP) was dissolved in 24.5 ml DMF, the solution was heated in an oil bath to 140 °C and kept at the set temperature for 4-5 minutes then 0.5 ml of 10 mM $HAuCl_4$ aqueous solution was added dropwise over a period of 1-2 minutes. The reaction was continued for another 40 minutes keeping the temperature at 140 °C. The sample was centrifuged at 4000 rpm for 15 minutes then the precipitate was washed with water and ethanol. Finally, the product was redispersed in ethanol.

2.4 Synthesis of tetrahedral gold nanoparticles[41]

5.0 ml of ethylene glycol (EG) was heated to reflux in a silicon oil bath under nitrogen atmosphere. Two 5.0 ml solutions of 0.375 M PVP and 0.0664 M $HAuCl_4.3H_2O$ in EG were prepared. PVP solution was injected to boiling EG by means of micropipette, then $HAuCl_4$ solution was injected twice. This process was repeated 15 more times every 30 seconds. Solution color turned from red rust to brownish throughout the course of the reaction. The temperature was kept stable for another 45 minutes before centrifuging the solution three times at 1000 rpm for 5 minutes. Finally, the precipitate was removed and the supernatant was centrifuged at 3500 rpm for 30 minutes. The precipitate was then collected and redispersed in 4.0 ml EG.

2.5 Synthesis of hollow urchin like gold nanoparticles[42]

Synthesis of silver seeds: 25 ml aqueous solution of 1.1 mM $AgNO_3$ was preheated at 70 °C for 10 minutes. 1.5 ml of sodium citrate (1% in mass) was added as soon as the temp. increased to 110 °C. The reaction was then continued for another 90 min. at the set temp., then the colloidal Ag solution was cooled to room temp. The color of the solution changed to yellowish-brownish.

Synthesis of hollow urchin-like gold nanoparticles: 4.0 ml of the previously prepared Ag colloids solution was centrifuged at 4.000 rpm for 5 min then 1.0 ml of 2.94 mM $HAuCl_4$ aqueous solution was added to the resulting Ag precipitate. 1.0 ml of 10 mM ascorbic acid was added immediately. The solution turned dark blue instantly after

$HAuCl_4$ addition. 5 min. later, 400 µL of PVP (50 mM in monomer conc.) was mixed with the product solution to stabilize the resulting nanoparticles from possible aggregation.

2.6 Synthesis of gold nanocubes[41]

5.0 ml of EG was heated to reflux in a silicon oil bath under nitrogen atmosphere. Two 5.0 ml solutions of 0.375 M PVP and 0.083 M $HAuCl_4$ were prepared in EG. 0.5 ml of 0.0059 M $AgNO_3$ solution in EG was added to the boiling EG 10 min. before the addition of PVP and $HAuCl_4$. The injection process for both solutions and the purification procedure was the same as described for the preparation of tetrahedral nanoparticles. The reaction was continued after the final injection for another 45 min. The solution color converted after dilution from rust red-brownish to iridescent blue.

2.7 Synthesis of gold nanoplates[43]

5.0 ml of EG was preheated to a temp. of 155 $^{\circ}$C for 15-20 min. then 1.0 ml of 0.02 M $HAuCl_4$ in EG was prepared, after that another solution of PVP with a weight ratio of 2.0, with respect to $HAuCl_4$, was prepared in 1.0 ml of EG. The $HAuCl_4$ and PVP solutions were added simultaneously into the preheated EG. The reaction was held at a set temp. for 25 min. The color of the solution turned to reddish brown after several minutes. The solution was centrifuged at 4000 rpm for 15 min. then washed with ethanol. This process was repeated three times. Finally, the precipitate was redispersed in ethanol.

2.8 Synthesis of trihedral gold nanoplates[43]

5.0 ml of EG was preheated to a temp. of 155 $^{\circ}$C. 1.0 ml of 0.1 M $HAuCl_4$ solution was prepared in EG, then another solution of PVP with a weight ratio of 1.5, with respect to $HAuCl_4$ was prepared in 1.0 ml of EG. Both solutions were added simultaneously into the preheated EG. The reaction was kept at set temp. for 20 min. The color of the solution changed to reddish brown after several minutes. The product was washed three times and redispersed for further characterization using ethanol.

2.9 Synthesis of AgAu core-shell nanoparticles[44]

Synthesis of Ag NPs seeds: 20 ml of 50 mM $AgNO_3$ solution was prepared in oleylamine then slowly heated to 180 $^{\circ}$C under the flow of a nitrogen stream. The reaction was continued for 1 hr. for the growth of the nanoparticles. 30 ml of ethanol was added to the solution as soon as it cooled to room temp. The nanoparticles were then separated by centrifugation (8000 rpm, 10 min). The precipitate was redispersed in 15 ml of hexane after three washes of ethanol.

Synthesis of AgAu core-shell NPs: 20 ml of 6.3 mM $HAuCl_4$ solution was prepared in octadecene with the addition of 2.0 ml of oleylamine. The solution was heated to 50 $^{\circ}$C under nitrogen atmosphere, then 2.0 ml of hexane solution containing 10 mg of AgNPs was injected at this temp. The solution was kept at 50 $^{\circ}$C for an additional 2 hrs. The reaction was then allowed to cool down to room temp. before 30 ml of ethanol was added. Finally, the solution was centrifuged at 8000 rpm for 10 min., washed with ethanol a couple of times, and then redispersed in 15 ml of hexane.

3. Results and discussion

3.1 Spherical citrate-capped gold nanoparticles having different sizes

Citrate-stabilized Au NPs method has been applied in order to synthesize spherical gold nanoparticles by employing citrate molecules as both reducing and stabilizing agents. Such employment triggers the formation of the nanoparticles by reducing gold from its precursor and then by physical adsorption to the surface of the resulting nanoparticles. This process provides colloidal stability due to the presence of negatively charged citrate ions[33]. Variation in the ratio between stabilizer molecules and metal salt precursor allows the possibility of having different sizes of nanoparticles (Figure 8 b,c). On the other hand, obtaining nanoparticles with less than 5 nm size can be achieved by using sodium boronium hydride as a stronger reducing agent and using citrate only as a stabilizing agent (Figure 8a). The weakly adsorbed citrate molecules on the surface of the NPs are advantageous here since they allow for functionalization of the nanoparticles by employing ligands with a higher binding affinity to the NPs, thus replacing the already existing citrate molecules.

The resulting nanoparticle solutions were characterized by transmission electron microscopy (TEM) as illustrated in (Figure 8) and UV-Vis spectroscopy (Figure 9).

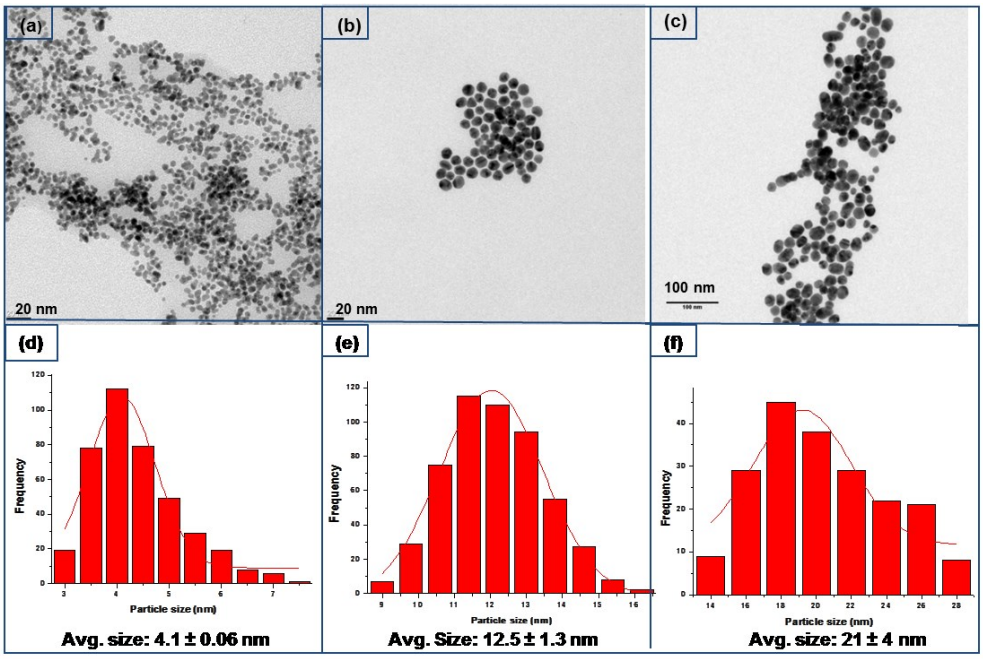

Figure 8: TEM images (a-c) of differently sized spherical citrate-capped Au NPs and their corresponding size distribution histograms (d-f)

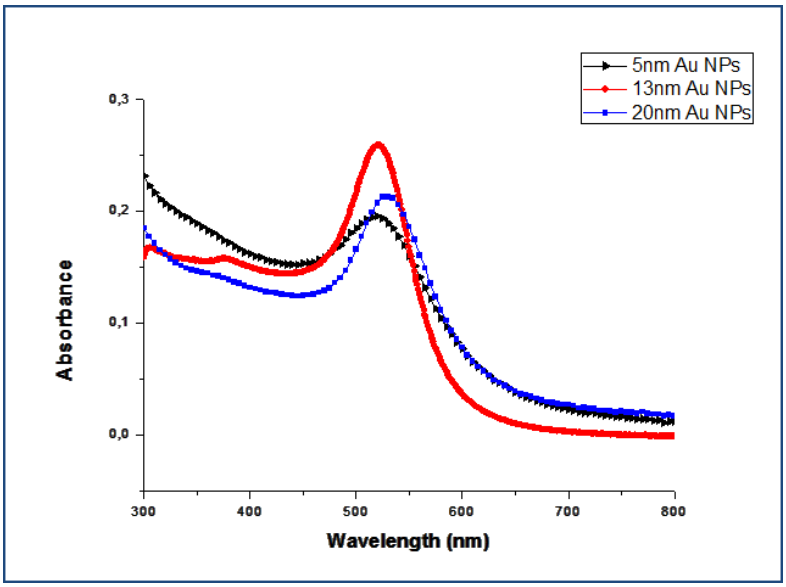

Figure 9: UV-Vis absorption spectrum for differently sized spherical gold nanoparticles

Spherical gold nanoparticles show a plasmon peak of around 520 nm. Absorption results as a consequence of the polarizability of the nanoparticles influenced by the electric field of the stimuli[45] (illustrated in Figure 10). It is especially important to mention that controlling the position of surface plasmon peak according to the size of spherical nanoparticles is limited since nanoparticles smaller than 50 nm show a slight shift in their plasmon peak position.[46] (See Figure 9.) In order to maintain better control over LSPR peak for spherical nanoparticles, the dielectric constant of the nanoparticles' medium can be changed through nanoparticle biofunctionalization (as mentioned above).

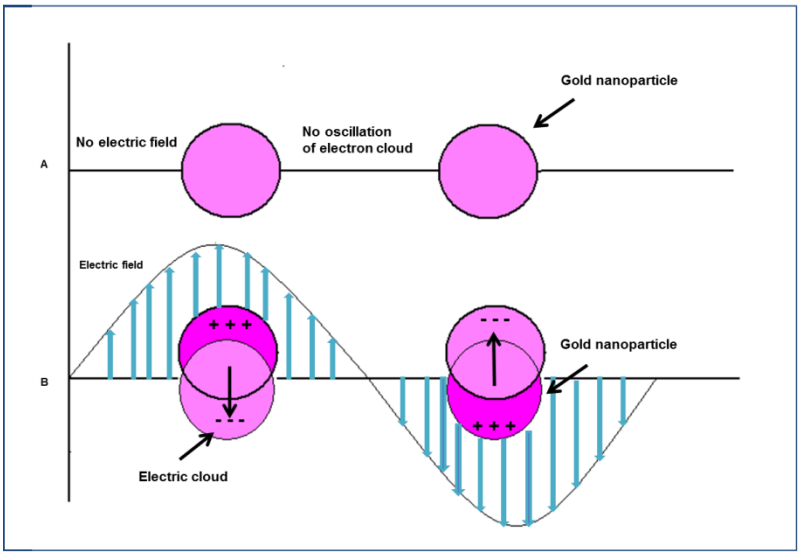

Figure 10: Effect of electric field of external stimuli on the conductive electrons of gold nanoparticles[45]

3.2 Gold nanostructures with other shapes

3.2.1 One-dimensional gold nanostructures: gold nanorods

Nanorods were prepared using the seed-mediated growth approach in a two-step synthesis; in the first step small-sized gold nanoparticles were generated by reduction of gold salt using sodium borohydride for seed formation functioning as nucleation sites[47] for further growth. The second step involved addition of the growth solution containing more gold ions, CTAB and ascorbic acid as well as the organic additive 5-bromosalysilic acid. Silver ions were also added as a promoter due to their preferential binding to specific planes of the crystallographic form of gold seeds, therefore promoting the growth along other planes[48,49]. CTAB is used as a micellar rode-like template or surfactant to direct the growth process of the nanorods into one dimension and then stabilize the resulting nanorods through formation of bilayer surfactant along the faces of the nanorods.[50,51] Ascorbic acid is used as a mild reducing agent to help in the reduction of gold ions to neutral gold with the aid of seed particles[49]. In general, among other factors for controlling the aspect ratio of nanorods could be by monitoring the amount of Au seeds that are added to the growth solution[52]. Figure 11 shows TEM image (a) and SEM image (b) alongside their corresponding dimensions distribution histograms (c & d).

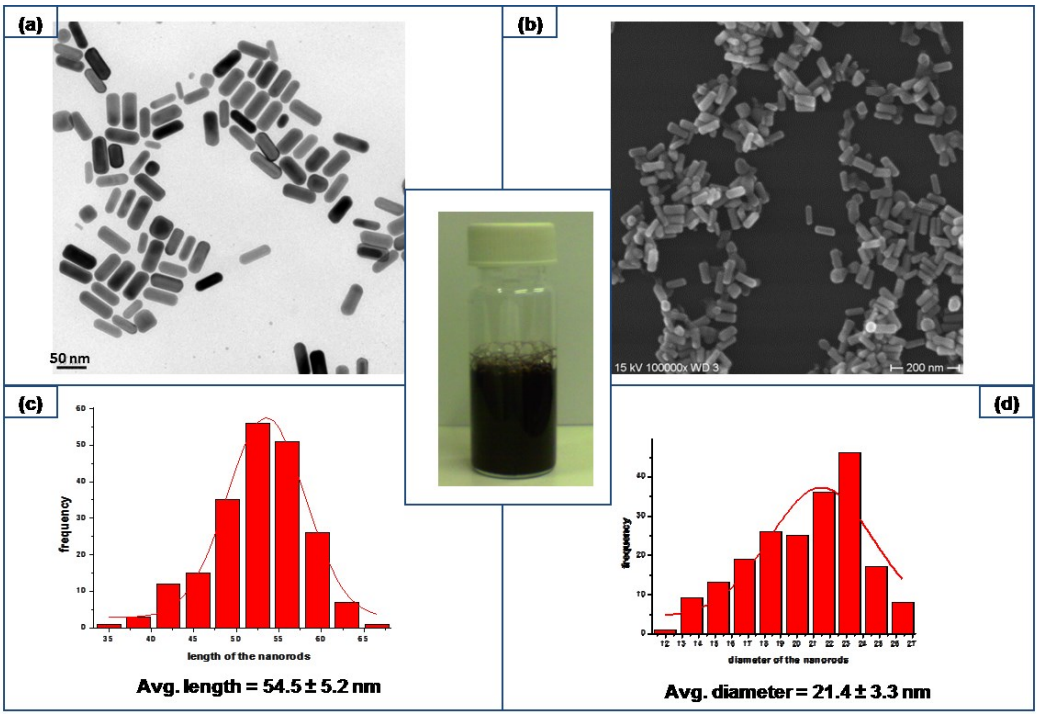

Figure 11: TEM (a) and SEM (b) images of gold nanorods with their length (c) and diameter (d) distribution histograms

In nanorod particles, LSPR splits into two modes, i.e. longitudinal and transverse (as indicated by Figure 12). The transverse plasmon maximum appears around 529 nm, which resembles the conventional position for spherical gold nanoparticles, while the longitudinal plasmon peak appears around 698 nm and could be red-shifted to near IR region by increasing the aspect ratio of the nanorods (the ratio of the length to the diameter of the particle)[46,48]

In general, both physical properties of gold nanorods represented by their LSPR peak position in the extinction spectrum, as well as their chemical reactivity towards functionalization, are highly influenced by variations of their aspect ratio.

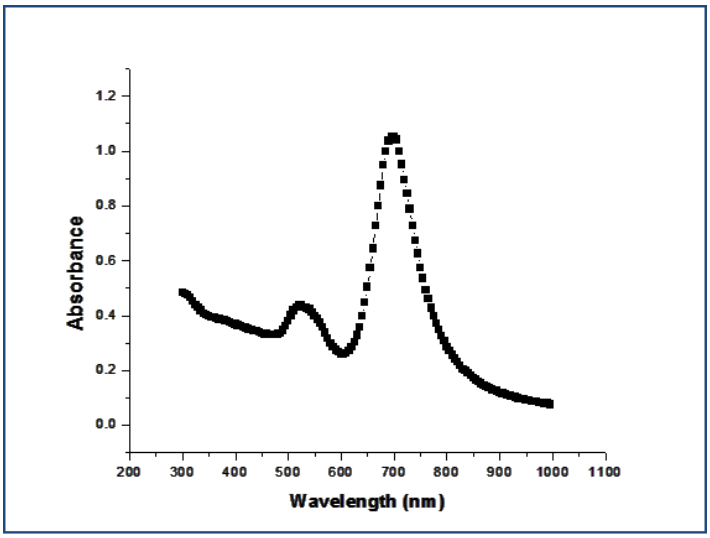

Figure 12: UV-Vis spectrum for gold nanorods

3.2.2 Two-dimensional gold nanostructures: trihedral and nanoplates gold nanoparticles

This class of gold nanoparticle possesses attractive applications in surface-enhanced Raman spectroscopy and optical biosensing due to its interesting physical properties that result as a consequence of high localization of electric field near the corners and edges of the nanostructures, influenced by illumination of external stimuli[53,54]. The synthetic approach employed through “polyol process”, in which gold ions are thermally reduced in the presence of highly boiling point solvent (ethylene glycol (EG)) and polyvinylpyrrolidone (PVP) as a stabilizer.

Variations in the gold salt concentration as well as the weight ratio of PVP stabilizer result in the generation of trihedral nanoparticles with an average size of 178 nm. In contrast, a mixture of trihedral and hexagonal nanoplates produced in the micrometer

range with an average size of 4.1 µm (shown in Figure 13 and Figure 14, respectively).

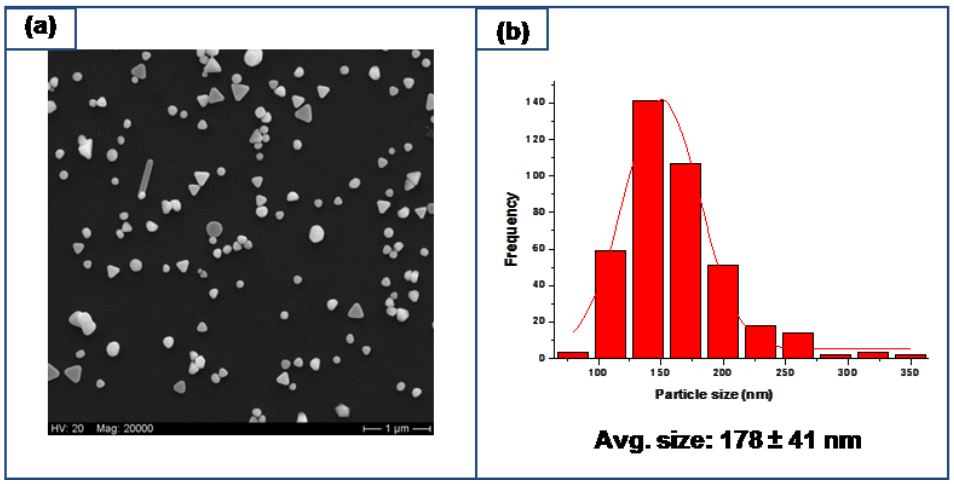

Figure 13: SEM image of trihedral gold nanoparticles (a) and their size distribution histogram (b)

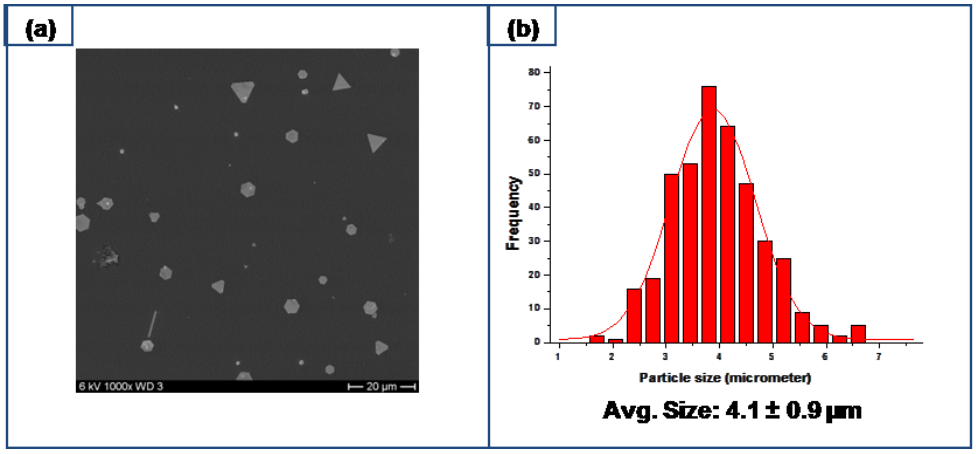

Figure 14: SEM image of gold nanoplates (a) and their size distribution histogram (b)

UV-visible measurements for both products reveal LSPR peak absorption maximum for trihedral nanoparticles as around 600 nm, while nanoplates show two absorption maxima around 606 nm and 797 nm as illustrated in Figure 15.

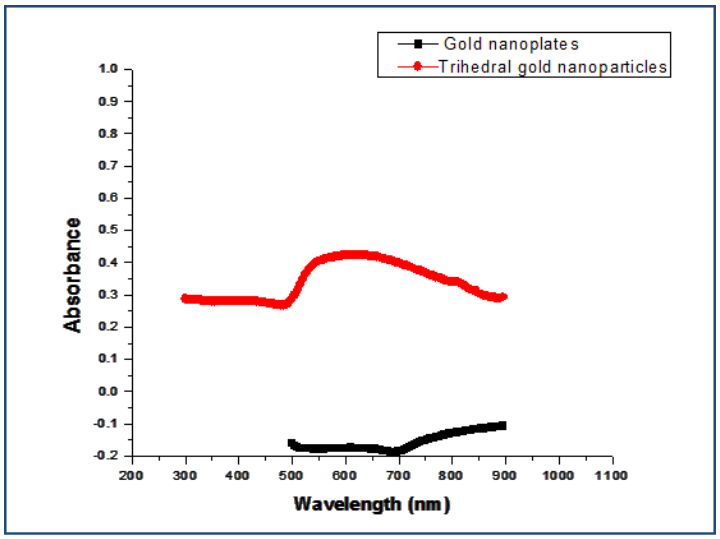

Figure 15: UV-Vis spectrum for trihedral and gold nanoplates

3.2.3 Three-dimensional gold nanostructures: tetrahedral, decahedral and gold nanocubes

For the formation of tetrahedral nanostructures, as well as gold nanocubes, the "polyol process" was applied as well. Under high ratio of PVP : gold salt precursor tetrahedral nanoparticles were produced with an average size of 206 nm, while introducing silver ions to the reaction prior the addition of gold ions and PVP resulted in the formation of gold nanocubes with an average size of 192 nm a (shown in Figure 16 and Figure 17, respectively).

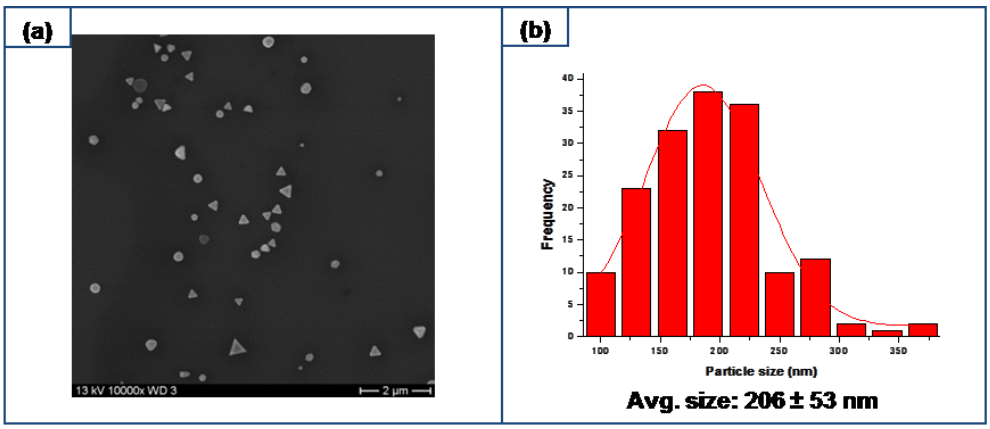

Figure 16: SEM image of tetrahedral gold nanoparticles (a) and their size distribution histogram (b)

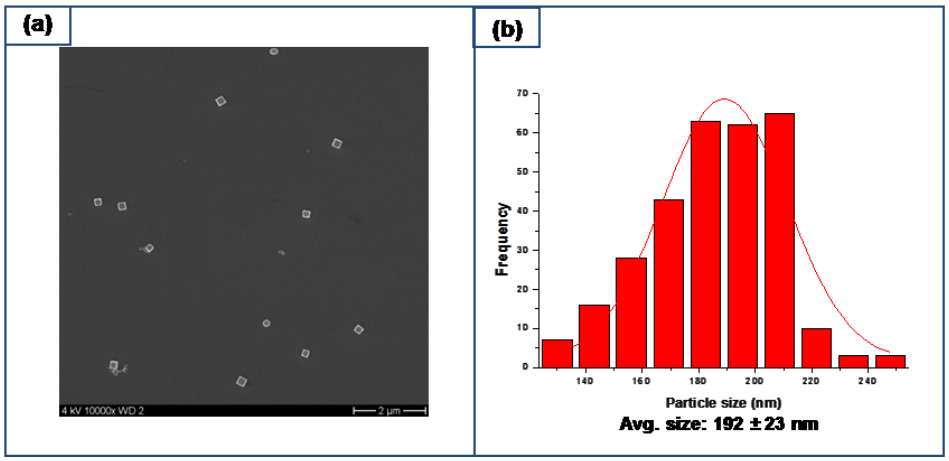

Figure 17: SEM image for gold nanocubes (a) and their size distribution histogram (b)

On the other hand, decahedral gold nanoparticles with an average size of 142 nm were generated by applying the "polyol process" in DMF instead of polyethylene glycol solvent with variation the molar ratio between gold salt : PVP as indicated by Figure 18.

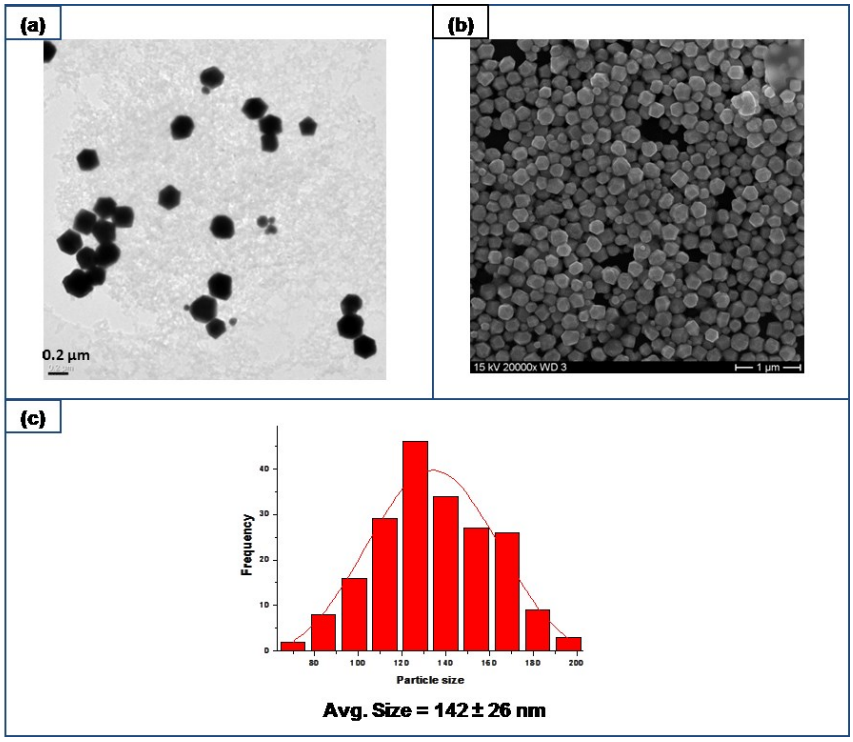

Figure 18: TEM (a) and SEM (b) images for decahedral gold nanoparticles with their size distribution histogram (c)

Analyzing the generated solutions using UV-Vis spectroscopy revealed absorption maxima for tetrahedral nanostructures to be around 600 nm, while gold nanocubes' absorption peak appeared to be around 602 nm and for decahedral nanoparticles, around 588 nm, as illustrated in Figure 19.

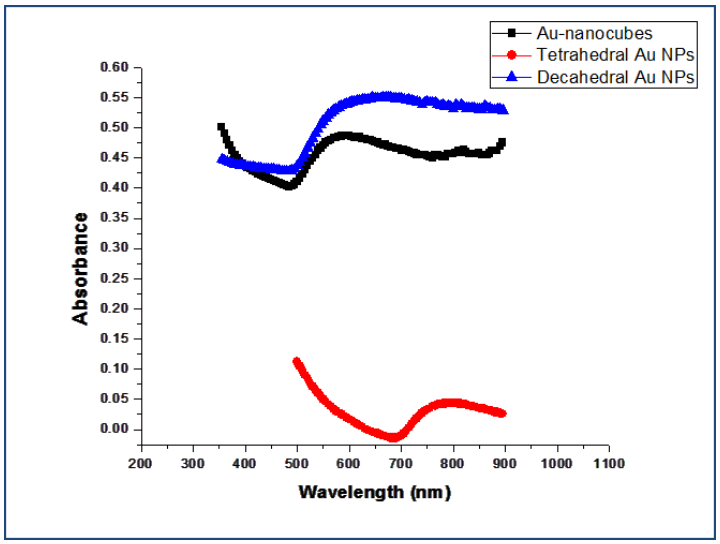

Figure 19: UV-Vis spectrum for decahedral, tetrahedral and gold nanocubes

3.2.4 Hollow urchin-like gold nanoparticles

The synthetic protocol for hollow urchin-like gold nanostructures – see Figure 20 – involves formation of silver seeds stabilized by citrate ions. In a subsequent step, gold ions were added and reduced by silver seeds through a galvanic replacement process and then deposited on the seeds to form hollow urchin-like structures. The resulting nanostructures have an average size of 75 nm.

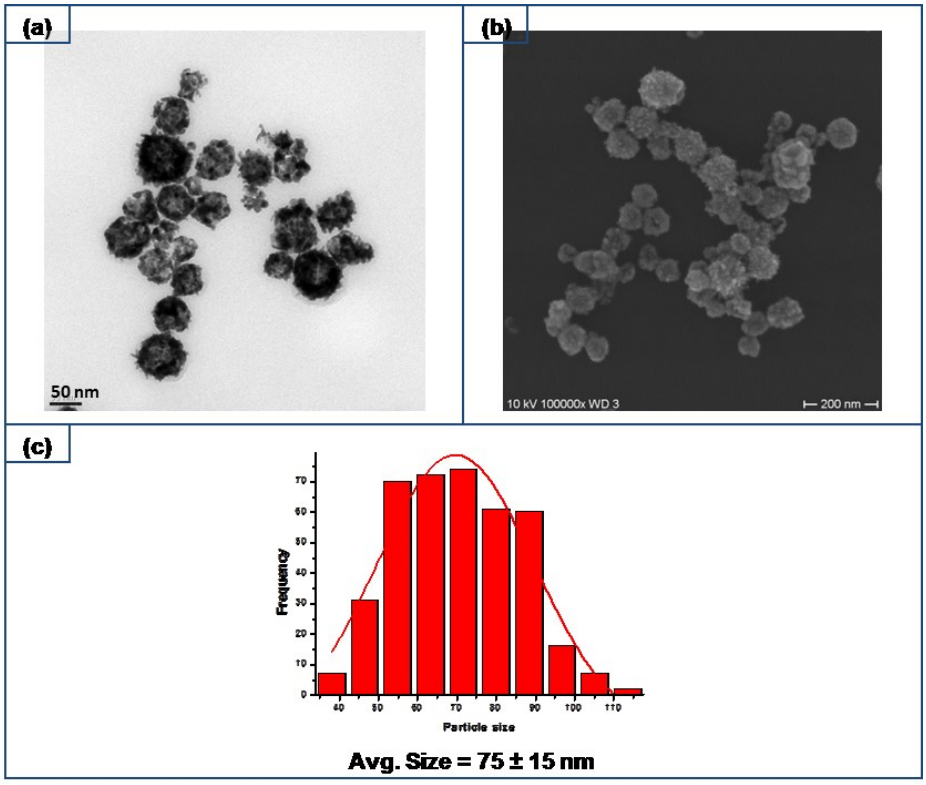

Figure 20: TEM (a) and SEM (b) images for hollow urchin-like gold nanoparticles and their size distribution histogram (c)

The UV-Vis spectrum resulting from the formation of hollow urchin-like nanostructures is shown in Figure 21. The plasmon resonance absorption peak for the product appears in the range of 750 nm. Changing the molar ratio between silver seeds and Au ions could be used in order to control the optical properties of the resulting nanostructures[55]

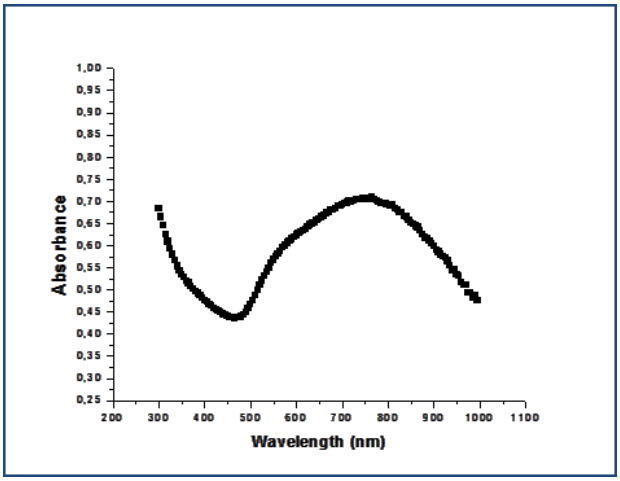

Figure 21: UV-Vis spectrum for hollow-urchin like gold nanoparticles

3.3 Metal nanoparticles with other Compositions

3.3.1 Silver nanoparticles

Silver ions were thermally reduced at 180 °C then stabilized by oleylamine molecules, which are adsorbed on the surface of the nanoparticle to provide colloidal stability. The resulting nanoparticles have an average size of 12.6 nm, as indicated by Figure 22.

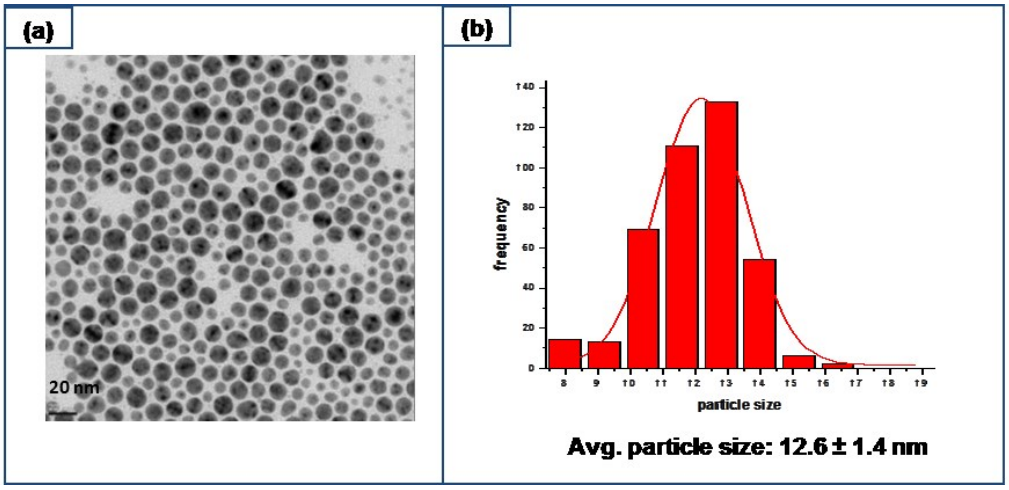

Figure 22: TEM image for silver nanoparticles (a) and their size distribution histogram (b)

3.3.2 AgAu core-shell nanoparticles

AgAu core-shell nanoparticles were synthesized using previously prepared silver nanoparticles as seeds and by depositing gold ions on the surface of silver seeds in order to form a shell around the silver nanoparticles, thus forming the core.

The reaction was carried out at 50 °C, a temperature sufficient for minimal diffusion of gold ions onto the surface of Ag NPs, therefore providing a core-shell system rather than alloy nanoparticles, which can result under higher reaction temperatures[44].

Size calculation depending on the TEM images reveal that, surprisingly, the resulting nanoparticles have almost the same diameter as the silver seeds. This discovery does not acquiesce with the previous reports that the nanoparticles would have a gold shell around 4 nm thick[44]. Representative TEM image for the nanoparticles with the corresponding size distribution histogram are shown in Figure 23

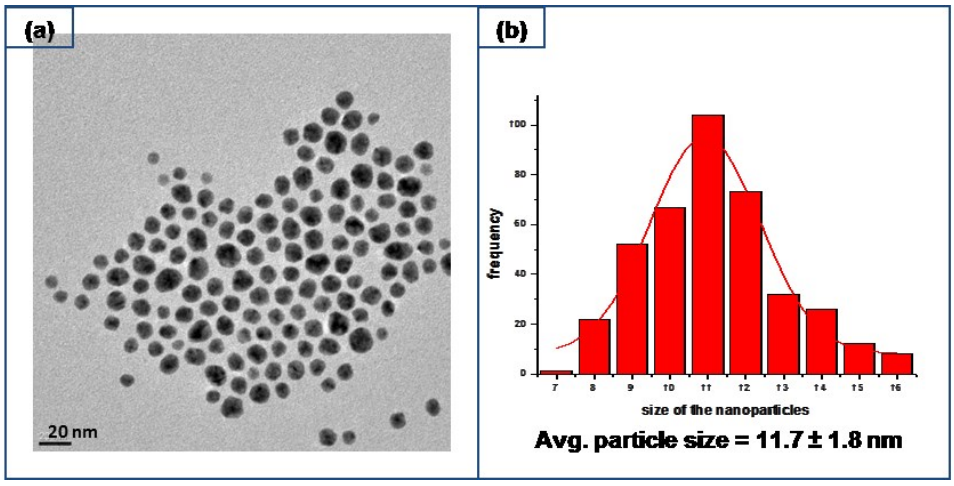

Figure 23: TEM image for AgAu core-shell nanoparticles (a) and their size distribution histogram (b)

The sample was characterized by EDX, indicated in Figure 24, to examine the elemental composition of the sample. EDX measurements show that there are two peaks corresponding to both gold and silver, indicating that the two elements are present in the sample. What still needs clarification is whether silver and gold appear as a core-shell system, or as isolated nanoparticles independent of each other. To investigate this point UV-Vis measurement was conducted, then the resultant spectrum was compared to the spectrum resulting from silver seeds and to a third

spectrum resulting from spherical gold nanoparticles with almost the same size shown in Figure 25.

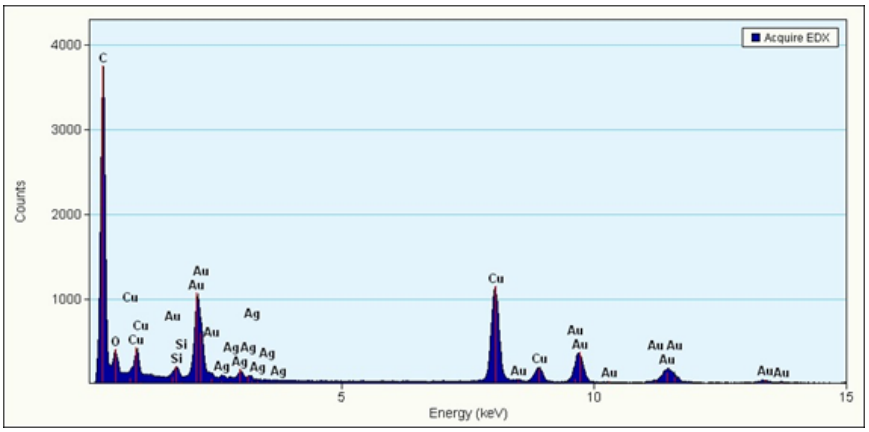

Figure 24: EDX measurements for AgAu core-shell nanoparticles

As it is clarified in Figure 25, silver nanoparticle seeds have a plasmon resonance peak around 400 nm, while core-shell nanoparticles show a spectral shift around 524 nm, which resembles the position of spherical gold nanoparticles with the same diameter. It is also worth mentioning that the resulting spectrum shows one single absorption peak for their nanoparticles, which would not be the case if gold and silver were formed independently of one another. However, the unexpected results from the analysis of TEM images could also be attributed to uncertain results from either the TEM instrument itself or as a consequence of data processing. In particular, the expected shell thickness of just 4 nm, a relatively small figure which can easily drop due to uncertain measurements.

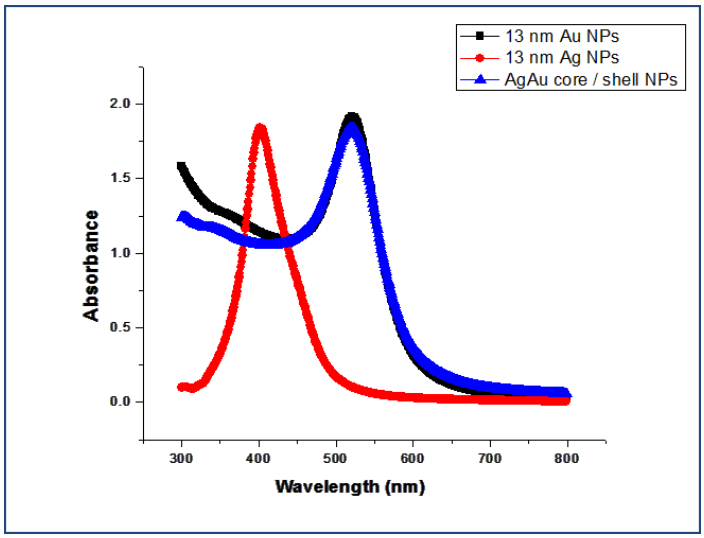

Figure 25: UV-Vis spectrum for spherical Au NPs, spherical Ag NPs and AgAu core-shell NPs having a comparable size

In summary, versatile numbers of metal nanostructures were successfully prepared, in agreement with what has been previously reported in the literature, therefore providing a useful and versatile toolbox for the subsequent chapters.

4. Conclusion

We have applied different synthetic methods based mainly on “wet chemical synthesis” to prepare a number of differently sized and shaped metal nanoparticles.

The resulting nanoparticles were characterized using TEM, SEM and UV-Vis spectroscopy, showing the successful synthesis of different nanostructures.

The resulting nanostructures will be used in the patterning strategies **(chapter 3)** and in the transference process to the surface of polyethylene glycol hydrogel polymer **(chapter 4)**.

5. Bibliography

(1) http://www.nano.org.uk/what-is-nanotechnology#what-is-nanotechnology.

(2) Horikoshi, S.; Serpone, N. In *Microwaves in Nanoparticle Synthesis*; Horikoshi, S.; Serpone, N., Eds.; WILEY-VCH Verlag GmbH & Co. KGaA, **2013**; pp. 1–24.

(3) Vert, M.; Doi, Y.; Hellwich, K.; Hess, M.; Hodge, P.; Kubisa, P.; Rinaudo, M.; Schué, F. *Pure Appl. Chem.* **2012**, *84*, 377–410.

(4) Blosi, M.; Albonetti, S.; Gatti, F.; Baldi, G.; Dondi, M. *Dye. Pigment.* **2012**, *94*, 355–362.

(5) Zijlstra, P.; Orrit, M. *Reports Prog. Phys.* **2011**, *74*, 1–55.

(6) Dykman, L. A.; Khlebtsov, N. G. *Acta Naturae* **2011**, *3*, 34–55.

(7) Feynman, R. P. *Eng. Sci.* **1960**, *23*, 22–36.

(8) Bhattacharya, R.; Mukherjee, P. *Adv. Drug Deliv. Rev.* **2008**, *60*, 1289–1306.

(9) Kim, Y.; Cho, G.; Song, J. H. *Nucl. Instruments Methods Phys. Res. B* **2007**, *254*, 73–77.

(10) Toderas, F.; Baia, M.; Maniu, D.; Astilean, S. *J. Optoelectron. Adv. Mater.* **2008**, *10*, 2282 – 2284.

(11) Tsai, D.; Chen, C.; Chou, C. *Mater. Chem. Phys.* **2005**, *90*, 361–366.

(12) Nikolov, A. S.; Nedyalkov, N. N.; Nikov, R. G.; Atanasov, P. A.; Alexandrov, M. . T. *Appl. Surf. Sci.* **2011**, *257*, 5278–5282.

(13) Tinguely, J.; Charron, G.; Lau-Truong, S.; Hohenau, A.; Grand, J.; Félidj, N.; Aubard, J.; Krenn, J. R. *J. Colloid Interface Sci.* **2013**, *394*, 237–242.

(14) Lee, K.; El-sayed, M. A. *J. Phys. Chem. B* **2006**, *110*, 19220–19225.

(15) Noguez, C. *J. Phys. Chem. C* **2007**, *111*, 3806–3819.

(16) Sekhon, J. S.; Verma, S. S. *Plasmonics* **2011**, *6*, 311–317.

(17) Bhattacharyya, S.; Kudgus, R. A.; Bhattacharya, R.; Mukherjee, P. *Pharm. Res.* **2011**, 237–259.

(18) Lu, F.; Tian, Y.; Liu, M.; Su, D.; Zhang, H.; Govorov, A. O.; Gang, O. *Nano Lett.* **2013**, *13*, 3145–3151.

(19) Ranjan, M.; Facsko, S. *Nanotechnology* **2012**, *23*, 1–7.

(20) Vigderman, L.; Zubarev, E. R. *Langmuir* **2012**, *28*, 9034–9040.

(21) Cuenya, B. R. *Thin Solid Films* **2010**, *518*, 3127–3150.

(22) Mahmoud, M. A.; Narayanan, R.; El-Sayed, M. A. *Acc. Chem. Res.* **2013**, *46*, 1795–1805.

(23) Zhang, J. Z. *J. Phys. Chem. Lett.* **2010**, *1*, 686–695.

(24) Intartaglia, R.; Das, G.; Bagga, K.; Gopalakrishnan, A.; Genovese, A.; Povia, M.; Fabrizio, E. D.; Cingolani, R.; Diaspro, A.; Brandi, F. *Phys. Chem. Chem. Phys.* **2013**, *15*, 3075–3082.

(25) Fan, C.; Poumellec, B.; Zeng, H.; Desmarchelier, R.; Bourguignon, B.; Chen, G.; Lancry, M. *J. Phys. Chem. C* **2012**, *116*, 2647–2655.

(26) Hee, J.; Park, J. R. *J. Korean Phys. Soc.* **2009**, *54*, 2143–2147.

(27) Okitsu, K.; Sharyo, K.; Nishimura, R. *Langmuir* **2009**, *25*, 7786–7790.

(28) Philip, D. *Phys. E* **2010**, *42*, 1417–1424.

(29) Castro, L.; Blázquez, M. L.; González, F.; Munoz, J. A.; Ballester, A. *Chem. Eng. J.* **2010**, *164*, 92–97.

(30) Narayanan, K. B.; Sakthivel, N. *Adv. Colloid Interface Sci.* **2010**, *156*, 1–13.

(31) Chen, Y.; Gu, X.; Nie, C.-G.; Jiang, Z.-Y.; Xie, Z.-X.; Lin, C.-J. *Chem. Commun.* **2005**, 4181–4183.

(32) Ahmed, W.; Kooij, E. S.; Van Silfhout, A.; Poelsema, B. *Nanotechnology* **2010**, *21*, 1–6.

(33) Tao, A. R.; Habas, S.; Yang, P. *Small* **2008**, *4*, 310–325.

(34) Khlebtsov, N. G.; Dykman, L. A. *J. Quant. Spectrosc. Radiat. Transf.* **2010**, *111*, 1–35.

(35) Anker, J. N.; Hall, W. P.; Lyanders, O.; Shah, N. C.; Zhao, J.; Van Duyne, R. P. *Nat. Mater.* **2008**, *7*, 442–453.

(36) Chen, H.; Kou, X.; Yang, Z.; Ni, W.; Wang, J. *Langmuir* **2008**, *24*, 5233–5237.

(37) Jana, N. R.; Gearheart, L.; Murphy, C. J. *Langmuir* **2001**, *17*, 6782–6786.

(38) Bastús, N. G.; Comenge, J.; Puntes, V. *Langmuir* **2011**, *27*, 11098–11105.

(39) Turkevich, J.; Stevenson, P. C.; Hillier, J. *Discuss. Faraday Soc.* **1951**, *11*, 55–75.

(40) Ye, X.; Jin, L.; Caglayan, H.; Chen, J.; Xing, G.; Zheng, C.; Doan-Nguyen, V.; Kang, Y.; Engheta, N.; Kagan, C. R.; Murray, C. B. *ACS Nano* **2012**, *6*, 2804–2817.

(41) Kim, F.; Connor, S.; Song, H.; Kuykendall, T.; Yang, P. *Angew. Chem. Int. Ed. Engl.* **2004**, *43*, 3673–3677.

(42) Wang, W.; Pang, Y.; Yan, J.; Wang, G.; Suo, H.; Zhao, C.; Xing, S. *Gold Bull.* **2012**, *45*, 91–98.

(43) Lee, J.-H.; Kamada, K.; Enomoto, N.; Hojo, J. *Cryst. Growth Des.* **2008**, *8*, 2638–2645.

(44) Wang, C.; Peng, S.; Chan, R.; Sun, S. *Small* **2009**, *5*, 567–570.

(45) Satija, J.; Bharadwaj, R.; Sai, V.; Mukherji, S. *Nanotechnol. Sci. Appl.* **2010**, *3*, 171–188.

(46) Harris, N.; Ford, M. J.; Mulvaney, P.; Cortie, M. B. *Gold Bull.* **2008**, *41*, 5–14.

(47) Gole, A.; Murphy, C. J. *Chem. Mater.* **2004**, *16*, 3633–3640.

(48) Placido, T.; Comparelli, R.; Giannici, F.; Cozzoli, P. D.; Capitani, G.; Striccoli, M.; Agostiano, A.; Curri, M. L. *Chem. Mater.* **2009**, *21*, 4192–4202.

(49) Grzelczak, M.; Perez-Juste, J.; Mulvaney, P.; Liz-Marzan, L. M. *Chem. Soc. Rev.* **2008**, *37*, 1783–1791.

(50) Zhang, Q.; Yin, Y. *Chem. Commun. (Camb).* **2013**, *49*, 215–217.

(51) Jana, N. R.; Gearheart, L.; Murphy, C. J. *Adv. Mater.* **2001**, *13*, 1389–1393.

(52) Xu, Z.-C.; Shen, C.-M.; Xiao, C.-W.; Yang, T.-Z.; Zhang, H.-R.; Li, J.-Q.; Li, H.-L.; Gao, H.-J. *Nanotechnology* **2007**, *18*, 1–5.

(53) Navarro, J. R. G.; Manchon, D.; Lerouge, F.; Blanchard, N. P.; Marotte, S.; Leverrier, Y.; Marvel, J.; Chaput, F.; Micouin, G.; Gabudean, A.-M.; Mosset, A.; Cottancin, E.; Baldeck, P. L.; Kamada, K.; Parola, S. *Nanotechnology* **2012**, *23*, 1–8.

(54) Jeong, G. H.; Lee, Y. W.; Kim, M.; Han, S. W. *J. Colloid Interface Sci.* **2009**, *329*, 97–102.

(55) Zhao, L.; Ding, K.; Ji, X.; Li, J.; Wang, H.; Yang, W. *Colloids Surfaces A Physicochem. Eng. Asp.* **2011**, *386*, 172–178.

Chapter 3

Patterning of gold nanoparticles onto silicon substrates

The ultimate goal of this chapter is to pattern Au NPs onto silicon substrate with defined size, shape, spacing and position, to be applied as templates in our strategy for biofunctional molecule immobilization. A number of approaches are applied, namely “block copolymer micelle nanolithography,” self-assembled monolayer of different shapes of gold nanostructures onto amino-silanized silicon surfaces and a combinational approach between micro-contact printing strategy and self-assembly.

Finally, the accessibility of patterned gold nanoparticles towards functionalization after silanization and contacting with poly dimethylsiloxane (PDMS) stamp is demonstrated.

Jingyu Chen, **Manar Arafeh**, Diana Felkel, Axel Loebus, Susan Kelleher, Anna Fischer, Marga Lensen, *J. Mater. Chem. C*, **1**, 7709-7715 (2013)

Cigdem Yesildag, **Manar Arafeh** and Marga C. Lensen, Micro-pattern of gold nanoparticles on silicon using micro-contact printing approach. *(in preparation)*

1. Introduction

1.1 Patterning; definition and strategies

Patterning may be defined as the arranging of nano-objects, well-defined in size, shape, and location, into a particular arrangement or predefined patterns.

In general, two patterning strategies have been recognized as main categories: bottom-up and top down.

The top-down approach is represented by conventional fabrication methods such as photolithography,[1] electron beam lithography[2,3], focused ion beam[4] and X-ray.[5] These methods have advantages in providing separations between the nanostructures that are not feasible by self-assembly techniques as well as being unable to produce aperiodic arrangement of nanopattern. However, they hardly achieve a resolution of the nanopattern below 100 nm. Moreover, as these methods depend mainly on light, they have limitations related to light diffraction. Such processes are also time consuming,[6] extremely expensive[7] and requiring highly sophisticated equipment.

In the bottom-up approach, nanofabrication results as a consequence of self-organization of nanoobjects generating nanostructured materials. This method allows a better control over the size, shape and surface chemistry of nanoparticles, in order to achieve diversity in the organization and arrangement of nanostructures. Simple processing and inexpensive equipment are the main advantages of this approach. Limitations arise due to a restricted ability to produce aperiodic arrangement of nanopatterns. Block copolymer lithography[8] and colloidal lithography[9] are famous examples of this approach.[10]

A third approach is a combination between the top down and bottom up approaches, capitalizing on the advantages and overcoming the limitations of each. For instance, Spatz' group reported a certain combination between generated pattern from pure self-assembly of block copolymer micelle (bottom-up) and conventional lithographic methods, such as electron beam writing (top down), achieving new length scales, feature sizes and arrangements that were not possible by pure self-assembly or pure conventional lithography.[6,11]

1.2 Block copolymer micelle nanolithography

Block copolymers are polymers that consist of more than one type of polymeric chain, and the molecules of which are linked linearly in blocks that covalently link to each other.[12,13] Polystyrene – block – poly (2-vinylpyridine) – the polymer which is employed in this work – consists of two blocks; polystyrene and poly (2-vinylpyridine), which are covalently linked to each other.

˝Block copolymer micelle˝ (BCM) nanolithography is considered to be one of the most promising bottom-up approaches to creating well-ordered nanopatterns of metal nanostructures. This consideration is due to its ability to self-assemble on substrates,[14] therefore achieving resolution up to 45 nm. The value of this method is due to its potential for applicability to many different kinds of substrates, as well as its precise control over the size and spacing of particles, which are crucial parameters in terms of biofunctional molecule immobilization. Furthermore, plasma treatment during the fabrication process gives the deposited nanoparticles certain stability on the surface.

1.3 Self-assembled monolayer of nanoparticles on the surface

Arrays fabricated by self-assembled monolayers of covalently linked and varying morphologies of metal nanostructures onto a functionalized substrate are expected to play a vital role in biofunctional molecules immobilization. This role is facilitated through sensitivity enhancement of SPR assay, which is affected by dielectric environment of the surrounding media[15] (for details see chapter 2; introduction). We attempted to self-assemble different morphologies of metal nanostructures onto chemically functionalized silicon substrates to be transferred afterwards to the PEG hydrogel surface as will be described in chapter 4.

1.4 Microcontact printing approach (μCP)

Creating micro-pattern using microcontact printing approach is composed of two main steps: the inking step and the printing step. The inking step involves inking the stamp with the desired material to be transferred to the substrate. In the printing step, the ink would be delivered to the substrate through pressing the stamp onto the surface of the selected substrate.

In order to enhance the efficiency of the stamping process, certain control should be considered related to the relative strength of interaction between the ink molecules and the stamp on one side as well as the strength of the interaction between the ink and the substrate on the other side. To achieve better performance for microcontact printing technique, the ink interaction with the stamp should be weaker than that with the substrate.[16]

Methods based on microcontact printing have the advantages of being relatively easy and allowing patterning on a large scale. Moreover, it allows patterning of close-packed arrays of gold nanoparticles onto the surface of solid support.[17] Limitations of this approach are the possibility of multilayer formation as well as loss of order of the patterned nanoparticles, especially at the edge of the stamp.[18]

1.5 Hybrid hierarchical pattern of gold nanoparticles and polyethylene glycol hydrogel

A member of Lensen Lab has successfully developed a method for creating a novel system based on a hybrid hierarchical pattern of micro-stripes composed of gold nanoparticles obtained by micro-contact deprinting with polyethylene glycol microstructures[19]– a method that has also been developed in our group[20]– See Figure 26.

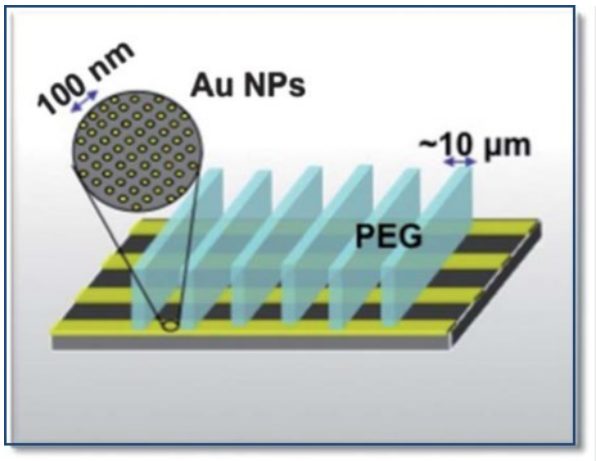

Figure 26: Hybrid hierarchical pattern of Au NPs and PEG hydrogel[19]

1.6 Accessibility of gold nanoparticles toward functionalization

The fabrication method in the previous system involves employing poly dimethylsiloxane (PDMS) mold in order to create PEG microstructures on the substrate. Also involved is the functionalization of Si-Au NPs substrates with an

acrylic group to increase the wettability of PEG prepolymer onto the substrate during the filling process and be crosslinked with PEG bars upon UV-curing. Silicon surface bearing Au NPs was therefore modified with acrylic silane derivative.

The desired result is to use the nanoparticles for further functionalization, the accessibility of gold nanoparticles on the substrate for further functionalization processes after silanization and contacting with PDMS mold was a major issue.

1.7 Biofunctional molecules onto Au NPs arrays

The main challenge that arises concerning biofunctional molecules immobilization is maintaining their spatial orientation on the surface in such a way that their biological activity is retained. Our concept in this regard guarantees a number of parameters, such as size of nanoparticles and hence, the number of immobilized biomolecules per particle down to a single biomolecule per particle. The spacing between the nanoparticles will also be considered and hence, the orientation of biomolecules (crowding effect). In addition to that the coverage of immobilized biofunctional molecules through particles surface density will also be addressed as well as specificity and selectivity in terms of Au-ligands conjugation gives a high potential value in the frame of proteins immobilization. This is done in such a way that both proteins' stability and activity would be reserved.

2. Experimental

2.1 Silicon – Au NPs substrates by "block copolymer micelle" nanolithography

General procedure:

Initially, a set of micellar solutions of polystyrene – block – poly (2-vinylpyridine) was prepared by dissolving PS_{183} – b – $P2VP_{52}$ (Polymer Source Inc.) in toluene to give final concentrations of 1, 3, and 5 mg/ml, then the solutions were stirred for 48 hr. Gold salt precursor $HAuCl_4.3H_2O$ was added at a loading rate of 0.1, 0.3 and 0.5, as is required (amount of gold salt per P2VP unit). The solution was left stirring for another 24 hrs. Silicon wafers having around 2 cm × 1 cm in size were obtained by cutting the silicon wafer into small pieces, washed by sonication in water, isopropanol and acetone and finally dried under a stream of nitrogen prior to being dipped in the micellar solution. Au-ions loaded micelles formed as a monolayer on silicon substrate by dip-coating the wafers into the micellar solution and retracting at the adjusted speed of the dipcoater. Finally, the substrates were exposed to oxygen plasma for 2 hrs., in order to burn off the polymer and reduce gold ions to form gold nanoparticles.

2.2 Micro-pattern of gold nanoparticles on silicon by microcontact printing (μCP)

PDMS stamp preparation

Poly dimethysiloxane (PDMS) stamp was replicated using (20 - 10 – 5) micro-structured silicon master. The master was fluorinated with trichloro(1H,1H,2H,2Hperfluorooctyl) silane 97% (Sigma–Aldrich, Munich, Germany) prior to use in replication. Then the (10:1) (v/v) mixture of silicon elastomer (Sylgard 184, Dow Corning) and the curing agent were prepared and degassed for 15 min. in the desiccator. PDMS prepolymer was then drop casted on the master and cured at 120 °C for 2 hrs. Finally, the stamp was pealed of from the master with tweezers, and stored under inert atmosphere.

Microcontact printing (μCP) and micro-pattern formation

Silicon substrates were washed by sonication in a (1:1) (v/v) mixture of water and acetone for 10 – 15 min., dried under a stream of nitrogen and subsequently

immersed in a piranha solution at 120 °C for 1 hr. The silicon substrates were immediately washed with deionized water and dried under a stream of nitrogen. PDMS stamp was inked for a couple of minutes in a 1% aqueous solution of aminopropyltriethoxy silane, then dried using a stream of nitrogen before coming into contact with the activated silicon substrate for 15 – 20 seconds. For silanizing the substrates with PEG silane, toluene containing 1% of triethylamine (as a catalyst) and 3 mM of PEG-silane were placed in a flask under inert atmosphere. The substrates were then immersed in the solution and the reaction was allowed to proceed at 60 °C for 18 hr. As soon as the reaction was over, the wafers were taken out, sonicated in toluene, ethanol for 5 min. each. Finally, they were washed with deionized water and dried by nitrogen flow. The gold nanoparticles were subsequently allowed to self-assemble onto the surface of silicon wafers by immersing the substrates into gold nanoparticles solution for 2 hrs, thus gold nanoparticles selectively bind to amino group forming micro- pattern of gold nanoparticles.

2.3 Self-assembly of different nanostructures onto amino-silanized silicon substrates

Amino-silanization of silicon substrates

Silicon substrates were washed by sonication in water, isopropanol and acetone, dried under a stream of nitrogen and then immersed in piranha solution for 30 min. They were then washed again with water and isopropanol, dried under a stream of nitrogen, and placed in a sealed desiccator along with a vial containing several drops of 3-aminopropyltrimethoxy silane. (97%, Sigma Aldrich). The silanizing agent was allowed to deposit on the surface of the substrates as soon as the desiccator was saturated with silane vapor after evacuating the chamber. After 2 hrs. the desiccator was opened and the substrates were first rinsed with toluene to remove any unbound silanizing molecules from the surface, then rinsed in isopropanol and finally dried under a stream of nitrogen. The silanized silicon substrates were characterized using water contact angle measurements and ellipsometry to measure the thickness of the silane molecular layer.

The general procedure for self-assembly process is as follows:

Amino-silanized silicon substrates were washed with water, isopropanol and acetone and finally dried under a stream of nitrogen prior to their use in the self-assembly process. The substrates were then immediately immersed in the NPs solution for a period of time ranging from 1 hr to 3 days, depending on the concentration of the nanoparticles solution. Next, they were washed with water, isopropanol and acetone and dried under a stream of nitrogen.

Electroless gold plating

The electroless plating experiment was performed as follows: the respective substrates were immersed into aqueous gold growth precursor solution composed of (0.1% w/w) $HAuCl_4.3H_2O$ and (0.2 mM) $NH_2OH.HCl$ as a reducing agent. After 3 min. of immersion time, the substrates were taken out, rinsed with water, isopropanol and acetone and blown dry with nitrogen.

3. Results and discussion

3.1 Silicon – Au NPs substrates by "block copolymer micelle" (BCM) nanolithography

3.1.1 Block copolymer micelle solution

Within the frame of the current project, the potential application of BCM nanolithography of generating highly ordered specific sites for biofunctional molecules immobilization on a conductive silicon substrate is determined by which PS-b-P2VP polymer is used as a polymeric template or "nanoreactor". These polymers consist of two blocks: hydrophobic (poly styrene) and hydrophilic (poly (2-vinylpyridine). Due to the exclusivity of toluene solvent to polystyrene and not to poly (2-vinylpyridine), reversed micelles are formed. The hydrophilic block (Poly (2-vinylpyridine) forms the micellar core with coordinated gold ions, while the hydrophobic one (polystyrene) forms the corona. Silicon substrates were dipped into the micellar solution with a certain polymer concentration and retracted, employing various retraction speeds to form a film of micelles on silicon surface. The substrates were then treated with oxygen plasma to reduce the gold from its salt precursor and to burn off the polymeric matrix. Schematic representation for BCM approach is illustrated in Figure 27.

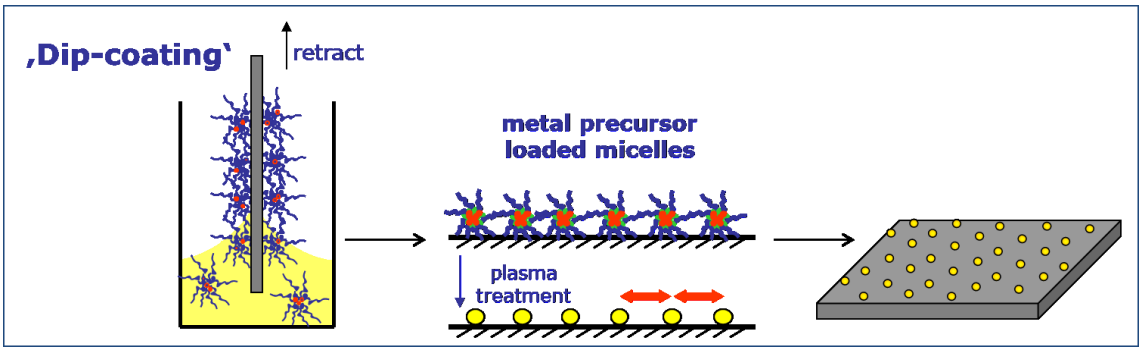

Figure 27: Schematic representation for "block copolymer micelle approach"[10]

In the context of our approach to biofunctional molecules immobilization, a number of parameters were studied that supposedly have a certain influence on the generated nanoparticles size and/or spacing and are considered to be essential criteria in the immobilization process (see what was written in chapter 1; biofunctional molecules on gold surfaces). These parameters are: the effect of gold loading on the size of the

generated gold nanoparticles, the effect of retraction speed, density and age of BCM solution on the interparticle distances.

3.1.2 Controlling Au NPs size by regulating Au loading in the BCM solution

In the course of BCM solution preparation, gold salt precursor was added in different loading amounts to different micellar solutions with the same age and density. This was done to investigate the size of the resulting nanoparticles. The result is indicated by SEM images as shown in Figure 28.

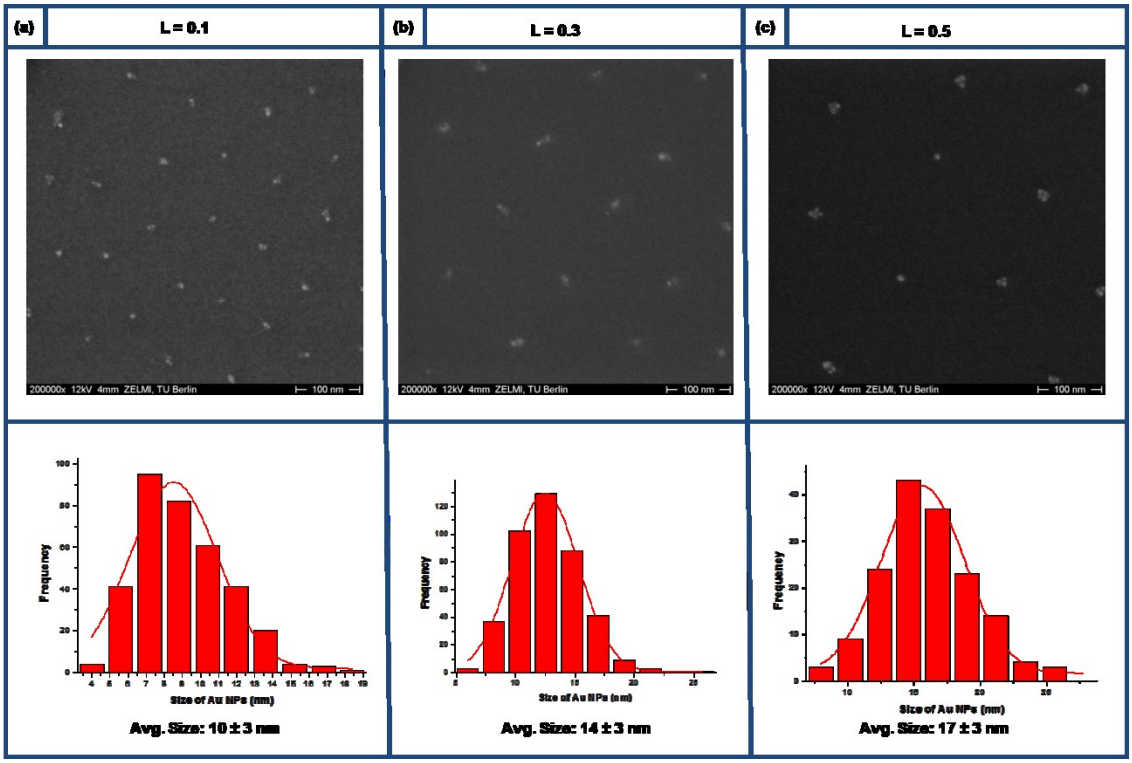

Figure 28: SEM images showing Au NPs size variations based on different Au loading (L); a) L= 0.1, b) L= 0.3 and c) L= 0.5 and their corresponding size distribution histograms (The experiment was conducted using a fresh BCM solution has a density of 1 mg/ml and the retraction speed was adjusted at 80 mm/min)

As indicated by the above figure, increasing gold salt amount leads to an increase in the generated particle size. The differences remain within a narrow range considering the standard deviation in each measurement. However, it is important here to consider the inaccuracy that might result from the weighing balance, particularly in such a small scale of measurements (in mg's).

On the other hand, the produced gold nanoparticles result mainly as nanoclusters rather than individual nanoparticles (see above images). Nevertheless, the calculated

size was performed for the whole surface area of the binding site regardless of its form as a nanocluster or individual nanoparticle.

3.1.3 Controlling interparticle distances through retraction speed variations

After preparation of the BCM solution, silicon wafers were dipped into the solution, kept there for around 20 seconds to allow the micelles to cover the surface, and then retracted. The retraction speed of the dip-coater was carefully adjusted to a certain value.

Variations in retraction speeds were tested using the same micellar solution to monitor the influence of different retraction speeds on the interparticle distances. SEM images for the resulting nanoparticles revealed that retraction speed hardly has any influence on interparticle space, if standard deviations of the measurements are taken into account. The difference in the average distance for each measurement is lower than the accompanying standard deviation, as shown in Figure 29. This result could be explained by the low mobility of the micelles on the substrate due to the large molecular weight of the polymer composing it. Therefore, the micelles will stick to the substrate and are not affected by the retraction speed.

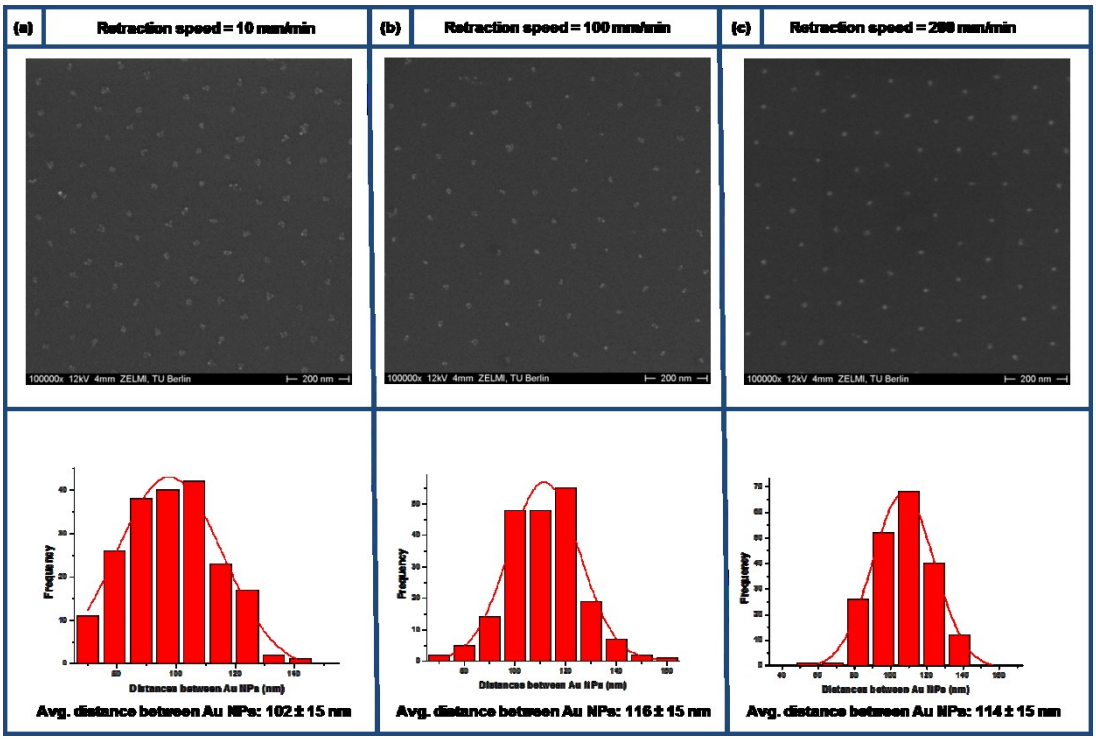

Figure 29: SEM images and their corresponding distance distribution histograms for Si-Au NPs showing differences in the interparticle distances between Au NPs depending on retraction speed variations; (a) 10 mm/min. (b) 100 mm/min. (c) 200 mm/min. (The experiment was performed using 1 mg/ml micellar solution having gold salt loading (L) = 0.3

3.1.4 Effect of density variations of BCM solution on the resulting interparticle distances

BCM solutions were prepared with different concentrations of the polymer, keeping the rest of the parameters the same. SEM characterization shows that density variations of BCM solution have a significant influence on both interparticle distances as well as on the pattern quality. Increasing the density from 1 to 3 mg/ml decreases the interparticle distances from 148 nm to 69 nm, keeping the hexagonal arrangement of the nanoparticles intact. Further increase in the polymer concentration to 5 mg/ml leads to destruction of the pattern quality in addition to further decrease in the interparticle distance to 43 nm. SEM images and their distance distribution histograms are shown in Figure 30.

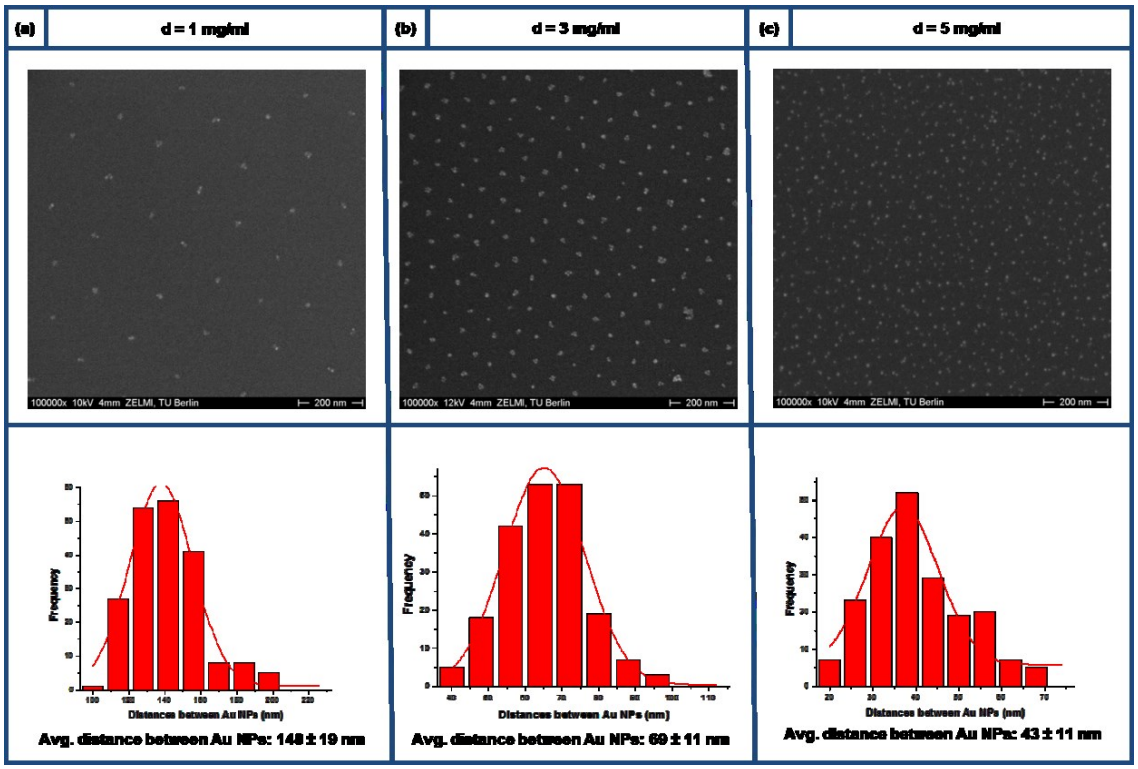

Figure 30: SEM images for Si-Au NPs with different interparticle distances based on density variations of BCM solution (The experiment was conducted using micellar solutions having gold salt loading (L) = 0.3, retraction speed = 80 mm/min)

In order to reasonably explain losing the hexagonal arrangement as a result of increasing the density of BCM solution above 5 mg/ml, TEM measurements were performed for the corresponding micellar film on carbon-coated copper grid as indicated by Figure 31.

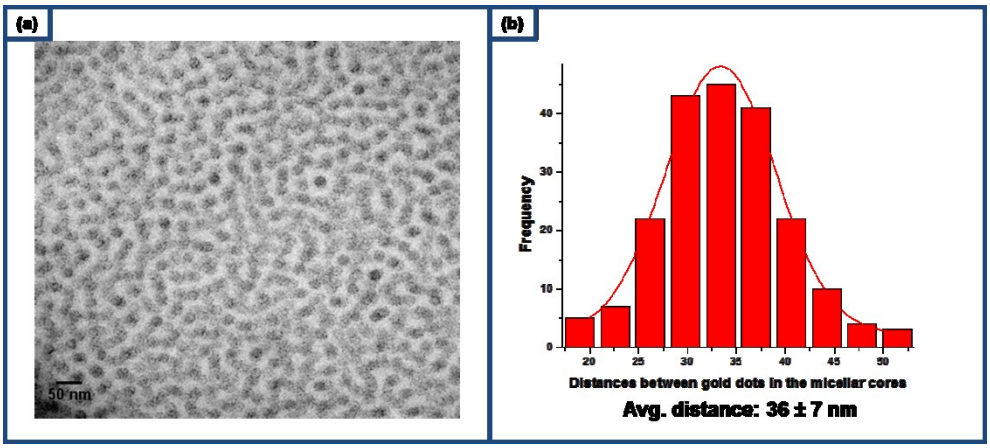

Figure 31: TEM image of the micellar film (a) and the corresponding distance distribution histogram (b)

As shown in the TEM image, micelles show multilayers instead of monolayer indicated by the misordered arrangement of the micellar cores. The average distance between the cores is 36 nm, a figure comparable to the separation between the nanoparticles on silicon after plasma treatment (see Figure 30c).

On the other side, dynamic light scattering (DLS) was implemented in order to shed the light on the hydrodynamic radius of the micelles inside the solution, as seen in Figure 32.

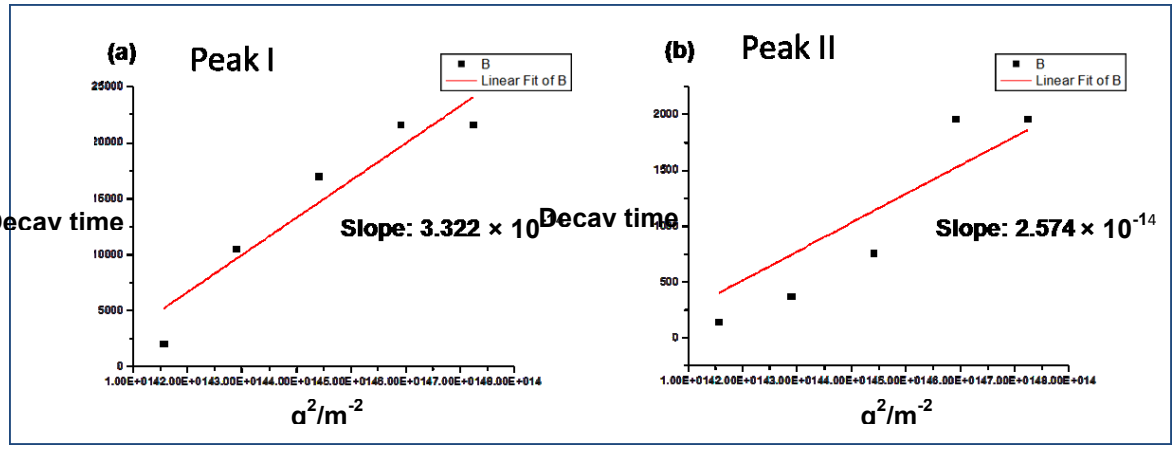

Figure 32: Fitting results out of DLS measurements; two curves are obtained corresponding to two kinds of micelles (a) micelles have a d(H) = 20 nm, and (b) 30 nm (q = (4πnsin(Θ/2))/α)

The hydrodynamic diameter d(H) corresponding to each curve can be calculated by the following mathematical relationship:

$$d(H) = \frac{kT}{3\pi\eta D} \qquad [1]$$

Where: **d(H)**: the hydrodynamic radius, **k**: Boltzmann's constant, **T**: temperature,. **η**: viscosity of the solution and **D** is the translational diffusion coefficient, which can be obtained from the slope of the curve.

Therefore, the hydrodynamic diameter **d(H)** for the first curve equals 20 nm and the second equals 30 nm. This means, we have two kinds of micelles associated with two different hydrodynamic diameters, which are probably responsible for losing the hexagonal arrangement for the corresponding gold nanoparticles on the substrate.

3.1.5 Effect of BCM solution age on the interparticle distances

In order to monitor the age influence on Au NPs pattern, SEM measurement was conducted for gold nanoparticles on silicon after plasma treatment resulted from a freshly prepared BCM solution (i,e just after 24 hrs. from gold loading step). The same solution was then aged for 1 week before conducting another dipping and plasma treatment experiment. SEM measurements revealed that there is an influence caused by ageing the BCM solution results in decreasing the interparticle distances, this result can be attributed to the decrease in the amount of toluene solvent caused by evaporation that lead to an increase in the density of BCM solution (see above). Results are shown in Figure 33.

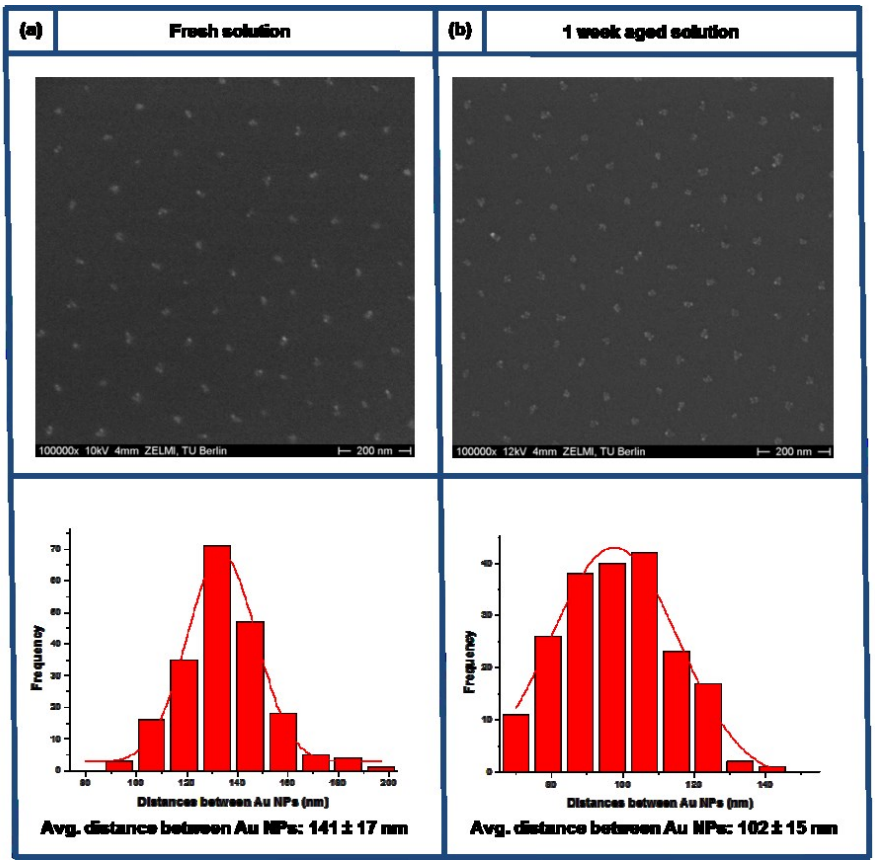

Figure 33: SEM images with the corresponding distance distribution histograms showing age effect of BCM solution on the resulting interparticle distances for freshly prepared solution (a) and 1 weak aged solution (b)

To obtain further insight into micelle formation, SAXS measurements for the micellar solution having a density of 1 mg/ml and gold loading rate (L) of 0.3, reveal, unexpectedly, that micelles did not form once the block copolymer was dissolved in toluene. Instead they formed as soon as gold salt was added to the micellar solution; the addition of gold salt precursor initiates micelle formation. Curves result from SAXS analyses are shown in Figure 34.

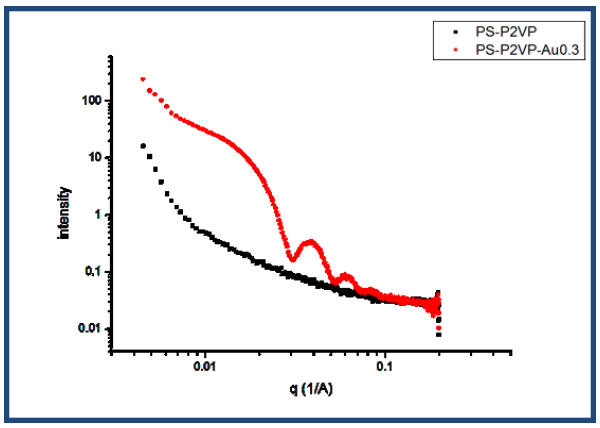

Figure 34: SAXS measurements for the micellar solution

*3.2 Micro-pattern of gold nanoparticles on silicon by microcontact printing (μCP)**

Micro-pattern of gold nanoparticles on a silicon surface was generated by inking a micro-structured PDMS stamp with aminopropyltriethoxy silane, then by bringing it into contact with an activated silicon surface. This process produced a pattern of amino-silanized silicon substrate. Another silanization process using polyethylene glycol (PEG) silane was then performed in the areas where no amino silane exists, leading to a micro-pattern of amino silane as opposed to PEG-silane. Treating the whole assembly with gold nanoparticles solution led to selective adsorption of gold nanoparticles on the areas terminated by amino functionality driven by the high affinity of amino functional group towards binding to the gold nanoparticles. Schematic representation for the process is illustrated in Figure 35.

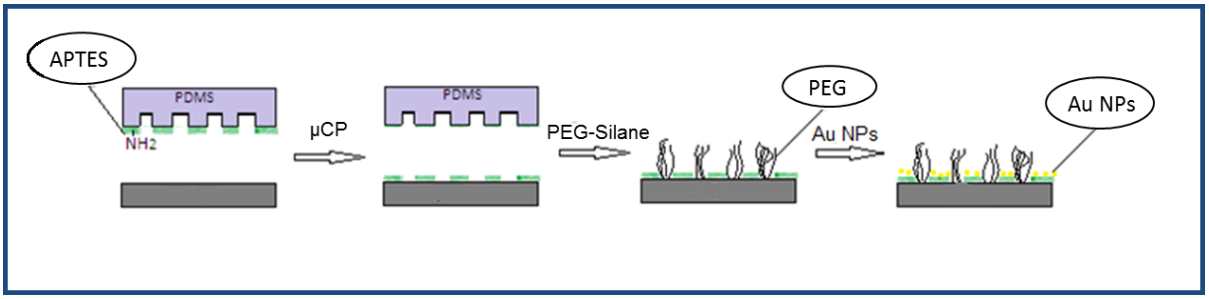

Figure 35: Schematic drawing for micro-pattern of gold nanoparticles through micro contact printing and self-assembly approach (Figure is taken from master thesis of Cigdem Yesildag)

The micro-pattern of gold nanoparticles was characterized using SEM (see Figure 36), which shows the eventual substrate confirming the successful patterning strategy by exhibiting micro-pattern composed of gold nanoparticles. An image of higher magnification (Figure 36b) shows the details of the boundary line between two alternating areas, one with high gold coverage and the other one with poor coverage, easily recognized from the image. The final step of the pattering strategy involves selective self-assembly of gold nanoparticles onto amino-functionalized silicon substrate, which resides within micro-pattern areas, thus forming a monolayer of gold nanoparticles. Additionally, amino functionality shows high affinity toward gold binding. The resulting micro-pattern of gold nanoparticles therefore shows high surface coverage of the nanoparticles accompanied by small interparticle distances of around 20 nm. Conversely, gold nanoparticles were rarely found in the adjacent

*This work was done by a master student in Lensen Lab (Cigdem Yesildag)

areas passivated with PEG silane, due to the relative inertness of PEG toward gold binding.

The μCP strategy coupled with self-assembly of Au NPs on the substrate offers the advantage of having a monolayer formation instead of multilayers. These layers result normally, especially at the edges of the stamp, as a consequence of direct μCP of gold on the substrate (see introduction of this chapter).

The potential value of this work lies in providing simple, bench top technique for the micro-patterning of gold nanoparticles onto a conductive silicon substrate that can be used for patterned immobilization of proteins.

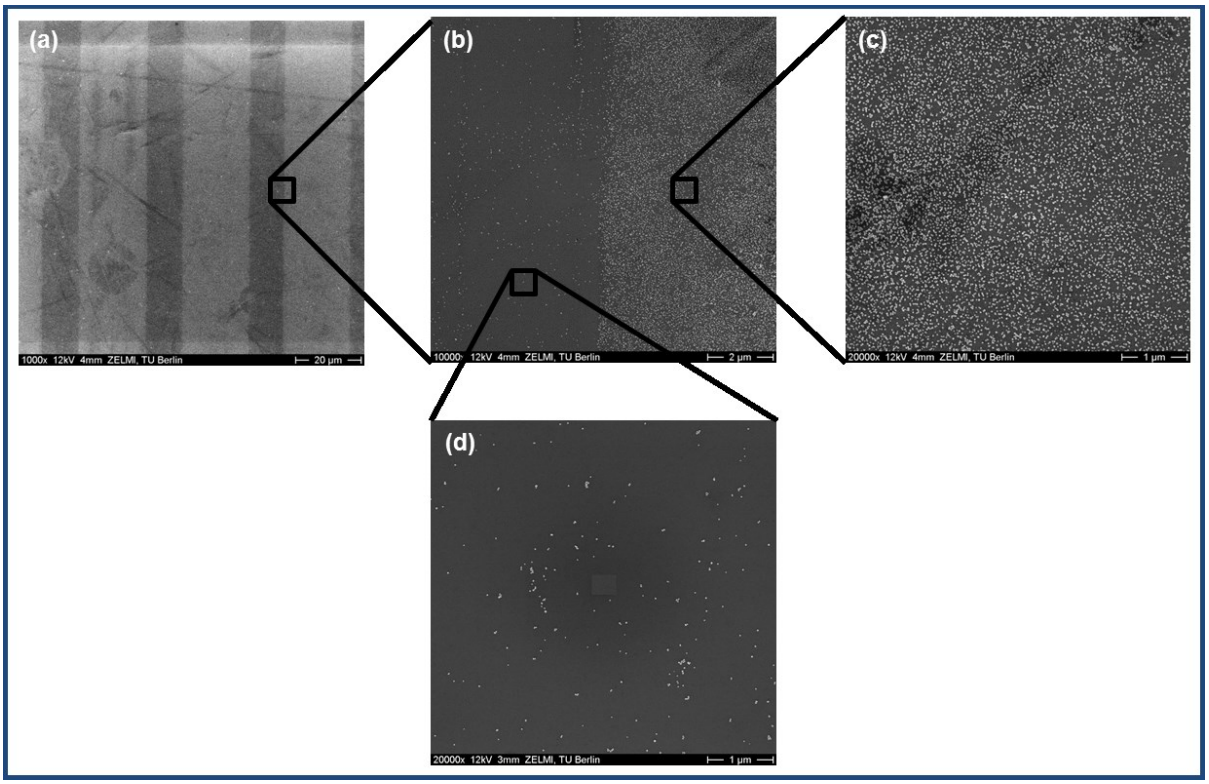

Figure 36: SEM images for micro-pattern of gold nanoparticles (a), magnified image for the boundary area (b), gold nanoparticles reside within the micro-pattern (c) and gold nanoparticles rarely found outside the micro-pattern (d)

One limitation that emerges is the non-selective adsorption of some gold nanoparticles on the area where PEG silane is supposed to be, as shown in Figure 36d. The explanation for this observation might be the fact that PEG silane molecules do not cover the whole area between the micro-pattern. The concentration of PEG silane and/or the reaction time could be increased to improve these results.

3.3 Self-assembly of different metal nanostructures onto amino-silanized silicon substrates

Gold nanostructures, in addition to other metal nanoparticles (silver and silver gold core-shell nanoparticles) that were prepared, (see chapter 2) self-assembled onto silicon substrates terminated by amino-functionality guided by the high affinity of those nanoparticles toward amino group. Self-assembly process is described in Figure 37.

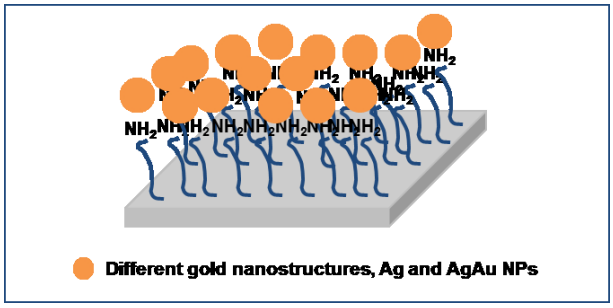

Figure 37: Self-assembly process of Au nanostructures, Ag and AgAu NPs onto amino-functionalized silicon surface

Self-assembly is an easy and spontaneous process aimed at the immobilization of different types of gold nanostructures as well as other metal compositions (silver and silver gold core–shell nanoparticles) that share an affinity towards amino groups with gold. The interesting feature in this binding (amino group toward metal nanoparticles) is the relative weakness compared to the strong binding exhibited by thiol functionality. This varied binding strength of both functionalities will be greatly advantageous to us, and will be explained in chapter 4.

SEM images showing self-assembly of metal nanostructures onto amino-terminated silicon substrates are shown in Figure 38.

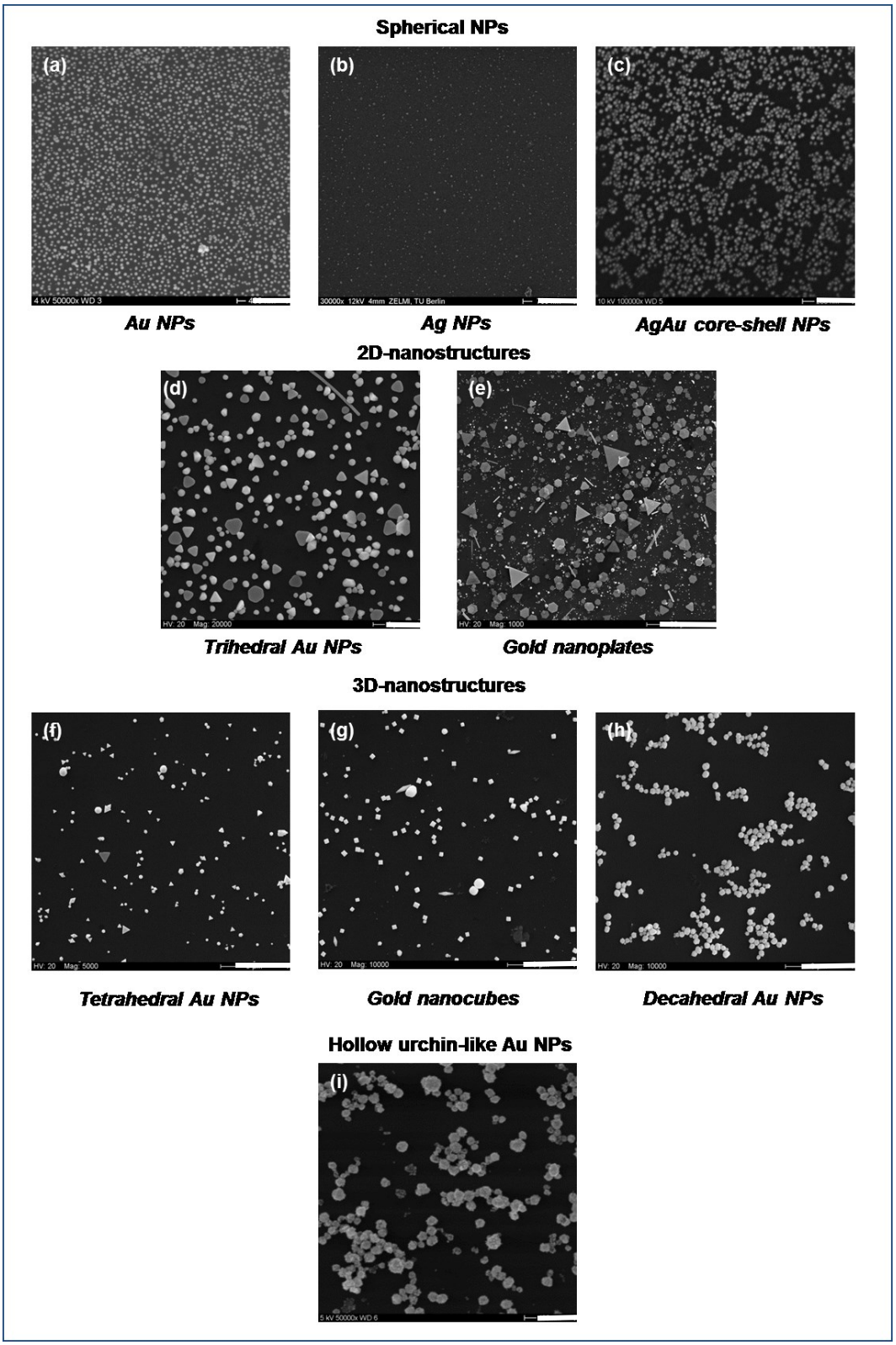

Figure 38: Different nanostructures self-assembled on amino-functionalized silicon (scale bars: a) 400 nm, b) 700 nm, c) 200 nm, d) 1 µm, e) 30 µm f) 6 µm, g) 3 µm, h) 3 µm, i) 400 nm)

By applying the self-assembly process, we were able to immobilize different nanostructures onto 2D conductive silicon substrate. This method allows different morphologies of nanostructures with diverse physical and chemical properties (see chapter 2; introduction) to play a defined role in protein immobilization. Moreover, the strategy can be employed by having high coverage of the nanostructures on the surface (i,e high coverage of binding sites) and hence, high coverage or high density of biofunctional molecules immobilized onto the surface, which can then be adapted to specific protein applications.

However, certain limitations can arise, such as uncontrolled deposition of nanostructures over the surface, which in turn results in agglomeration or multilayer formation of nanostructures. Such limitations can be minimized by controlling the concentration of the nanoparticle solution and/or the required time for the self-assembly process. Furthermore, difficulties were observed in the self-assembly of gold nanorod, resulting in a big agglomeration of nanorods on the substrate. This issue was caused by the CTAB bilayer covering the nanorods, (see chapter 2, nanorods formation) therefore retarding ligand exchange reaction by the amino group at the surface of the nanorod. A suggested solution in this case would be overcoating the nanoparticles with polystyrenesulfonate in order to switch the charge from positive to negative.[22] Protonation of the amino functional groups on silicon would create a positive charge and therefore create an electrostatic interaction between the nanoparticles and the surface.

3.4 Electroless plating proving the accessibility of gold nanoparticles towards functionalization

The electroless plating experiment was implemented in order to prove that gold nanoparticles are still accessible for functionalization after these processes of silanization and after contact with the PDMS stamp (see the introduction of this chapter). In that process, Si Au-NPs substrates are silanized by acrylic silane and then put into contact with the PDMS stamp, after that they were immersed in the growth solution containing more gold ions ($HAuCl_4.3H_2O$) and $NH_2OH.HCl$ acting as a weak reducing agent. Since $NH_2OH.HCl$ is a weak reducing agent, it cannot reduce gold ions without aid from seeds on the substrate. In other words, if gold nanoparticles on silicon are still accessible, they will then be able to act as a catalyst assisting the reducing agent for further gold ion reduction and deposition on their surface.

To this end, four samples were treated with the previously described growth solution: Si-Au NPs without any silanization or contact with PDMS, Si-Au NPs silanized and contacted with non-patterned PDMS, Si-Au NPs silanized and contacted with patterned PDMS and a control sample. Silicon substrate free of gold nanoparticles was treated in the same way as Si-Au NPs (i,e. silanized and contacted with PDMS) acted as a control sample. SEM images were taken for those samples after they were treated with the growth solution, and the results were compared with Si-Au NPs before treatment, as illustrated in Figure 39.

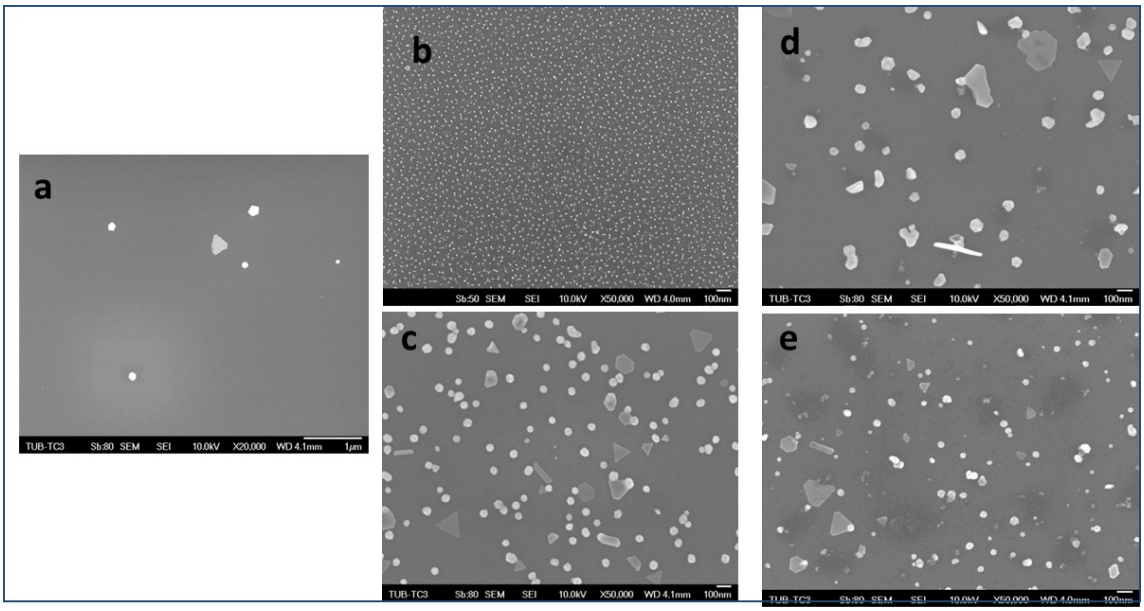

Figure 39: SEM images for silicon sample without Au NPs after silanization and PDMS contact, after growth (a). Si-Au NPs without silanization and PDMS, before growth (b), Si-Au NPs without silanization and PDMS after growth (c), Si-Au NPs after silanization, contacting with non-patterned PDMS, after growth (d), Si-Au NPs after silanization, contacting with patterned PDMS, after growth (e)

It is clear from the above image that Au NPs on silicon show significant growth in their size (compare Figure 39b and 39c) after treatment with the growth solution. By comparing the result of Figure 39c with our silanized and PDMS contacted substrates (Figure 39d and Figure 39e), it is clear that Au NPs on both samples grow in size just as the sample without silanization and PDMS contact does. This indicates that the accessibility of gold nanoparticles on the surface was not affected by silanization and contact with PDMS, and the Au NPs are therefore still available for functionalization.

Moreover, Au NPs were rarely found on silicon having no gold seeds after immersion in the growth solution (Figure 39a) treated in the same way as our samples (silanization and PDMS contact). This indicates that the presence of gold nanoparticles on the surface acting as seeds was essential in catalyzing the reduction process of gold ions coming from the growth solution.

4. Conclusion

A number of patterning strategies were successfully applied in generating nano- and micro-patterns of gold nanoparticles on a conductive silicon substrate. These strategies were: “block copolymer micelle” nanolithography, µ-contact printing and self-assembly producing gold nanoparticles with highly defined size, shape, position and interparticle distances, in turn providing a number of patterned surfaces for biofunctional molecule immobilization.

Periodic hexagonal arrangement of gold nanoparticles was obtained using “block copolymer micelle” nanolithography. Certain control over the nanostructures was achieved when the size of the nanoparticles ranged between 10 to 17 nm, depending on the added amount of gold salt to the micellar solution. Furthermore, the interparticle distances were controlled by density variations of the polymer inside the micellar solution, in which a significant decrease in the interparticle spacing was obtained by increasing the density. However, going further with higher density led to the loss of the hexagonal arrangement of the nano-pattern. Age factor was found to play a role in decreasing the interparticle distances. Conversely, retraction speed variations show no significant influence on the spaces between the nano-pattern.

The micro-contact printing strategy was successfully applied in generating a micro-pattern of gold nanoparticles. This pattern was precisely positioned within micro-stripes exhibiting alternating areas of rich gold nanoparticles beside other areas with poor gold nanoparticle coverage.

The basis of self-assembly was implemented in order to produce a number of metal nanostructures on the silicon surface to be transferred to the surface of polyethylene glycol polymer. This will fall within the scope of chapter 4.

SEM characterization of the resulting nano- and micro-patterns demonstrates the successful application of different patterning strategies in producing a number of patterned surfaces available for biofunctional molecule immobilization.

Investigating the accessibility of gold nanoparticles on silicon for functionalization after silanization and contact with PDMS using electroless plating experiment, reveals the availability of the nanoparticles for further binding.

5. Bibliography

(1) Li, X.; Song, G.; Peng, Z.; She, X.; Li, J.; Sun, J.; Zhou, D.; Li, P.; Shao, Z. *Nanoscale Res. Lett.* **2008**, *3*, 521–523.

(2) Griffith, S.; Mondol, M.; Kong, D. S.; Jacobson, J. M. *J. Vac. Sci. Technol. B Microelectron. Nanom. Struct.* **2002**, *20*, 2768–2772.

(3) Plaza, J. L.; Chen, Y.; Jacke, S.; Palmer, R. E. *Langmuir* **2005**, *21*, 1556–1559.

(4) Melngailis, J. *J. Vac. Sci. Technol. B Microelectron. Nanom. Struct.* **1987**, *5*, 469–495.

(5) Feldman, M.; Sun, J. *J. Vac. Sci. Technol. B Microelectron. Nanom. Struct.* **1992**, *10*, 3173–3176.

(6) Glass, R.; Möller, M.; Spatz, J. P. *Nanotechnology* **2003**, *14*, 1153–1160.

(7) Dai, C.; Wu, Y.; Lee, Y.; Chang, C.; Su, W. *J. Cryst. Growth* **2006**, *288*, 128–136.

(8) Liu, Y.; Hu, H.; Ye, W.; Zhou, F.; Hao, J. *J. Mater. Chem. C* **2013**, *1*, 902–907.

(9) Burmeister, F.; Schäfle, C.; Matthes, T.; Böhmisch, M.; Boneberg, J.; Leiderer, P. *Langmuir* **1997**, *13*, 2983–2987.

(10) Lohmüller, T.; Aydin, D.; Schwieder, M.; Morhard, C.; Louban, I.; Pacholski, C.; Spatz, J. P. *Biointerphases* **2011**, *6*, MR1–12.

(11) Glass, R.; Arnold, M.; Blümmel, J.; Küller, a.; Möller, M.; Spatz, J. P. *Adv. Funct. Mater.* **2003**, *13*, 569–575.

(12) Segalman, R. A. *Mater. Sci. Eng. R* **2005**, *48*, 191–226.

(13) Tseng, Y.; Darling, S. B. *Polymers (Basel).* **2010**, *2*, 470–489.

(14) Daga, V. K.; Schwartz, E. L.; Chandler, C. M.; Lee, J.-K.; Lin, Y.; Ober, C. K.; Watkins, J. J. *Nano Lett.* **2011**, *11*, 1153–60.

(15) Park, J.-E.; Momma, T.; Osaka, T. *Electrochim. Acta* **2007**, *52*, 5914–5923.

(16) Wu, X.; Lenhert, S.; Chi, L.; Fuchs, H. *Langmuir* **2006**, *22*, 7807–7811.

(17) Santhanam, V.; Andres, R. P. *Nano Lett.* **2004**, *4*, 41–44.

(18) Riskin, A.; Dobbelaere, C. De; Shan, L.; Boyen, H. G.; Haen, J. D.; Hardy, A.; van Bael, M. K. *J. Phys. Chem. C* **2012**, *116*, 10743–10752.

(19) Chen, J.; Arafeh, M.; Guiet, A.; Felkel, D.; Loebus, A.; Kelleher, S. M.; Fischer, A.; Lensen, M. C. *J. Mater. Chem. C* **2013**, *1*, 7709-7715

(20) Chen, J.; Mela, P.; Möller, M.; Lensen, M. C. *ACS Nano* **2009**, *3*, 1451–6.

(21) Tinguely, J.-C.; Charron, G.; Lau-Truong, S.; Hohenau, A.; Grand, J.; Félidj, N.; Aubard, J.; Krenn, J. R. *J. Colloid Interface Sci.* **2013**, *394*, 237–242.

Chapter 4

Patterning of gold nanoparticles on polyethylene glycol hydrogel

A particular combination of gold nanoparticles with polyethylene glycol (PEG) hydrogel will be described. The first and the second part of this chapter deal with the transference of gold nanoparticles to the surface of polyethylene glycol hydrogel.

The first part involves the transference of gold nanoparticles obtained by BCM (chapter 3) to the surface of PEG hydrogel by swelling removal in water.

The second part gold nanoparticles with different shapes (see chapter 2) were transferred to the surface of polyethylene glycol (PEG) hydrogel, after being self-assembled onto a functionalized silicon substrate terminated with amino silane molecules.

The third part describes the formation of micro-pattern of alternating areas of PEG-hydrogel and composite material composed of Au NPs and PEG by means of a novel method based on **f**ill **m**olding **i**n **c**apillaries **(FIMIC).** This method of fabrication generates a three dimensional platform for specific biofunctionalization of gold nanoparticles within the hydrogel matrix.

Jingyu Chen, Vera Schulte, Yibing Hu, **Manar Arafeh**, Amandine Guiet, Axel Loebus, Petra Mela, Diana Felkel, Anna Fischer, Susan Kelleher, Marga Lensen, Adhesion and Spreading of Cells on PEG with Imbedded Patterns of Gold Nanoparticles *(Manuscript in preparation).*

Manar Arafeh, Gonzalo de Vicente, Axel Loebus and Marga C. Lensen, Embedded Micro-pattern of PEG – Gold Nanoparticles Composite Hydrogel for Biomedical Applications *(Manuscript in preparation)*

Manar Arafeh, Cigdem Yesildag and Marga C. Lensen, Transference of Different Shapes of Gold and Silver Nanoparticles from Silicon Substrate to the Surface of Polyethylene Glycol Hydrogel *(Manuscript in preparation)*

1. Introduction

Polyethylene glycol (PEG) is an oligomer or polymer of ethylene oxide, the structure of which is shown in Figure 40[1].

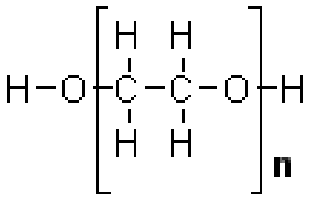

Figure 40: Chemical structure of polyethylene glycol

Polyethylene glycol hydrogel is a very popular material widely used in material science application due to its highly attractive biocompatible and nontoxic properties, as well as its deformable and transparent nature.[2]

Concerning the intended scope of this work, i,e biofunctional molecules immobilization, PEG hydrogels can perform a central role as non-adhesive materials for proteins. A system composed from PEG hydrogel as a protein repellent background and metal nanostructures on the surface, providing specific binding sites for proteins immobilization, is fabricated.

It is worth mentioning that controlling protein adsorption on the surface is a high priority in many fields[3] including nanobiotechnology, since nonspecific adsorption of proteins is considered to be a critical issue. Therefore, many techniques have been developed to create a pattern of inert surfaces based on polyethylene glycol hydrogel and other areas where protein adsorption is promoted.[4] Examples of these techniques include the formation of polyethylene glycol hydrogel using photolithography[4,5] or the fabrication of microstructure-based polyethylene glycol within 3D-microfluidic channels.[6] The use of a self-assembled monolayer of (EG) fabricated over a metal surface through thiol moiety has also been reported.[7] Furthermore, surface initiated polymerization method has been used to synthesize EG functionalized polymer brushes with tunable thickness.[8]

However, PEG hydrogels are more stable than PEG molecules prepared by self-assembly methods and also boast long-term resistence.[9]

The aim of this chapter is to create strategies in order to minimize the chance for nonspecific protein adsorption. Our strategy will be the fabrication of diverse systems

based on metal nanostructures serving as anchoring points for selective functionalization and therefore, proteins immobilization and PEG hydrogel polymer serving as protein non-fouling background.

Therefore, the contents of this chapter have three main themes: (1) focus on the transference of gold nanoparticles fabricated by ″block copolymer micelle nanolithography″ (see chapter 3) from silicon substrate into PEG hydrogel polymer by swelling in water. (2) Broadening the scope of this point by involving other metal compositions sharing the same chemical behavior toward certain functional groups (amine and thiol) with gold, as well as other gold morphologies to form a part of nanostructures/polymer system. (3) Patterning protocol for PEG polymer forming protein-repellent areas versus other areas composed of PEG prepolymer and citrate-capped gold nanoparticles where protein adsorption is supposedly promoted. The latter patterning strategy was fabricated by **f**ill **m**olding **i**n **c**apillaries (**FIMIC**), a method that has recently been developed in our group.

2. Experimental

Details concerning synthetic protocol for citrate capped gold nanoparticles solution as well as preparation of gold nanoparticles on silicon substrate obtained by ˝block copolymer micelle nanolithography˝ are described in chapters.2 & 3, respectively.

2.1 Transference of Au NPs from silicon substrate to the surface of polyethylene glycol hydrogel by swelling removal in water

Prepolymer solution composed of *Polyethylene glycol diacrylate (PEG575)* (Sigma Aldrich, Mw 575 Da) and 1% of 2-hydroxy-4'-(2-hydroxyethoxy)-2-methyl-propiophenone photoinitiator, (98%; Sigma Aldrich, Mw 224.26 Da) (PI) was dropped on the Si-Au NPs substrate prepared by the BCM nanolithography method, then subsequently UV cured in an oxygen free atmosphere. After 30 minutes the PEG replica was removed by swelling in water for 30 minutes.

2.2 Transference of different shapes of Au NPs from silicon substrate to the surface of PEG hydrogel

Samples of different shapes of gold nanoparticles obtained by self-assembly on amino-silanized silicon substrates were prepared, a process described in chapter 3.

Functionalization of the nanoparticles on amino-silanized silicon substrate with 2-propenethiol linker molecule

Silicon substrates were incubated into 2-propenethiol linker molecules, (60%, Sigma Aldrich), for 3 hrs. then washed by in ethanol immersion for 30 minutes to remove the excess linker, then dried under stream of nitrogen.

Transference process to the surface of PEG hydrogel

PEG575 prepolymer with 1% photoinitiator was drop casted onto silicon surface and covered with a glass cover slip, cured under UV light for 1 hr., then PEG hydrogel replica was pealed from the silicon surface by swelling in water for 1 hr. The PEG replicas and silicon substrates were both characterized after transference using SEM.

2.3 Micro- and nano- surface patterning of PEG-gold nanoparticles composite

Preparation of micro-patterned PEG575 replica

Micro-structured silicon master was fluorinated with trichloro(1H,1H,2H,2Hperfluorooctyl) silane 97% (Sigma–Aldrich, Munich, Germany) prior its use in replication, then cleaned by rinsing in water, isopropanol and acetone, and dried under a nitrogen stream.

A drop of PEG575 precursor along with 1% photoinitiator was placed on the top of the silicon master, covered by a glass cover slip, and then subjected to UV curing for 10 minutes in an oxygen free atmosphere. Next, the replica was peeled off of the surface of the master to be used in the **FIMIC** process.

PEG575- Au NPs composite synthesis

10% by weight of Au NPs solution was added to the prepolymer of PEG575 with 1% photoinitiator, and the whole mixture was sonicated for a few minutes and then placed in the oven at a temperature above 100 $^{\circ}$C for a couple of minutes in order to let the water evaporate from the mixture.

*Micro-sized pattern of PEG – Au NPs composite by **FIMIC** process*

PEG575 replica was cut down into small pieces, placed upside down on a clean glass slide, in which the replica structures were totally in contact with the glass. A small drop of the PEG – Au NPs composite was placed near the edge of the replica and, by means of a pipette tip; the small drop approached slowly the edge of the replica, allowing the composite liquid to fill the replica channels by aid of the capillary action. The whole system composed of the PEG replica and the composite filling were cured under UV light for 20 min. Finally, the sample was pealed off of the glass and turned upside down for further characterization.

2.4 Characterization techniques

Optical microscopy

Light microscopy images were taken with an inverted Axiovert 100A Imaging microscope (Carl Zeiss, Goettingen, Germany) using an AxioCam MRm digital

camera and analyzed using the AxioVisionV4.8.1 software package (Carl Zeiss, Goettingen, Germany).

*Scanning electron microscope (**SEM**)*

Scanning electron microscopy (SEM) was performed on LEO 982 offered by ZEISS Company, the optical parts of the microscope from GEMINI Optics. The samples were carbon-coated prior measurements, which were performed using Inlens detector operating at 15.0 kV.

*Transmission electron microscope (**TEM**)*

Transmission electron microscope (TEM) images were acquired on the TECNAI G²20 S-TWIN microscope operating at 200 kV, with point of resolution 0.24 nm.

Confocal laser scanning microscope

Images that were acquired by confocal microscopy were recorded using Leica TCS SP5 II Confocal Microscope (Leica, Wetzlar, Germany) with a 20x objective. An excitation wavelength of 488 nm was used and the detector was set in the range of 498 - 841 nm for fluorescein. Images were analyzed and processed utilizing Leica (LAS AF) lite software.

*Atomic force microscope (**AFM**)*

An atomic force microscope was used (JPK instruments, Nanowizard II) to measure the topography and surface elasticity of the samples in a dry state.

Topographical imaging

Imaging was done in intermittent contact mode using silicon nitride cantilevers (Tap300GB – G), k ≈ 20 – 75 N/m, f0 ≈ 200 - 400 kHz; Nanoworld Innovative technologies) with gold coating. Images were edited with NanoWizard IP Version 3.3a (JPK instruments).

Force mapping

Force mapping was conducted using the same scanning probe microscope (JPK instruments, Nanowizard II) and silicon nitride cantilevers (ContAl) with aluminium reflex coating (k ≈ 0.07 - 0.4 N/m, f0 ≈ 9 - 17 kHz; Nanoworld Innovative technologies). Images were processed using NanoWizard IP Version 3.3a (JPK

instruments). ContAl tip (NanoWorld) exhibit a cone shape with a half cone angle of 20° - 25° along the cantilever axis. The tip-geometry has been taken into account by applying the Bilodeau formula[10] for force distance curves fitting. The fitting was implemented using Nanowizard IP software to obtain E-Modulus values.

Rheology

Rheological measurements were performed using Gemini 200 HR (Malvern Instruments). Measurements were taken at room temperature and the samples were swollen for at least 12 hrs. prior measurements. The frequency values were ascertained within a range of 0.01 to 10 Hz. 1 Hz for applied frequency and 0.0001 – 0.01 for deformation value (γ) in respect to all measured samples. The bulk elasticity was calculated according to the following equation[11]:

$$\mathbf{E = 3\ G'}$$

E is the Young's Modulus and **G'** is the Storage Modulus. Each material composition was measured at least 3 times.

Ellipsometry

Thickness measurements were conducted using Multiscope ellipsometry from Optrel GbR (Sinzing, Germany) in Null-ellipsometry mode.

Water contact angle measurements

Water contact angle measurements were taken using OCA 20 from Data Physics Instruments GmbH, (Filderstadt, Germany).

3. Results and discussion

In this section, three strategies to fabricate gold nanostructures as specific anchoring points for proteins on the protein's non adhesive surface are described. The first two strategies involve the transference of nanoparticles positioned on silicon substrate either by BCM method, where the nanoparticles were patterned on the substrate and the whole pattern then transferred, or by self-assembly method, where the nanoparticles were attached to a chemically functionalized silicon surface with versatility in size, shape and composition.

The third strategy employs a soft lithographic method to create a micro-pattern of a composite material composed of PEG and gold nanoparticles. Protein immobilization should take place on the areas where the gold is.

3.1 Transference of Au NPs from silicon substrate to the surface of polyethylene glycol hydrogel by swelling removal in water

Gold nanoparticles on silicon (Si-Au NPs) substrate obtained by "Block copolymer micelle nanolithography" (BCM) (see chapter 3 for detailed preparation of Si- Au NPs by BCM) were transferred to the surface of polyethylene glycol hydrogel by swelling in water, shown in Figure 41.

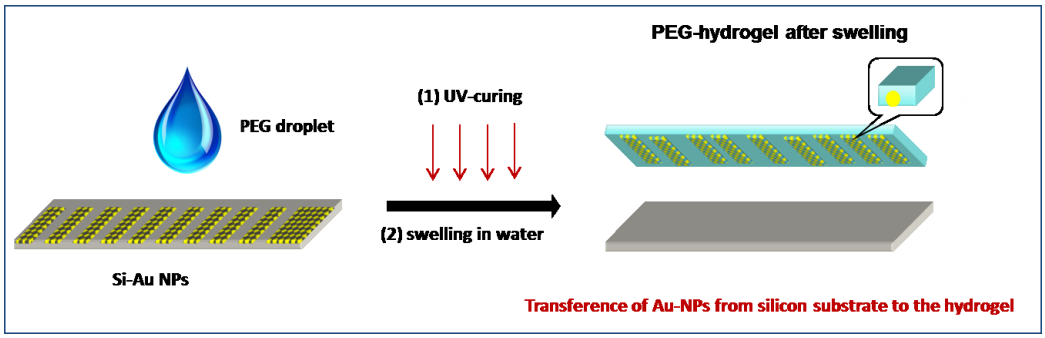

Figure 41: Scheme illustrating the transference process of Au NPs to the hydrogel surface by swelling removal in water

A drop of prepolymer solution composed of PEG575 with 1% photoinitiator, and without any cross linker, was drop casted onto Si-Au NPs, then UV-cured under a nitrogen atmosphere. The PEG replica was peeled off by swelling removal in water and characterized using SEM, as shown in Figure 42.

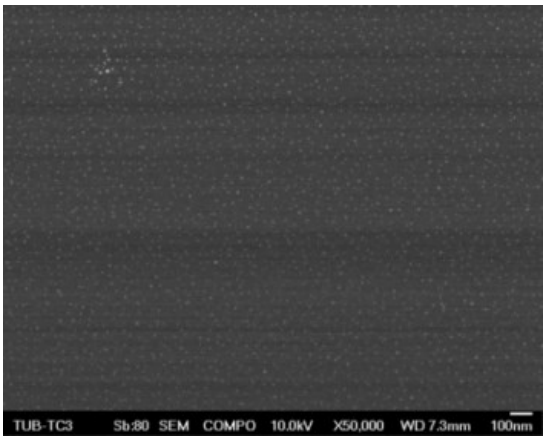

Figure 42: SEM image for Au NPs on PEG replica after transference in water

The developed transference strategy is very quick, simple and proceeds without the assistance of any linker molecule. Moreover, most of the nanoparticles were successfully transferred, as indicated by Figure 43, which shows the gold nanoparticles on the silicon substrate before and after transference.

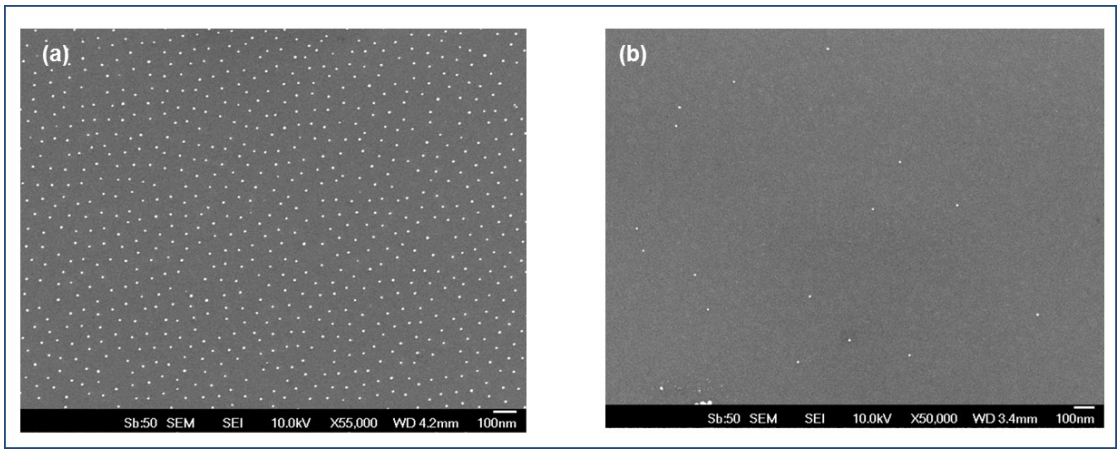

Figure 43: SEM images for Si-Au NPs before (a) and after (b) transference to the hydrogel

EDX measurement on PEG replica also revealed the presence of gold peak, as shown in Figure 44

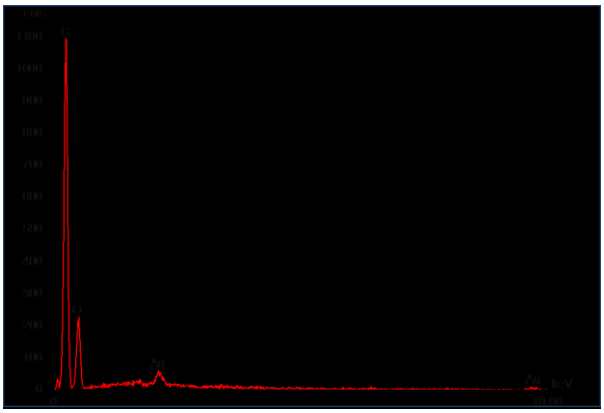

Figure 44: EDX spectrum of Au on PEG hydrogel replica

A number of advantages are created as a consequence of Au NPs originating from Si-Au NPs substrate, prepared by BCM. Such advantages include the ability to exercise a certain amount of control over size of nanoparticles and their interparticle distances (see chapter 3 for more details). Moreover, micro-pattern of nanoparticles on silicon could be obtained using a combination between the BCM method and other methods such as μ-contact deprinting[12,13]. Therefore, it would be feasible to transfer that pattern onto the PEG surface, as described above.

Since the transference process of the nanoparticles proceeds without the aid of any linker molecule, the driving force behind gold nanoparticle transfer is based on pure physical interaction between PEG hydrogel and the nanoparticles. It is therefore possible that the nanoparticles either pop off the PEG surface into the water or migrate to the interior through the hydrogel meshes.

Since the stability of the nanoparticles on PEG replica is a major issue, particularly if a request to use this kind of substrate for proteins immobilization depends on the ability of the nanoparticles to efficiently anchor proteins, consequence this issue must be investigated.

PEG replica was leaving the silicon substrate as a consequence of its swelling in water; therefore this process of water uptake could also have a certain influence on the transferred nanoparticles. This can happen either by increasing the hydrogel mish size as a result of the penetration of the water molecules through the hydrogel network chains which then promotes the nanoparticles migration to the hydrogel interior, or by increasing the softness and the volume of the hydrogel. We expect that by increasing either the hydrogel softness or volume as a consequence of its swelling

in water to weakness the secondary interaction between the PEG replica and the nanoparticles which cause the nanoparticles to pop off the PEG surface into the solution.

In order to investigate nanoparticle stability and to assess the swelling behavior of PEG575, a swelling test was conducted, as shown in Figure 45.

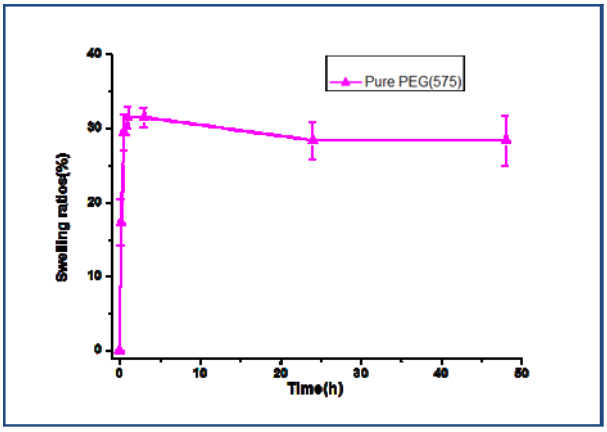

Figure 45: Swelling test of PEG575

It can be observed from the above curve that, during the time interval of 30 minutes up to 48 hr., the swelling ratio of the hydrogel was almost constant. As a consequence, the mesh size – which is an inherent property of the swelling ratio – of the hydrogel net is unlikely to be affected during this period. This indicates that, if Au NPs could be found after 30 minutes (the required time for our swelling transference process), then they are not expected to migrate afterwards from the replica surface through the hydrogel meshes influenced by swelling process. In the same way, we expect that the secondary interaction that bind gold nanoparticles to the hydrogel surface not to be affected as a consequence of PEG swelling in water. This means that they are unlikely to pop off the surface into the water after 30 minutes time period.

We therefore, conclude that Au NPs are likely to still be available for further functionalization processes after their transference to the PEG replica.

Another consequence of the swelling property of the hydrogel is its influence on the interparticle distances, in comparison to the original silicon substrate, where they are expected to increase as a consequence of the water uptake process.

As the SEM measurement for our sample should be done in evacuated conditions, a dry sample should be used throughout the measurements. Consequently, measuring the distances between the nanoparticles using SEM image cannot predict their separation in the swelling state.

In addition, AFM technique is not the proper method to provide accurate distances between the nanoparticles due to tip's artifacts, which often results in uncertain measurements.

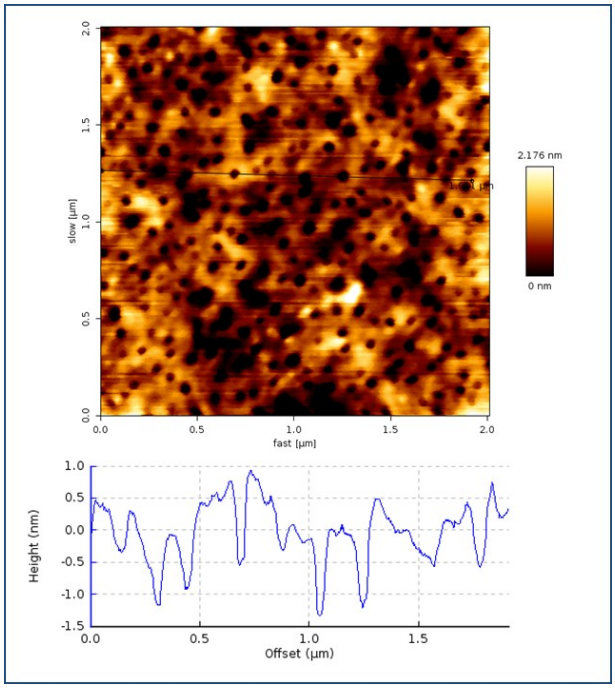

Figure 46: Surface topography of PEG replica shows the indents of Au NPs

AFM characterization of the PEG replica through surface topographical imaging and the resulting cross section profile show unexpectedly that the nanoparticles are not present on the surface. Instead indents of the nanoparticles appear in the image. This finding does not acquiesce with the previous SEM results for the same PEG replica. The explanation for this phenomenon would be that the nanoparticles are not sticking out of the PEG surface. Instead, they are partially entrapped under the Neath of the polymer surface. AFM results are shown in Figure 46.

3.2 Transference of different shapes of Au NPs from silicon substrate to the surface of PEG hydrogel

The previously described method for nanoparticles transfer to the PEG polymer surface offers a quick and simple route for creating specific binding sites for biofunctional molecules' immobilization. A measure of control over size and interparticle distances (protein binding sites) can be achieved, which should influence proteins' spatial orientation over the surface. This control is, nevertheless, restricted to spherical nanoparticles obtained by "block copolymer micelle" nanolithography. This also implies that their size is limited by the loading capacity of the core unit of the micelle.

We would like to introduce another approach to achieve a wider range of possibilities by fabricating a system composed of different morphologies as well as metal compositions of nanostructures on the protein repellent surface of polyethylene glycol (PEG) hydrogels. This strategy utilizes our previously prepared varied nanostructures on the surface of amino functionalized silicon substrate.

Silicon substrates were functionalized by amino-functionality in order to create weak, yet specific anchoring points for metal nanostructures. This was implemented by amino-silanization of silicon wafers (as described in chapter 3). Metal nanostructures were allowed to self-assemble onto amino silanized silicon substrates guided by their high affinity towards amino groups.

Propene thiol linker molecule assists transference process

Metal nanostructures on amino-silanized silicon surface were functionalized with a propene thiol linker molecule. In this process the thiol moiety of the linker binds to the metal surface forming (metal-S) bond, a bond stronger than the metal-amine bond. The other terminal of the linker is a double bond serving as a functional site for radical crosslinking with polyethylene glycol prepolymer precursor upon curing under UV light. The transference process to the hydrogel proceeded based on the relative binding strengths of metal–S versus metal-amine bond.

Figure 47 shows a schematic presentation of the individual steps involved in the transference process of nanostructures to the PEG hydrogel surface. These steps are: amino-silanization of silicon substrate (step 1), self-assembly of different

morphologies of nanostructures onto the surface of amino-silanized silicon (step 2), functionalization of the nanostructures with propenethiol (step 3), drop casting the PEG precursor solution, cured under UV (step 4) and finally, peeling off the PEG replica by swelling in water (step 5).

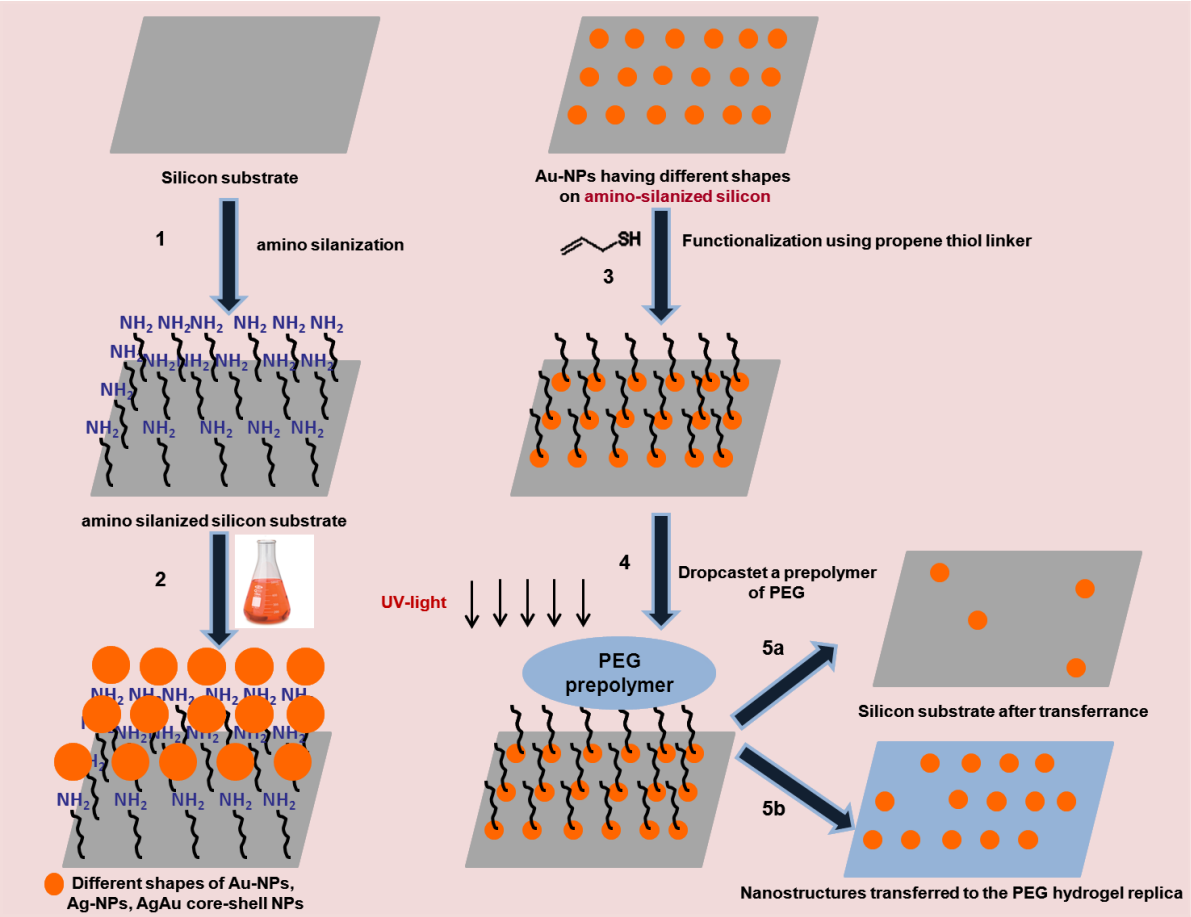

Figure 47: Scheme illustrating transference process of metal nanostructures from silicon substrate to PEG surface

The current strategy aims to create specific binding sites composed of different shapes and nanostructure composition on a protein-resistant background in order to anchor biomolecules. This strategy takes full advantage of the versatile physical and chemical properties of the nanostructures, a versatility expected to play a significant role in terms of biosensors applications (see chapter 2). The real value of this work relies on the feasibility of transferring nanostructures ranging from simple spherical nanoparticles to complex 2D, 3D and hollow urchin-like nanostructures to the PEG surface, shown in Figure 48.

Moreover, this work encourages further studies focused on enhancing binding signals and improving the detection sensitivity of localized surface plasmon resonance

(LSPR) assays, as described earlier. Some groups have shown a relationship between the size of nanoparticles and SPR signal enhancement,[14] supporting other studies based on the investigation of such relationships between the shape and composition of nanostructures.

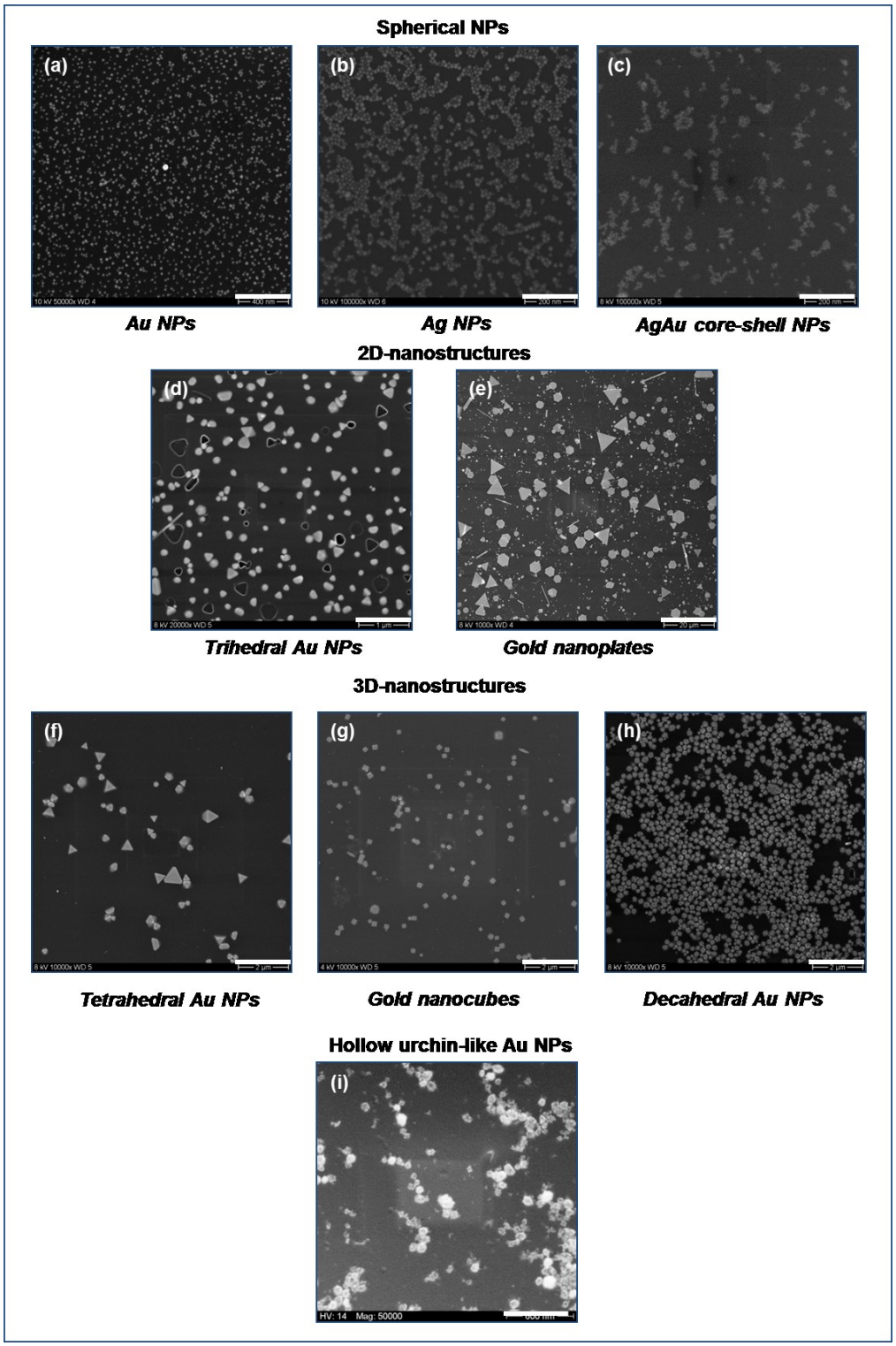

Figure 48: Different nanostructures on the surface of PEG hydrogel after their transference from silicon surface (scale bars: a) 400 nm, b) 200 nm, c) 200 nm, d) 1 µm, e) 20 µm f) 2 µm, g) 2 µm, h) 2 µm, i) 600 nm)

The current strategy of nanoparticle transfer guarantees a high control over a number of parameters such as size, shape and metal composition for the transferred nanostructures, an issue not addressed by the previously reported studies.[2,9,15] However, some challenges still need to be dealt with, such as achieving control over the position and distance between the nanostructures. Some agglomeration of nanostructures exists on the polymer surface as a consequence of similar agglomeration on the original silicon substrate, prepared by the self-assembly method (chapter 3). However, to improve the applicability of our approach, the method could be combined with our newly developed μCP strategy (see chapter 3; μCP). By this, the desired morphology of nanostructures can be self-assembled onto a micro-patterned area of amino functionalized silicon first then it transfers to the polymer surface after being functionalized with the linker molecule. As a result, micro-patterned on PEG surface of arbitrary nanostructure with the desired morphology and/or metal compositions can be achieved.

3.3 Micro- and nano- surface patterning of PEG-gold nanoparticles composite

For surface patterning of PEG and PEG – Au NPs composites, **F**ill **M**olding **I**n **C**apillaries (**FIMIC**), a method developed in our group, is employed. This method combines a micromolding method[16] represented by PEG replica formation with filling the replica micro-channels by another elastomeric material induced by capillary action.[17,18]

This easy bench top technique was applied in order to generate a three dimensional micro-pattern of protein-resistant areas composed of polyethylene glycol hydrogel beside other areas of PEG – Au NPs composite, where Au NPs exist as protein anchoring points within PEG hydrogel matrix.

The stages involved in **FIMIC** process are: *Formation of PEG replica* (step 1), *Preparation of the composite precursor* (step 2), *preparation of the micro-patterned PEG – Au NPs composite* (step 3). The scheme illustrating **FIMIC** process is shown in Figure 49.

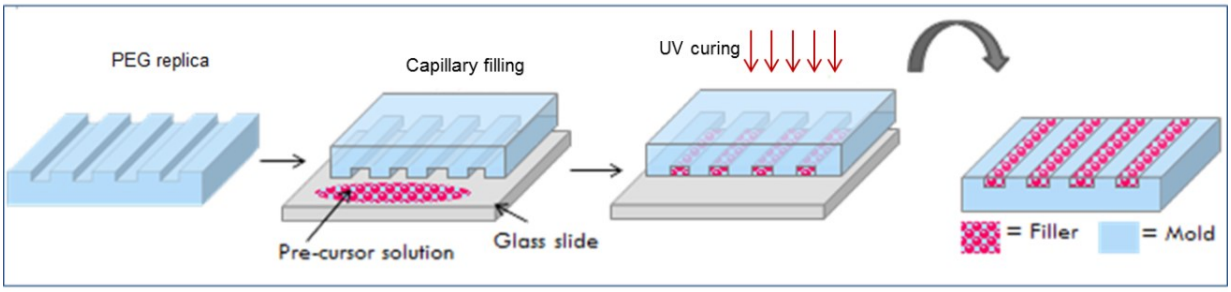

Figure 49: Scheme of micro-patterning of Au NPs composite using FIMIC process

In the initial step, PEG replica was generated using a silanized micro-structured silicon master. A drop of PEG precursor solution was drop casted on the surface of the master and then cured under UV-light. Subsequently, composite solution was prepared by physical mixing of 20 nm citrate capped-Au NPs with PEG prepolymer to be used in filling the micro-channels of PEG replica induced by capillary action.

The whole assembly was cured under UV-light to produce the micro-patterned PEG – Au NPs composite upon peeling off the FIMIC substrate. Characterization was performed for each individual step in the process.

Citrate capped Au NPs solution

Details concerning characterization of Au NPs solution using UV-Vis spectroscopy and TEM measurements are given in Chapter 2.

PEG – Au NPs composite solution

A solution of PEG – Au NPs composite was prepared, as previously described. 10 % of citrate-capped Au NPs was briefly and physically mixed with PEG prepolymer. TEM measurement was performed for the nanoparticles in PEG precursor solution, as shown in Figure 50.

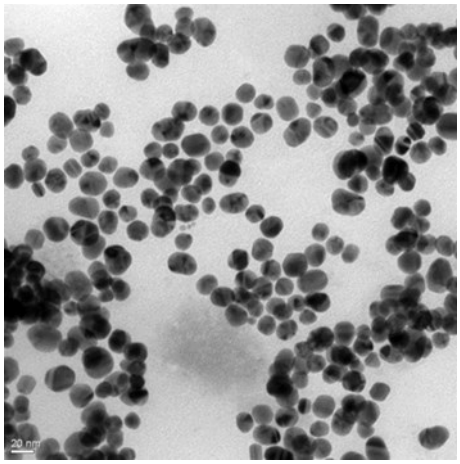

Figure 50: TEM image for PEG – Au NPs composite solution

The above image shows the nanoparticles homogeneously distributed in PEG precursor solution without significant agglomeration, which is an important requirement for further processing.

PEG – Au NPs composite film

A drop of the composite solution of PEG precursor and citrate-capped Au NPs was subjected to UV-curing for 30 minutes and the resulting composite film was characterized by atomic force microscopy, (AFM) as shown in Figure 51.

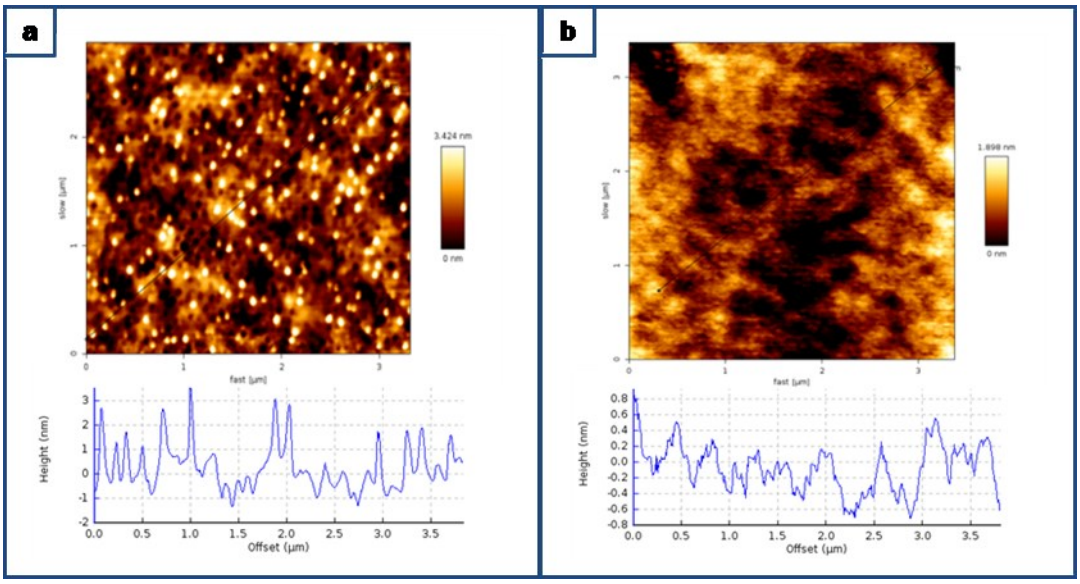

Figure 51: Surface roughness of PEG – Au NPs composite (a) and PEG575 (b)

As expected and appearing in the above figure, PEG – Au NPs composite exhibits a higher surface roughness (around 4 nm) compared to that exhibited by pure PEG575 (1 nm). Moreover, the nanoparticles are sticking out (as shown in the cross section of the composite film Figure 51a), in a manner advantageous to the creation of sites for biofunctionalization.

Micro-pattern of PEG – Au NPs composite

The resulting micro-pattern of polyethylene glycol – Au NPs composite was examined by optical and scanning electron microscopes in order to prove the success of the filling process for PEG micro-channels, as well as to reveal any scum layer formation, indicated by Figure 52. Both images show both filled and half-filled micro-channels.

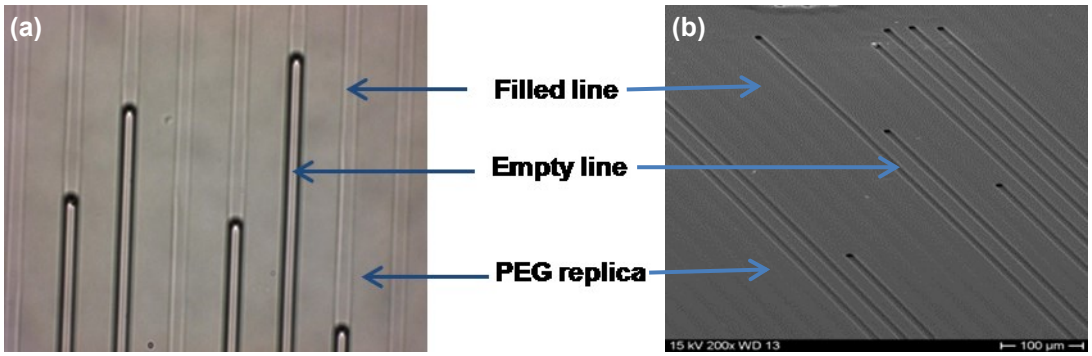

Figure 52: Micro-pattern of PEG – Au NPs composite (a) optical microscope image. (b) Scanning electron microscope image

A solution of fluorescent dye (structure and preparation will be described in chapter 5) in acetone was mixed with PEG – Au NPs composite before insertion into

the micro-channels, then the micro-pattern was visualized using a confocal microscope, illustrated in Figure 53.

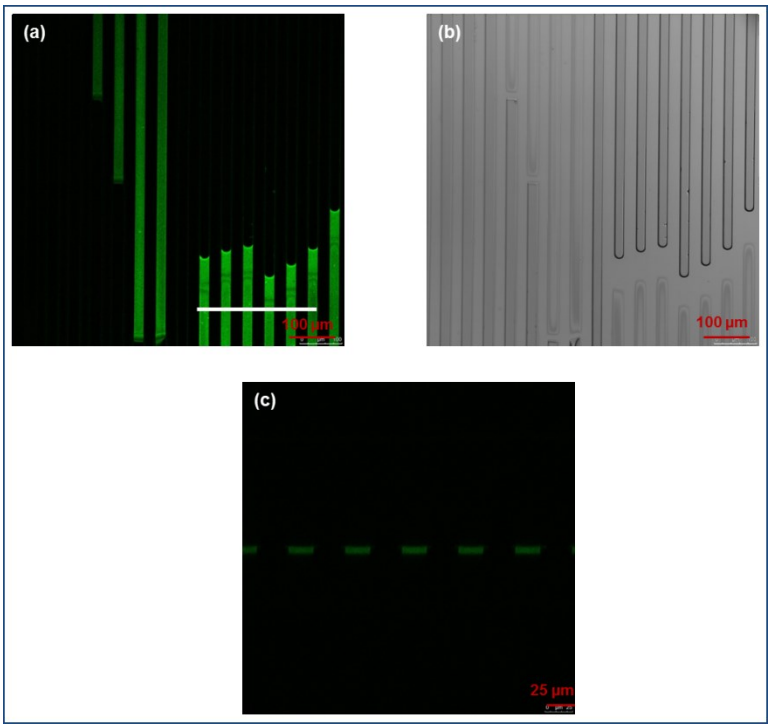

Figure 53: Confocal and the corresponding optical microscope image for PEG – Au NPs composite micro-pattern (a&b), and a cross section of the filled channels (c)

AFM characterization for Au NPs within the micro-pattern

Atomic force microscopy was employed to characterize Au NPs inside the micro-pattern of FIMIC samples. Figure 54a shows phase image for the micro-pattern substrate where two phases are visible. The first phase for PEG replica mold and the second one for PEG – Au NPs composite forming the filler.

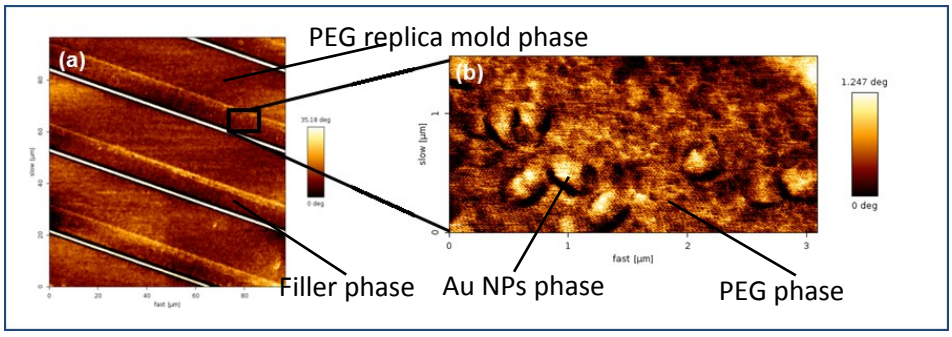

Figure 54*: Phase image of the micro-pattern of PEG – Au NPs composite (a) and Au NPs within the micro-pattern (b)*

A magnified image (Figure 54b) also shows two phases, the first belongs to PEG hydrogel as one component of the composite filler and a second phase to Au NPs as the second component of the composite material.

The surface characterization through topographical imaging and the corresponding cross section is shown in Figure 55, provides further proof of the existence of Au NPs within the micro-pattern. The cross section of the FIMIC sample shows a topographic difference of around 200 nm (Figure 55a), while a cross section of the magnified image within the micro-pattern (Figure 55b) exhibits a surface topography of around 3 nm, proving the existence of Au NPs (recall that surface topography for PEG hydrogel is within the range of 1 nm) (Figure 51b).

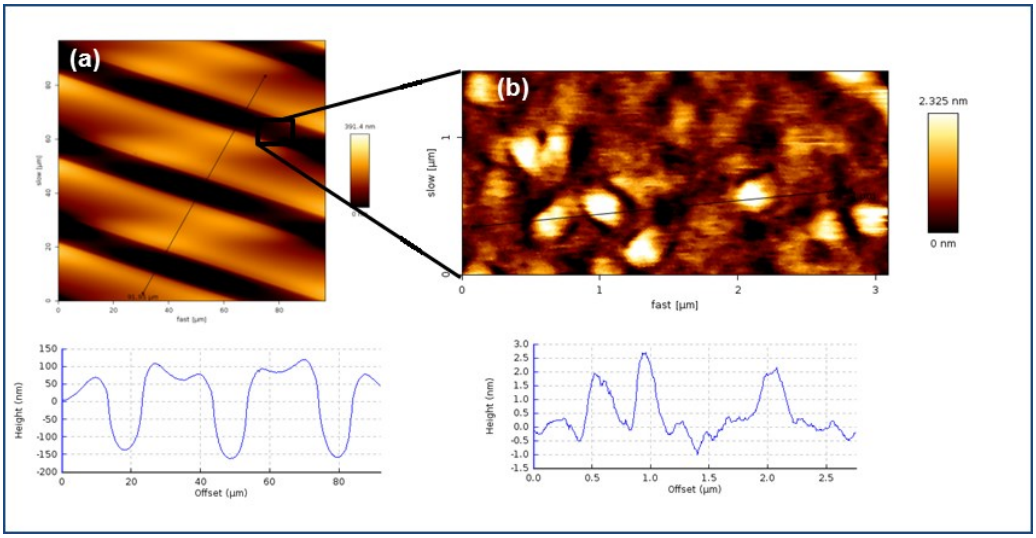

Figure 55: Height image of micro-pattern PEG – Au NPs composite and its corresponding height profile (a), Au NPs within the micro-pattern with the corresponding cross section (b)

As described before, the nanoparticles which were used in the FIMIC process have 20 nm size, as a consequence the (3 nm) value which is provided by the surface topography in the above image Figure 55b) for gold nanoparticles implies that the nanoparticles are partially buried in the hydrogel matrix.

Figure 56 shows an adhesion map of the micro-pattern where a pattern of elasticity could be seen through the existence of two kinds of colors. There are both lighter areas, where PEG mold is, and darker ones, where the micro-pattern of composite is. The ˝color code˝ in these kinds of images is used to indicate the strength of interaction between AFM tip and the material; lighter color means a stronger interaction between the tip and the surface (i,e stiffer material) and darker color indicates a weaker interaction (i,e softer material). This is based on the fact that

regions where Au NPs are show unexpectedly softer material, as indicated by Figure 56. This might be attributed to the presence of Au NPs in the PEG matrix interfere crosslinking reaction of PEG polymer chains upon UV-curing, which results in a lower crosslinking density of PEG polymer and hence generation of softer material.

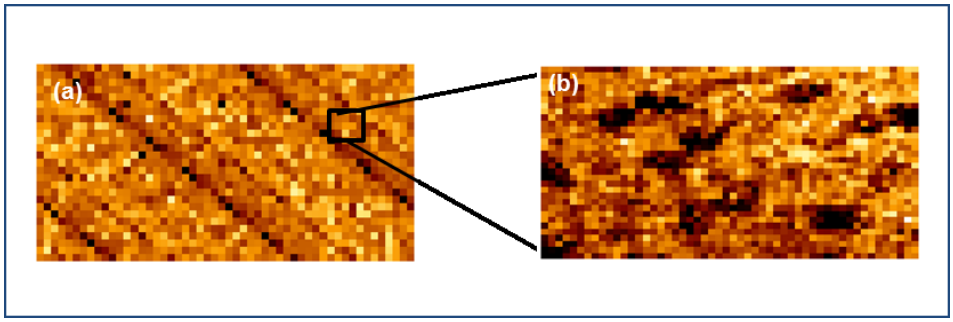

Figure 56: Adhesion map of the micro-pattern (a) and Au NPs within the pattern (b)

Slope map results from the slope of (f/d) curves, as indicated by Figure 57, and shows a lower elasticity value for PEG Au NPs composite, (i,e lower Young's Modulus). This is indicated by the darker color of the micro-pattern compared to the lighter color for the mold composed of PEG, representing higher Young's Modulus (i,e stiffer material). Areas where Au NPs are, show the same phenomenon; they have a softer area with lower elasticity value for Au NPs composites (Figure 57).

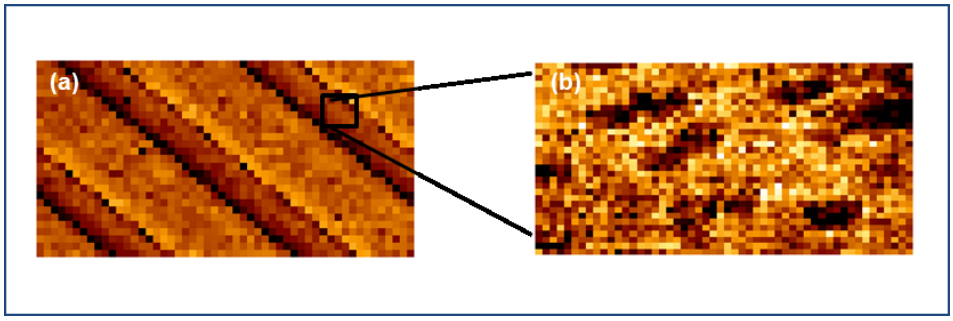

Figure 57: Slope map of the micro-pattern (a) and Au NPs within the pattern (b)

Moreover, data obtained from rheology measurements reveal that 10% Au loading composite material has a bulk elasticity of 0.87 ± 0.09 MPa, which is a lower value than the figure 16.9 ± 3.67 MPa of pure PEG575 obtained under the same conditions (1% photoinitiator, 0% cross linker). These results support the theory that the presence of Au NPs within the hydrogel decreases elasticity. In another words, the presence of Au NPs within the composite material increases its softness compared to pure PEG575.

The results obtained from both force maps and rheology support the same observation: there is lower elasticity and softer material in the areas involving Au NPs, compared to pure PEG575, which might be attributed to the interference of Au NPs in the crosslinking reaction between the polymer chains.

In summary, AFM was used to characterize the gold nanoparticles within the micro-pattern. While phase image shows two phases in the zoom in image of the micro-pattern belong to Au NPs and PEG, the surface topography gives 3 nm value as a surface roughness which is a higher value than the roughness of the PEG surface and lower than the actual size of Au NPs utilized in the process. This indicates that the NPs are partially entrapped in the hydrogel matrix.

Force maps as well as rheology results reveal that, areas containing Au NPs exhibit unexpectedly softer material accompanied with lower elasticity i.e. lower Young's Modulus value than PEG hydrogel without Au NPs. These results could be attributed that the presence of Au NPs in the composite matrix retards the crosslinking reaction between PEG chains upon UV-curing which leads to a decrease in the crosslinking density. As the crosslinking density of the polymer decreases, consequence its elasticity value also decreases.

3.3.1 Limitations result from FIMIC strategy

Scum layer formation: A scum layer forms during the filling of the replica micro-channels when the filling of the prepolymer is not restricted to the micro-channels but also includes the residual area of the replica, creating a polymer layer underneath the replica.[19] Example of scum layer formation could be seen in Figure 58

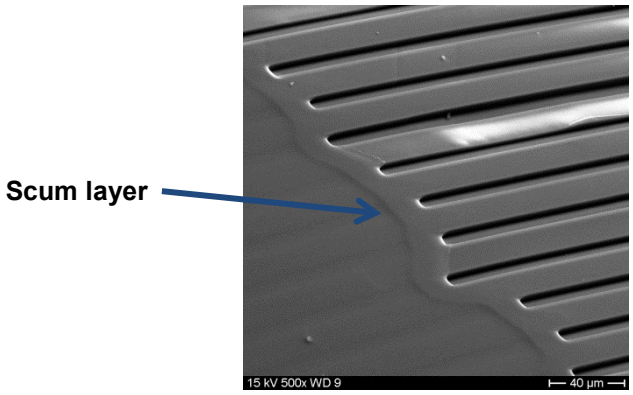

Figure 58: SEM image for scum layer formation in FIMIC substrate

Several factors can influence scum layer formation, such as unsealed contact between the PEG replica (the mold) and glass slide underneath. There are also a number of factors that can prevent good contact between the PEG mold and the glass, dust contamination on the glass for example. Furthermore, the presence of wider grooves in the replica mold to better seal the system. A large quantity of liquid prepolymer during the filling process of the micro-channels or unwanted contact with the replica edges during the filling process also assist scum layer formation.

Delamination problem: this problem results when one line or several lines are loosed from FIMIC substrate after it has been swelled in water. See Figure 59. This is an essential aspect in the application of FIMIC substrate in biofunctional molecules immobilization since this occurs primarily in liquid environments.

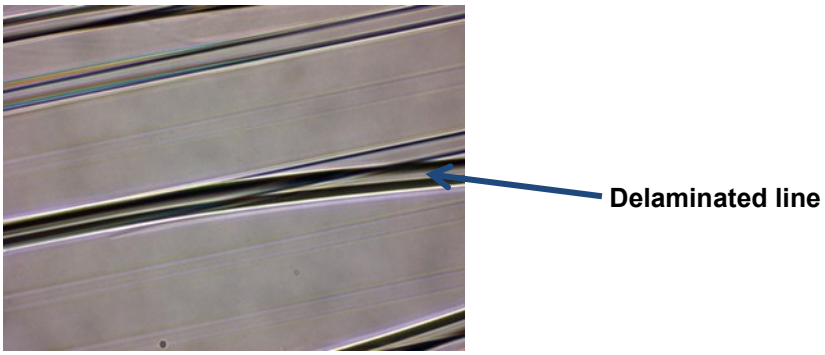

Figure 59: Optical microscope image for some delaminated lines in a FIMIC sample

Delamination usually takes place as a result of inconsistent degrees of swelling between the filler and the mold.[19] Since we are dealing with almost the same material (i,e PEG575) for the mold and the matrix of the composite material forming the filler, we must avoid delamination of both the filler and the mold by crosslinking the two upon UV curing. This couldn't be achieved if the replica itself were fully cured under UV before filling the micro-channels. We therefore tried to form the replica under a different curing time and to fill its micro-channels after. At the end, the FIMIC substrate was immersed in water for 24 hrs. An optical microscope was used to verify the delamination results. Different curing times for the PEG replica at a constant curing time for FIMIC substrate are illustrated in Table 1.

Table 1: Curing time for both PEG replica and FIMIC substrate

Curing time (PEG replica) (in minutes)	**Curing time (FIMIC) (in minutes)**	**Delamination**
5	30	No delamination
8	30	No delamination
10	30	No delamination
15	30	Delamination
20	30	Delamination

We found that if the PEG replica is cured for around 10 minutes or less, then the delamination problem can be avoided. The time is enough to have the replica micro-channels in good enough form that they could be used after that for the filling process.

Limited patterned surface area: it is usually difficult to achieve patterning over a large area; patterned areas normally cover just several micrometers. This problem might

be partially avoided if more than one substrate were used at a time or if the patterning proceeded over several positions in the same replica.

Limited PEG loading capacity for Au NPs: since the used gold nanoparticles in composite formation are citrate-capped gold nanoparticles, i,e negatively charged, the loading capacity of the PEG prepolymer is limited to a narrow range of nanoparticle concentration. Stability of citrate-capped gold nanoparticles in PEG precursor solution was verified using TEM. Measurements for 10% and 20% of Au NPs by weight in PEG precursor solution revealed that Au NPs was homogeneously distributed in PEG precursor solution, indicating that PEG precursor is able to stabilize citrate-capped Au NPs at this concentration level. Results are shown in Figure 60 (a & b).

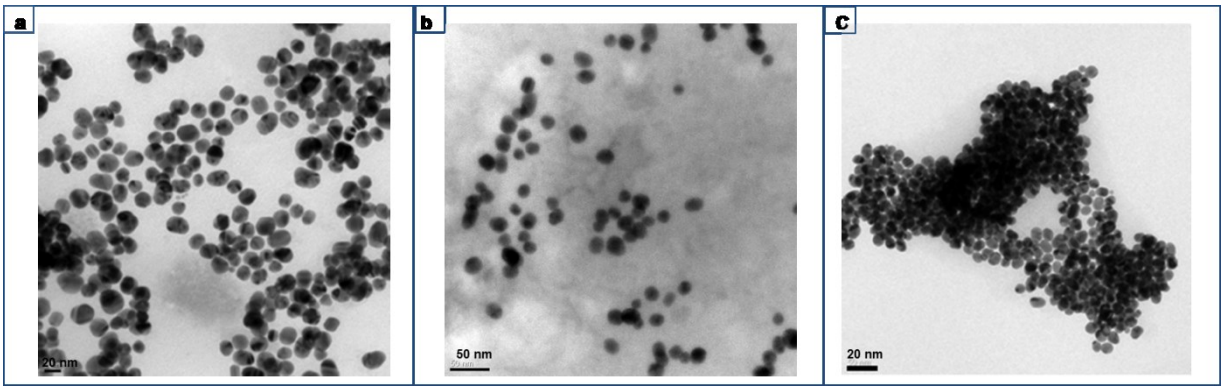

Figure 60: TEM images of 10% (a) and 20% (b) of citrate-capped Au NPs in PEG precursor solution, while (C) by increasing Au NPs loading for four times

On the other hand, by increasing gold nanoparticle loading in PEG precursor solution for four times, we caused unwanted agglomeration of the particles, shown in Figure 60 (c).

In summary, FIMIC method was used to create three-dimensional (3D) micro- and nano-patterns of composite material composed of PEG and Au NPs. This use could find an application under our scope of biomolecules' immobilization.

We were able to solve, either partially or completely, many of the inherent difficulties associated with FIMIC fabrication and applications. However, some issues are still open to further research, such as increasing the loading capacity of the polymer, an important requirement in terms of biomolecules immobilization that could be achieved by using either the existing NPs as seeds for further growth in situ, or by using another kind of nanoparticle with a capping agent other than our negatively charged citrate capped NPs, which achieved better stabilization by PEG precursor solution.

4. Conclusion

Novel surface functionalization methods were developed by creating specific sites available for biofunctional molecules immobilization on a protein-repellent background through two approaches. The first strategy for the successful transference of spherical nanoparticles was the one obtained by BCM method, utilizing simple, straightforward protocol without any linker assistance through hydrogel swelling in water.

The second approach involved is the transference of different morphologies of the nanostructures from the surface of a hard inorganic silicon substrate to the surface of a soft polymeric polyethylene glycol hydrogel, mediated by a linker molecule. This strategy was demonstrated for a wide range of nanostructures, from spherical nanoparticles to more complex nanostructures such as 2D, 3D and hollow urchin-like nanoparticles. Furthermore, the method was applied to other metal compositions (Ag and AgAu core-shell NPs) sharing their specific affinity toward certain functional moieties (amine and thiol) with gold nanoparticles.

Novel micro-pattern of PEG – Au NPs composite was achieved by employing our recently developed soft lithographic method Fill Molding In Capillaries (**FIMIC**) to generate a 3D platform that can be applied to biomolecules immobilization.

5. Bibliography

(1) Hanawa, T. *J. Periodontal Implant Sci.* **2011**, *41*, 263–272.

(2) Aydin, D.; Louban, I.; Perschmann, N.; Blümmel, J.; Lohmüller, T.; Cavalcanti-Adam, E. A.; Haas, T. L.; Walczak, H.; Kessler, H.; Fiammengo, R.; Spatz, J. P. *Langmuir* **2010**, *26*, 15472–80.

(3) Ballav, N.; Terfort, A.; Zharnikov, M. *Langmuir* **2009**, *25*, 9189–9196.

(4) Lee, Z.; Lee, K.; Hong, J.; Kim, J.; Cheong, C.; Choi, I. S. *Bull. Korean Chem. Soc.* **2005**, *26*, 1166–1167.

(5) Revzin, A.; Rajagopalan, P.; Tilles, A.; Berthiaume, F.; Yarmush, M.; Toner, M. *Langmuir* **2004**, *20*, 2999–3005.

(6) Khademhosseini, A.; Yeh, J.; Jon, S.; Eng, G.; Suh, K. Y.; Burdick, J. A.; Langer, R. *Lab Chip* **2004**, *4*, 425–430.

(7) Xia, Y.; Whitesides, G. M. *Angew. Chemie Int. Ed.* **1998**, *37*, 550–575.

(8) Ma, H.; Hyun, J.; Stiller, P.; Chilkoti, a. *Adv. Mater.* **2004**, *16*, 338–341.

(9) Liu, P.; Sun, J.; Huang, J.; Peng, R.; Tang, J.; Ding, J. *Nanoscale* **2010**, *2*, 122–7.

(10) Bilodeau, G. *J. Appl. Mechancis* **1992**, *59*, 519–523.

(11) Flory, P. J. *Principles of Polymer Chemistry*; University Press: Cornell, 1953.

(12) Chen, J.; Mela, P.; Möller, M.; Lensen, M. C. *ACS Nano* **2009**, *3*, 1451–1456.

(13) Chen, J.; Arafeh, M.; Guiet, A.; Felkel, D.; Loebus, A.; Kelleher, S. M.; Fischer, A.; Lensen, M. C. *J. Mater. Chem. C* **2013**, *1*, 7709-7715.

(14) Yuan, J.; Oliver, R.; Li, J.; Lee, J.; Aguilar, M.; Wu, Y. *Biosens. Bioelectron.* **2007**, *23*, 144–148.

(15) Graeter, S. V; Huang, J.; Perschmann, N.; López-García, M.; Kessler, H.; Ding, J.; Spatz, J. P. *Nano Lett.* **2007**, *7*, 1413–1418.

(16) Xia, Y.; Kim, E.; Whitesides, G. M. *Chem. Mater.* **1996**, *8*, 1558–1567.

(17) Kelleher, S.; Jongerius, A.; Loebus, A.; Strehmel, C.; Zhang, Z.; Lensen, M. C. *Adv. Eng. Mater.* **2012**, *14*, 56–66.

(18) Diez, M.; Schulte, V. a.; Stefanoni, F.; Natale, C. F.; Mollica, F.; Cesa, C. M.; Chen, J.; Möller, M.; Netti, P. a.; Ventre, M.; Lensen, M. C. *Adv. Eng. Mater.* **2011**, *13*, B395–B404.

(19) Löbus, A. Patterning Strategies of Poly (ethylene glycol) Based Hydroxyapatite Composites for Biomedical Applications, **2013**, p. 48.

Chapter 5

Construction of a fluorescein-based model system to be immobilized onto gold nanoparticle patterned substrates

As we intend to immobilize green fluorescent protein (GFP), as a model for biofunctional molecules, onto our patterned Au NPs arrays, it is crucial to adjust the parameters involved in the immobilization process. Such parameters include fluorescence quenching as a probable consequence of direct immobilization of fluorophore onto Au NPs. The aim of this chapter is therefore to construct a fluorescein-based model system to be immobilized onto our patterned Au NPs, accompanied by a well-designed linker molecule with an adjustable chain length in order to diminish the probability of fluorescence quenching.

Zhenfang Zhang, Axel Loebus, Gonzalo de Vicente, **Manar Arafeh** and Marga C. Lensen, In situ Formation of Novel Poly(ethyleneglycol)-based Hydrogels via Amine-Michael type Addition with Tunable Mechanics and Chemical Functionality *(submitted to chemistry of materials)*

Manar Arafeh, Marga C. Lensen, Synthesis and Characterization of Fluorescein-based Derivatives *(in preparation)*

1. Introduction

1.1 Fluorescence background: definition, Stokes shift and Jablonski diagram.

Fluorescence is a kind of luminescence that involves emission of light as a consequence of the absorption of electromagnetic radiation, where the emitted radiation has a longer wavelength (lower energy) than the absorbed radiation. “This shift towards longer wavelengths, or lower energies” called *Stokes shift,* is the difference between the maximum of the first absorption band and the maximum of the fluorescence spectrum. When the emitted radiation has the same wavelength as the absorbed radiation, this phenomenon is called resonance fluorescence.[1,2]

The best description for the different relaxation mechanisms or paths taken by an excited molecule back to the ground state is given by the *Jablonski diagram,* illustrated in Figure 61. The diagram depicts both radiationless and radiative routes, including fluorescence.

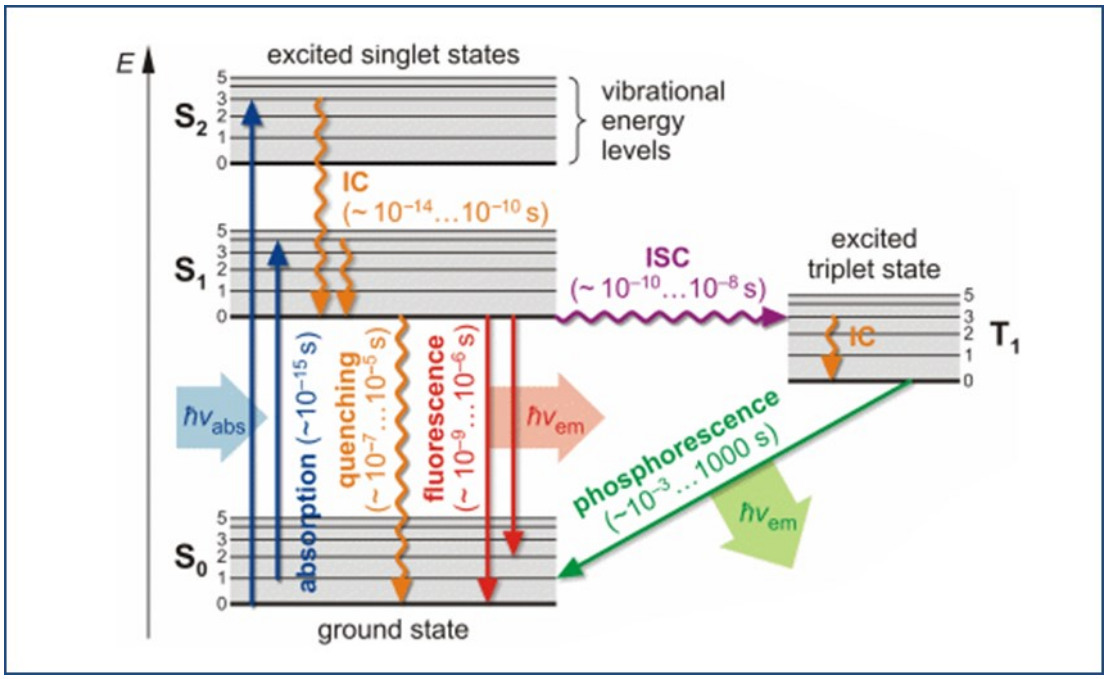

Figure 61: Jablonski energy diagram illustrating relaxation mechanisms of an excited fluorophore to return to the ground state(3)

As shown above, fluorescence results following transition from the lowest vibrational level of the first electronic singlet excited state back to the electronic ground state, or one of its vibrational levels.

1.2 Fluorescence quenching

Fluorescence quenching implies a decrease in the intensity of fluorescence emission due to molecules' relaxation through non-radiative pathways. A number of processes lead to fluorescence quenching, some of them happen during the excited state lifetime, such as collisional quenching (dynamic quenching), and others while the molecule is still in the ground state, such as complex formation between fluorophore and the quencher (static quenching).

Collisional quenching is a consequence of direct contact between fluorophore and the quencher (e.g. oxygen, amine or acrylamide) in the excited state, and enhances the probability that non-radiative mechanisms will be employed to return to the ground state. As a consequence of collisional quenching, both fluorescence quantum yield and lifetime are reduced.

Static quenching occurs due to non-fluorescent complex formation between fluorophore and the quencher in the ground state. In contrast to collisional quenching, fluorescence lifetime is not affected in static quenching.

In general, there are three mechanisms of fluorophore quenching: heavy atom effect or intersystem crossing, electron exchange and photoinduced electron transfer.

1.2.1 Intersystem crossing (heavy atom effect)

In heavy atom effect, fluorescence quenching can take place, where heavy atoms such as halogens act as fluorophores' quenchers.

Fluorescence quenching resulting from heavy atom effect happens as a consequence of spin-orbit coupling between the fluorophore and the quencher, which enhances intersystem crossing to the triplet state.[4] Since the lifetime of the triplet state is relatively long, the likelihood it will be quenched by the same quencher as the ground state is high and it is even possible that it may go back to the ground state by means of non-radiative mechanisms.[5]

1.2.2 Electron-exchange quenching

This mechanism involves an electron transfer process between donor and acceptor molecules, in which an electron transfers from the lowest unoccupied molecular orbital (LUMO) in the donor species to the highest-occupied molecular orbital

(HOMO) in the acceptor, then back again to the donor. Since the acceptor returns the electron from its HOMO orbital, it is left in an excited state.

1.2.3 Photoinduced electron transfer (PET)

PET process takes place through a complex formation between the electron donor and the electron acceptor, in which electron transfer can return to the ground state without photon emission[6].

1.2.4 Resonance energy transfer (RET)

Photon absorption excites one of the two electrons occupying the (HOMO) orbital up to the (LUMO) orbital. RET process occurs when the excited electron returns to the ground state where its energy then transfers to the acceptor, causing excitation of one of its electrons to a higher state. Since this process involves energy transfer from the donor to the acceptor, the fluorescence intensity of the donor species decreases.

1.3 Quenching of fluorophore near gold surface

Fluorophores are highly influenced by the surface plasmon field generated from metal nanoparticles (Au and Ag NPs) upon their induction by a photonic energy,[7] which affects both fluorophore quantum efficiency and lifetime.[8,9] The nature of fluorescence response to this field (either fluorescence enhancement or quenching) depends on a number of parameters including metal type, size, shape and distance between fluorophore and the metal surface.[10] Furthermore, it was also confirmed that fluorophore immobilized onto bulk gold shows stronger quenching behavior compared with that immobilized onto gold nanoparticles.[11]

Fluorophore exhibits a strong quenching effect near gold surface, where the quenching mechanism is thought to proceed through resonance energy transfer (RET) to the absorption band of gold (see above).[2]

1.4 Diminishing effect of linker molecule on quenching

A number of studies show the distance-dependent fluorescence quenching of fluorophore near the surface of gold nanoparticles.[8,12,13] For example, the Liu Group reported that distance between small dye (fluorophore) nanoparticles will enhance fluorescence quenching.[8] Additionally, the Tinnefeld Group observed that, with fluorophore – metal nanoparticles with a distance smaller than 15 nm, a significant

quenching in fluorescence intensity occurs as well as the reduction of fluorescence lifetime.[12]

It is therefore crucial to employ a linker molecule with a well-adjusted chain length between gold nanoparticles and the fluorophore in order to diminish the quenching effect of the gold nanoparticles – fluorophore interaction.

2. Experimental

NMR measurements have been performed using Bruker 400 MHz machine and $CDCl_3$ as a deuterated solvent.

*Preparation of 11-mercaptoundecanoylchloride from 11-mercaptoundecanoic acid (**2**)*

Thionylchloride (0.07 g, 5.88×10^{-4} mol) was added to a stirred solution of 11-mercaptoundecanoic acid (0.126 g, 5.76×10^{-4} mol) in 10 ml dichloromethane (DCM) under nitrogen atmosphere. The reaction was kept under reflux overnight. As soon as the reaction is over, the excess amount of thionyl chloride and DCM were evaporated under vacuum yielding 0.126 g (90%) of the chloride product as brown oil. Ms (ESI) (m/z): $[M^+Na^+H_2O2H^+]$ 279.13 ^{1}H-NMR: δ(ppm): 2.86 (t, 2H, J = 0.019 Hz), 2.65 (t, 1H, J = 0.019 Hz), 1.66 (4H, m), 1.26 (13H, m). ^{13}C NMR: δ(ppm): 173.82, 47.12, 39.12, 38.82, 29.37, 29.25, 29.11, 28.79, 28.48, 28.41, 25.05

*Preparation of N-fluoresceinyl-11-mercaptoundecanyramide (**4**)*

A 10 ml solution of (**2**) (0.126 g, 5.3×10^{-4} mol) in acetone was added dropwise over a period of 15 minutes to a stirred solution of (0.54 g, 1.55×10^{-3} mol) 6-aminofluorescein (**3**) dissolved in 20 ml acetone at 0 °C. The reaction was kept in the ice bath for two hours before the reaction mixture was filtrated and the residue under vacuum evaporated. The crude product was purified by recrystallization from ethanol to yield 0.68 g (80%) of the purified product as an orange solid. Ms (ESI) (m/z): $[M^+]$ 547.20. ^{1}H NMR: δ(ppm): 7.90-7.88 (d, 1H, J = 0.021 Hz), 7.74-7.72 (d, 1H, J = 0.022 Hz), 7.56-7.55 (s, 1H), 6.66-6.65 (d, 2H, J = 0.006 Hz), 6.61 (s, 1H), 6.59 (s,1H), 6.53-6.52 (d, 1H, J = 0.006 Hz), 6.51-6.50 (d, 1H, J = 0.006 Hz) 2.84-2.80 (t, 1H, J = 0.018 Hz), 2.63-2.60 (t, 1H, J = 0.018 Hz), 2.28-2.25 (t, 2H, J = 0.018 Hz), 1.63-1.45 (m, 4H), 1.26-1.17 ppm rest of the protons. ^{13}C NMR: δ(ppm): 172.36, 168.91, 168.34, 159.89, 159.61, 151.97, 151.79, 145.75, 129.18, 129.12, 126.14, 125.79, 120.41, 120.14, 112,98, 112.78, 110.72, 100.88, 102.28, 102.15, 38.18, 37.92, 36.51, 30.77, 28.90, 28.87, 28.82, 28.79, 28.64, 28.56, 28.52, 28.26, 27.74, 27.70. 24.81. IR peak assignments are shown in Table 2 in the results and discussion.

Silicon patterned gold nanoparticles substrates

Silicon patterned gold nanoparticle substrates were prepared by employing the block copolymer micelle (BCM) nanolithography method as described in chapter 3. The nanoparticles had an interparticle distance of around 70 nm.

*Conjugation of fluorescein-based linker molecule (**4**) to Au NPs patterned on silicon substrate*

Si Au-NPs substrate was washed with water, isopropanol and acetone and finally dried under a stream of nitrogen before being incubated overnight in a 3 ml of 0.01 M solution of (**4**) in acetone. The substrate was then washed through immersion in acetone solvent for 10-20 minutes to remove unbound dye molecules from the surface, then characterized by fluorescence microscope.

3. Results and discussion

3.1 Synthesis of fluorescein based linker molecule

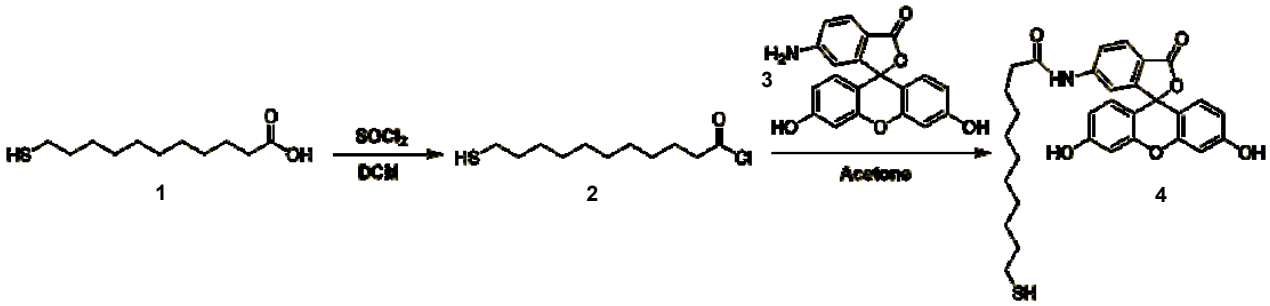

Figure 62: Scheme illustrating synthetic route of fluorescein-based linker molecule

The initial step of the synthesis protocol, illustrated in Figure 62, proceeded with a chlorination reaction of mercaptoundecanoic acid (**1**) to the corresponding chloride product (**2**) using thionyl chloride as a chlorinating agent. The formed product was used without any further purification in reaction with aminofluorescein (**3**) in order to produce our fluorescein-based linker molecule.

3.1.1 Synthesis and characterization of 11-mercaptoundecanoylchloride (2)

It is widely known that carboxylic compounds (**1**) react with thionyl chloride to produce the corresponding acid chloride (**2**). The reaction proceeds at room temperature and under nitrogen atmosphere to avoid humidity, since trace amount of water can react with thionyl chloride resulting in HCl and SO_2 formation, according to equation 1 or with the acid chloride product returning to the original carboxylic acid, as illustrated in Figure 63. Furthermore, water can react with the intermediate compound and interfere with acid chloride formation, as indicated in Figure 64.

$$SOCl_2 + H_2O \longrightarrow 2HCl + SO_2 \qquad \textbf{(1)}$$

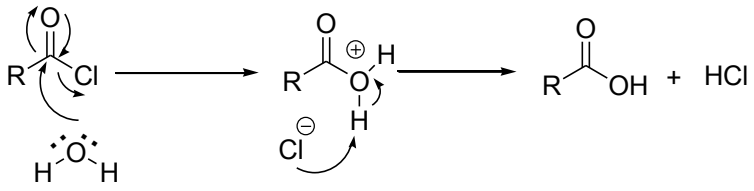

Figure 63: General scheme for the reaction between acid chloride and water

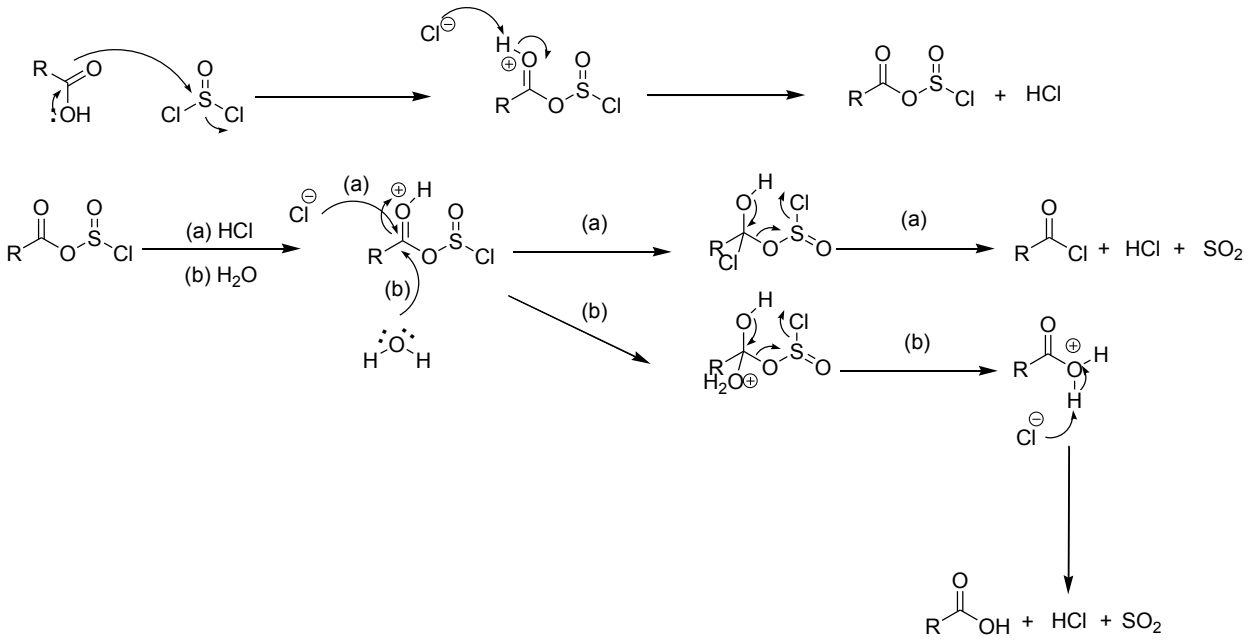

Figure 64: General scheme illustrating acid chloride formation (path a), in the case of water interfering with the reaction (path b) (reprinted from ref [14])

The title compound can be isolated from the reaction mixture by evaporating the solvent and the volatile byproducts. Characterization was performed using mass spectrometry and NMR.

The mass spectrum of the chlorinated compound (**2**) shows the correct molecular ion as expected from its molecular formula. The molecular ion peak shows the major fragment in the spectrum, indicated by Figure 65, where the molecular weight of the product is 236.1 amu and the molecular ion peak in the spectrum is 279.13, corresponding to (Mwt of the product + Na^+ + H_2O + $2H^+$).

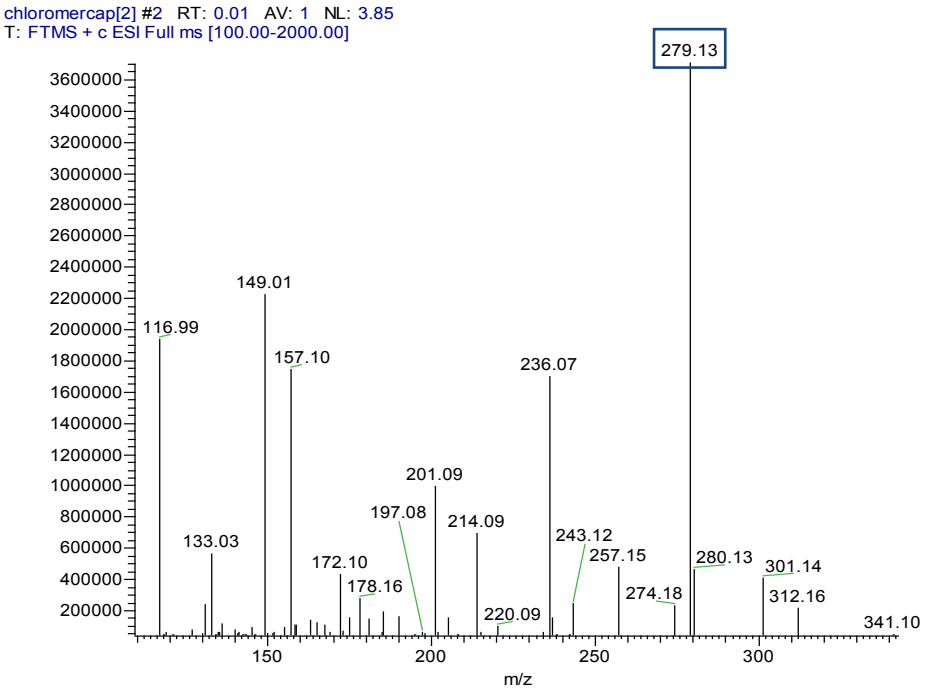

Figure 65: Mass spectrum of 11-mercaptoundecanoylchloride

The ^{1}H NMR spectrum of the title compound is in agreement with the assigned structure. The spectrum shows two triplets at δ 2.9 ppm and δ 2.6 ppm assigned to H-1 protons and H-4 protons, respectively. The chemical shift for H-2 and H3 protons is around 1.7 ppm, where they show multiplet splitting. The representative ^{1}H NMR spectrum for the product is shown in Figure 66.

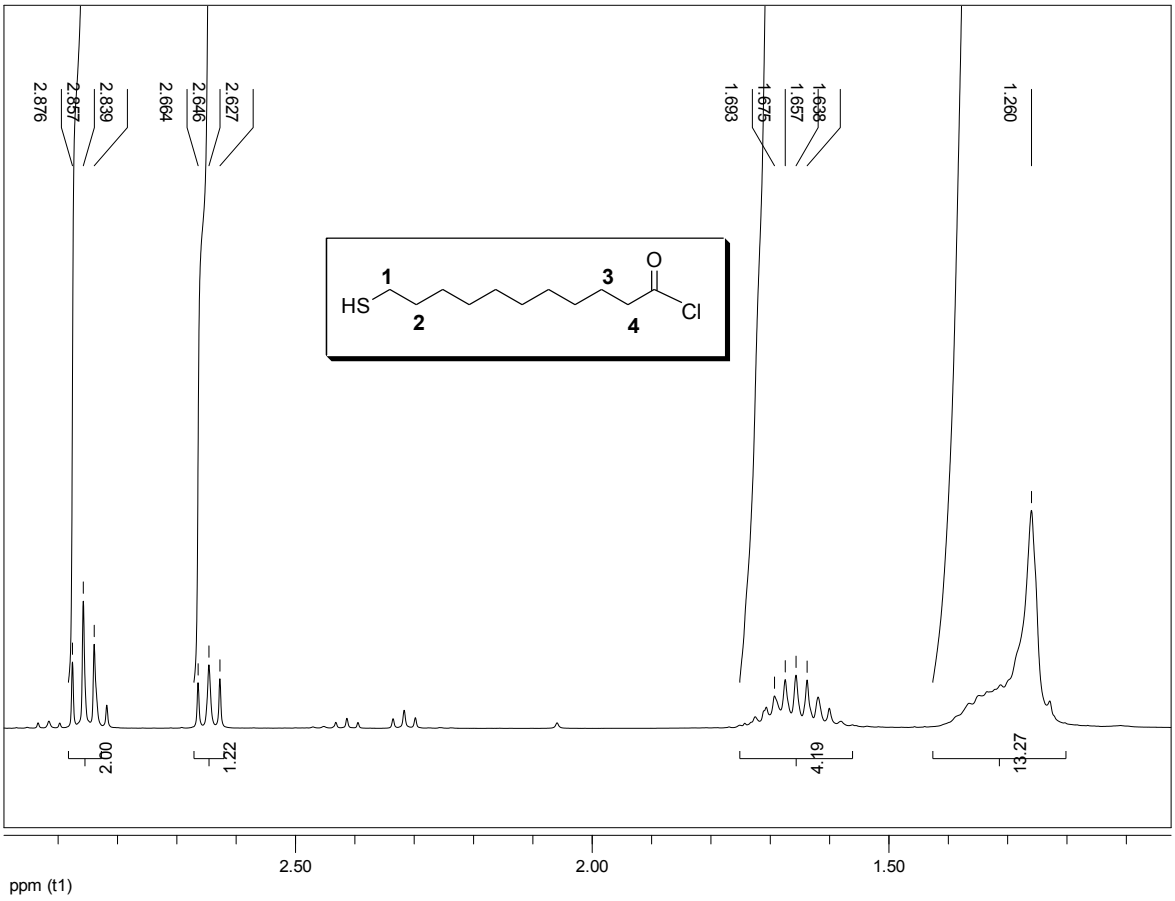

Figure 66: ^{1}H NMR spectrum of11-mercaptoundecanoylchloride

^{13}C NMR supports the evidence for the right constitution of the compound through the observable chemical shift of the carbonyl carbon upon the chlorination reaction, in comparison to the corresponding carboxylic acid as a starting material. Carbonyl carbon resonates at 180.3 in the carboxylic acid, then shifts to 173.8 upon acid chloride formation, as illustrated in Figure 67 and Figure 68 respectively.

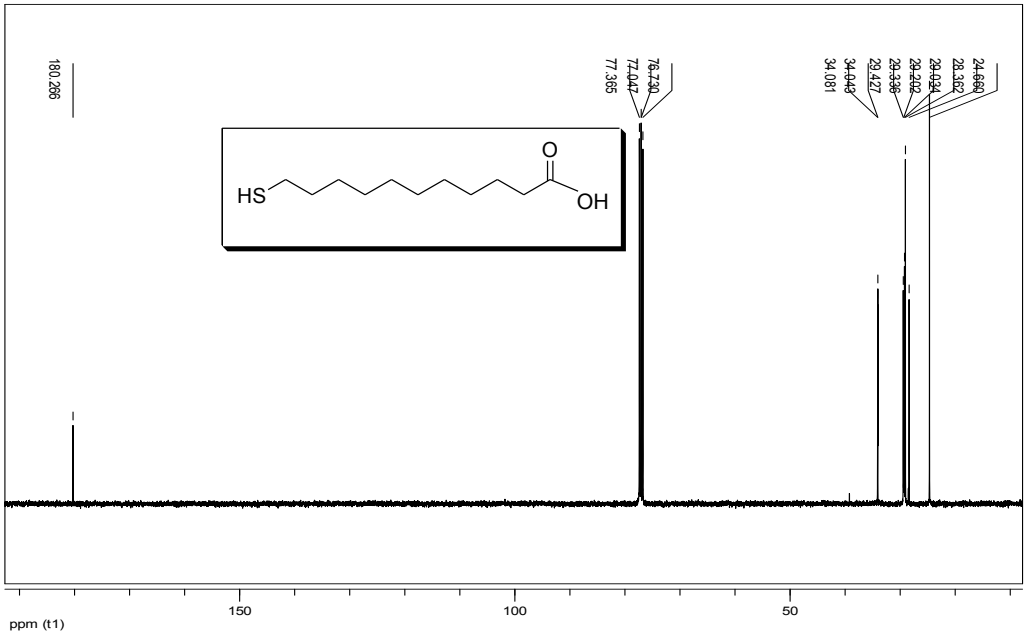

Figure 67: ^{13}C NMR spectrum for 11-mercaptoundecanooic acid

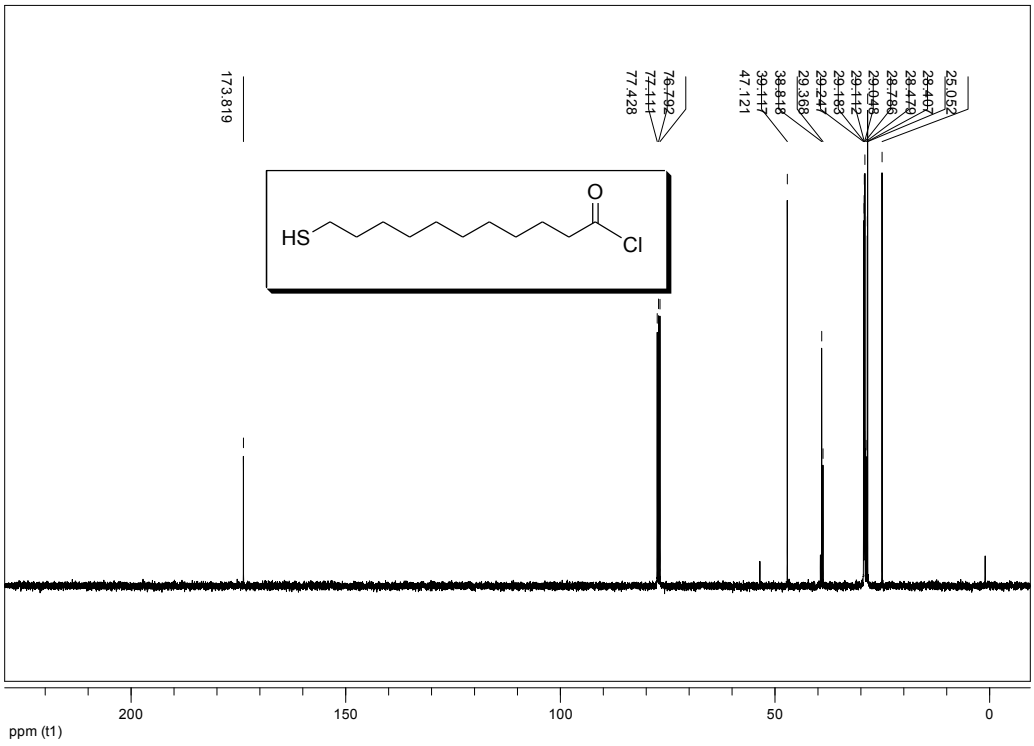

Figure 68: ^{13}C NMR spectrum of 11-mercaptoundecanoylchloride

3.1.2 Synthesis and characterization of N-fluoresceinyl-11-mercaptoundecanyramide (4)

The acid chloride (**2**) prepared in the previous step was allowed to react with aminofluorescein (**3**) through a nucleophilic addition elimination reaction in order to generate the corresponding amide product, as illustrated in the general scheme in Figure 69.

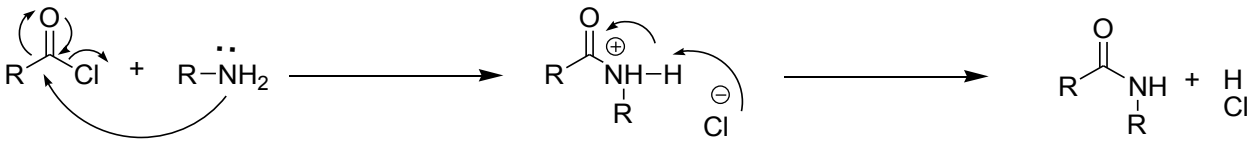

Figure 69: General scheme for the reaction between acid chloride and amine to generate the corresponding amide

The reaction was performed in the dark as well as in an oxygen-free atmosphere to avoid fluorescence quenching, which can result from light absorption or the presence of molecular oxygen in the reaction.

The title compound was recrystallized from ethanol and characterized using mass spectrometry, NMR and IR.

The mass spectrum of the product (**4**) shows the correct molecular ion peak as predicted from its molecular formula, where the molecular weight of the product is 547.20 amu, exactly matching the molecular ion peak in the spectrum. Representative mass spectrum is provided in Figure 70.

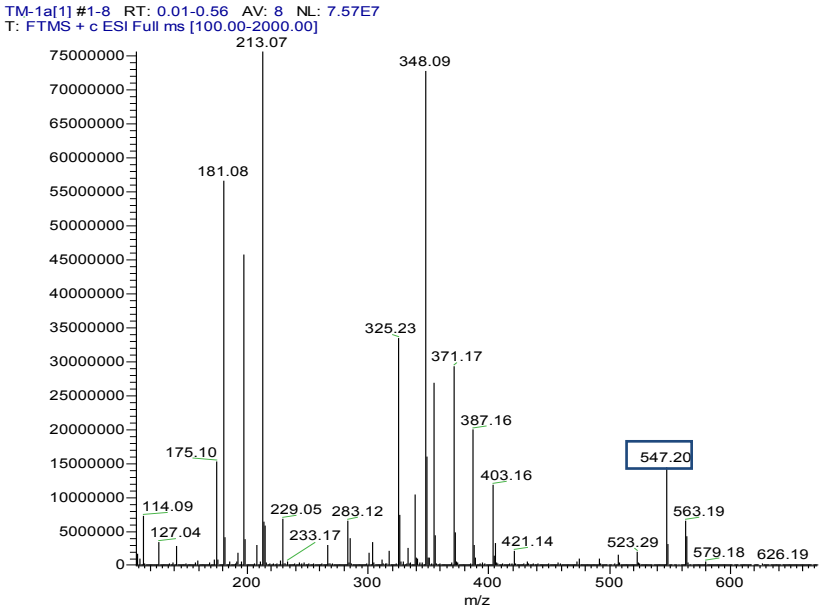

Figure 70: Mass spectrum of N-fluoresceinyl-11-mercaptoundecanyramide (4)

The ^{1}H NMR spectrum of the product is in agreement with the assigned structure. For clarity, the spectrum is split into two parts; aromatic protons appear in Figure 71 and aliphatic protons in Figure 72. The compound exhibits two doublets at δ7.89 ppm associated with a coupling constant of J = 0.021 Hz and at δ7.74 ppm with a coupling constant of J = 0.025 Hz assigned to the two protons H-b and H-a, respectively (Figure 71). Moreover, the spectrum shows a singlet peak resonate at δ7.59 ppm assigned to H-c proton.

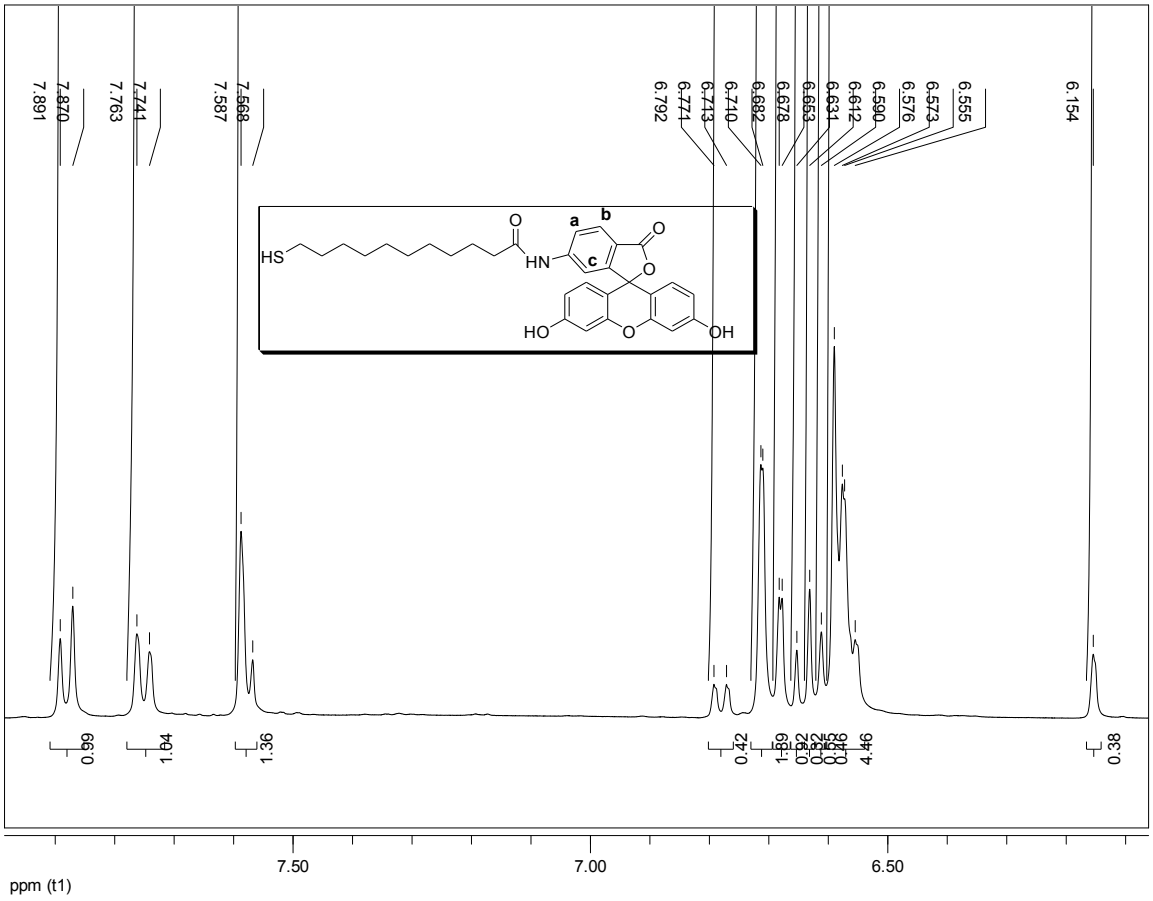

Figure 71: ^{1}H NMR spectrum for aromatic protons in N-fluoresceinyl-11-mercaptoundecanyramide (4)

In the aliphatic region, shown in Figure 72, the two H-1 protons seem to have different chemical environments from each other, because they resonate at different chemical shifts. One at δ 2.82 ppm and the other δ 2.60, where each exhibits triplet splitting of its NMR peak associated with a coupling constant of J = 0.018 Hz. A triplet peak resonating around δ2.26 ppm accompanied with a coupling constant of J = 0.018 Hz can be assigned with the two protons at H-10. Protons at H 2 and H-9 show multiplicity around δ1.63-1.45 ppm.

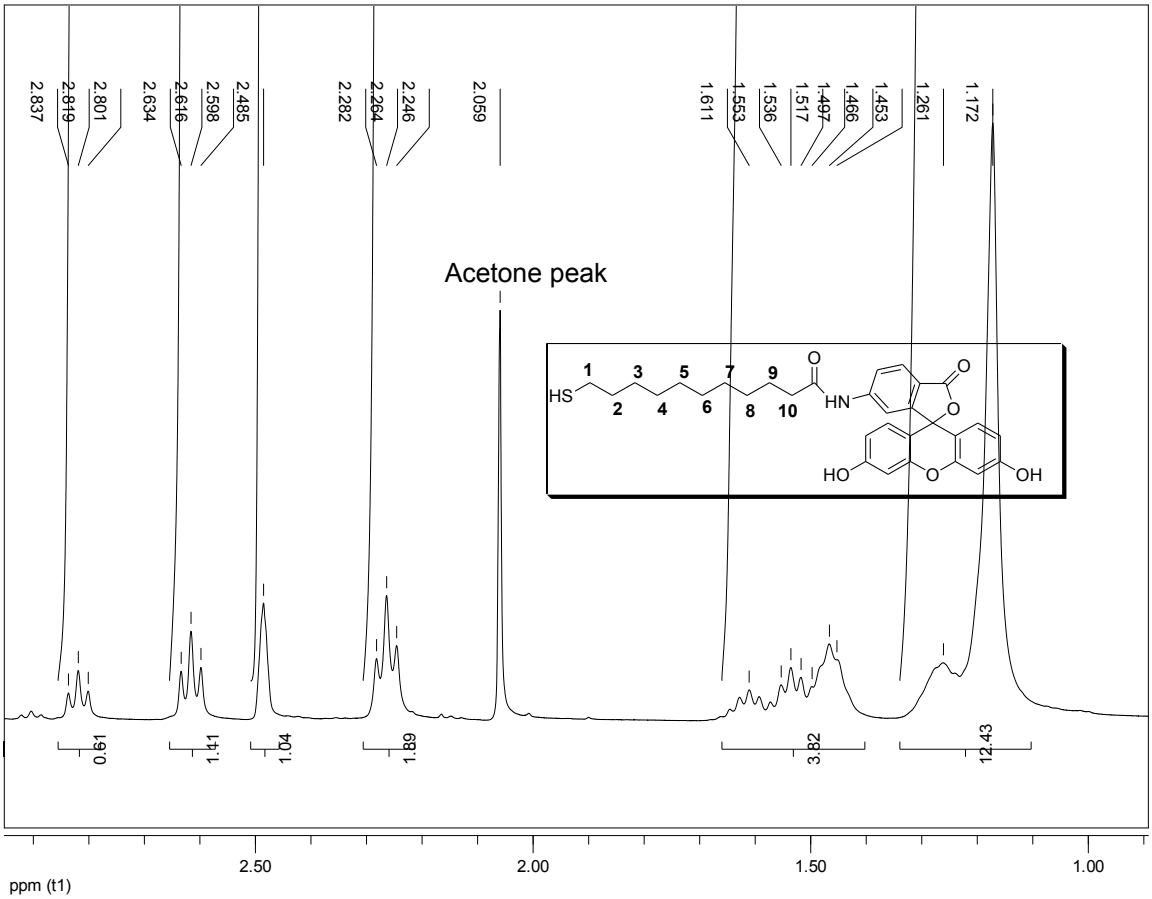

Figure 72: ^{1}H NMR spectrum for aliphatic protons in N-fluoresceinyl-11-mercaptoundecanyramide (4)

In ^{13}C NMR spectrum, shown in Figure 73, carbonyl carbon that forms the amide resonates around δ172.4 ppm, while (C-SH) resonates around δ 24.81 ppm. Carbonyl carbon forming cyclic ester resonates around δ168.91 ppm and carbon belongs to C-NH around δ 168.34 ppm.

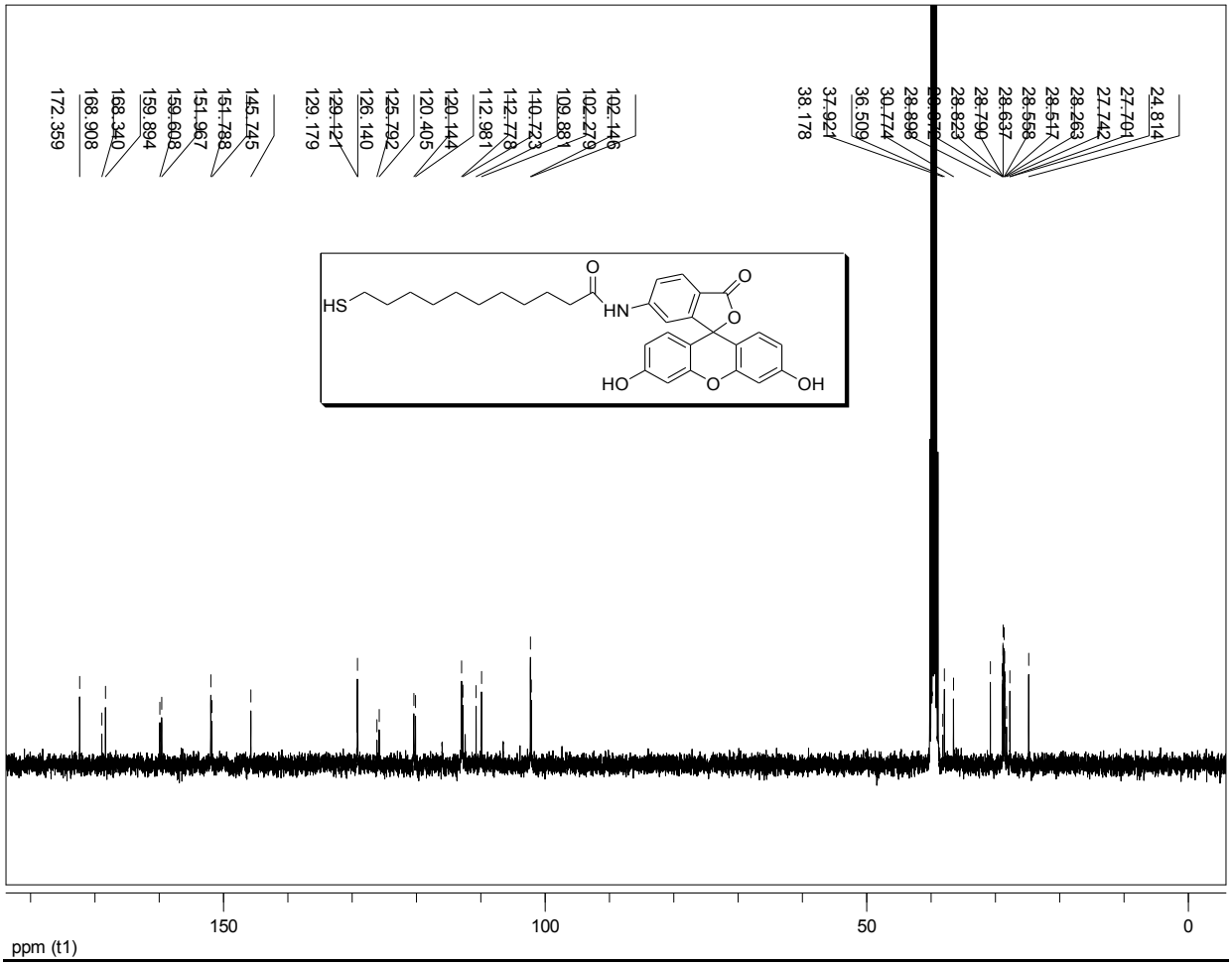

Figure 73: ^{13}C NMR spectrum of N-fluoresceinyl-11-mercaptoundecanyramide (4)

IR measurement was also performed, as indicated by Figure 74, and the absorption frequencies of the characteristic functional groups in the compound are shown in Table 2.

Table 2: Characteristic infrared absorption frequencies

Functional group	-O-H	-S-H	C=O (amide)	C=O (ester)	(cyclic ether)	C-O (OH attached to C)
Frequency (cm^{-1})	3473	2850	1677	1584	1232	1210

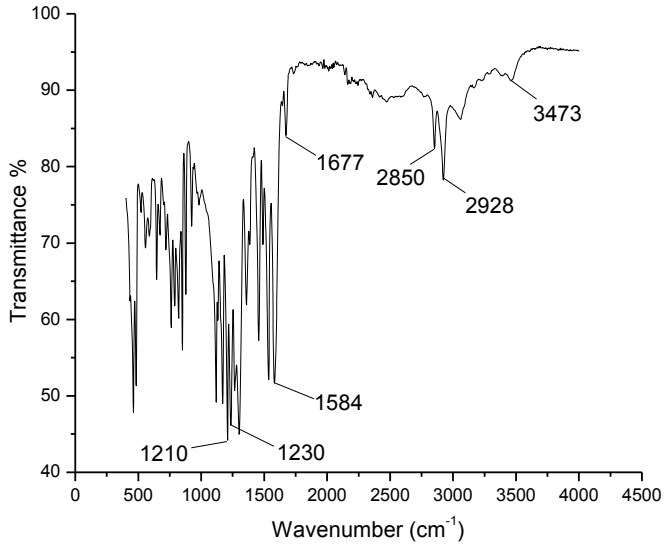

Figure 74: IR spectrum of N-fluoresceinyl-11-mercaptoundecanyramide (4)

3.2 Conjugation of N-fluoresceinyl-11-mercaptoundecanyramide (4) to Au NPs on silicon substrate

The target product was employed for specific conjugation to gold nanoparticles (Au NPs) on silicon through thiol moiety, in order to verify the quenching influence from Au NPs on the fluorophore. Figure 75 shows a laser scanned confocal microscope image of fluorescein conjugated to Au NPs through our synthesized spacer molecule.

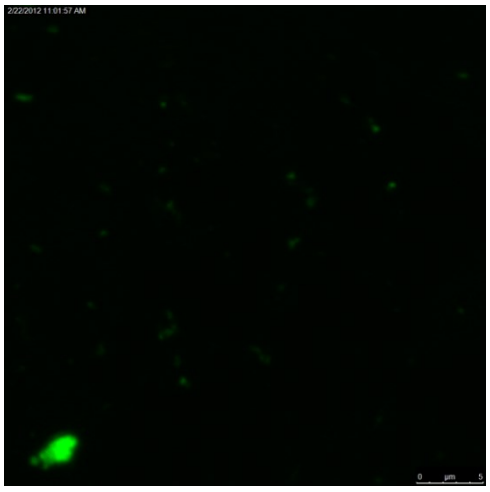

Figure 75: Confocal microscope image for fluorescein conjugated to Au NPs through spacer molecule

As shown in the above image, fluorescein displays selective immobilization onto gold nanoparticles on silicon guided by the high affinity of thiol functionality towards binding to the gold nanoparticles.

A fluorescein molecule was selected to act as an organic fluorophore in our system due to its high quantum yield (*Φ= 0.95).*[15] Quantum yield may be defined here as the ratio between the number of emitted photons to the number of absorbed photons. Moreover, Aminofluorescein possesses the complement functionality for easy functionalization to our spacer molecule.

The spacer molecule has the appropriate chain length to direct the fluorophore away from the surface of the nanoparticles, thereby decreasing fluorescence quenching.

Thiol functionality at the end of the linker molecule accounts for the specific conjugation of the molecule to the surface of the gold nanoparticles.

One limitation of this process is that the fluorescence pattern cannot be easily detected because the nanoparticles are separated by a distance of around 70 nm, less than the wavelength of the employed light (fluorescein has an excitation wavelength of around 495 nm). Nevertheless, our main interest in this work is the ability to detect fluorescence light originating from immobilized fluorescein molecules on the surface of gold nanoparticles, a goal which was reached.

4. Conclusion

A model system was designed, composed of a specific linker molecule with dual functionality. Specific binding to gold nanoparticles through thiol moiety from one side, and a complementary functionality to be conjugated to an organic fluorophore on the other side.

The synthetic route was proven by employing suitable characterization techniques, such as mass spectrometry, NMR and IR.

The chain length of the spacer molecule was carefully adjusted in order to diminish the fluorophore quenching that could result as a consequence of its conjugation to gold nanoparticles.

The confocal microscope was successfully implemented as an imaging technique in order to verify our ability to detect the emitted light from the fluorophore bound to gold nanoparticles. This successful implementation implies that the fluorescence originating from the fluorophore was not fully quenched.

The idea of employing a linker molecule with an appropriate chain length can be therefore successfully applied in order to immobilize biofunctional molecules with a fluorescent moiety in their structure (e.g. fluorescent proteins), without the risk of quenching from direct binding to the surface of gold nanoparticles.

5. Bibliography

(1) Skoog, D. A.; Holler, F. J.; Nieman, T. A. *Principles of Instrumental Analysis*; Vondeling, J.; Sherman, M.; Bortel, J.; Messina, F.; Pecuilis, V., Eds.; Fifth edit.; Thomson Learning Academic Resource Center, **1998**; p. 356.

(2) Valeur, B. *Molecular Fluorescence Principles and Applications*; WILEY-VCH Verlag GmbH: Weinheim, **2001**; Vol. 8, p. 54.

(3) Lo, J. R. Homo-FRET Imaging of CEACAM1 in Living Cells using Total Internal Reflection Fluorescence Polarization Microscopy, **2012**, p. 7.

(4) Rohatgi, K. K. Fundamentals of photochemistry 146.

(5) Rae, M.; Perez-Balderas, F.; Baleizao, C.; Fedorov, A.; Cavaleiro, J. A. S.; Tome, A. C.; Berberan-Santos, M. N. *J. Phys. Chem. B* **2006**, *110*, 12809–12814.

(6) Doose, S.; Neuweiler, H.; Sauer, M. *Chemphyschem* **2009**, *10*, 1389–1398.

(7) Thomas, K. G.; Ipe, B. I.; Sudeep, P. K. *Pure Appl. Chem.* **2002**, *74*, 1731–1738.

(8) Pal, S.; Dutta, P.; Wang, H.; Deng, Z.; Zou, S.; Yan, H.; Liu, Y. *J. Phys. Chem. C* **2013**, *117*, 12735–12744.

(9) Behera, M.; Ram, S. *Appl. Nanosci.* **2013**, *3*, 543–548.

(10) Wang, J.; Moore, J.; Laulhe, S.; Nantz, M.; Achilefu, S.; Kang, K. A. *Nanotechnology* **2012**, *23*, 1–13.

(11) Levi, S. a; Mourran, A.; Spatz, J. P.; van Veggel, F. C. J. M.; Reinhoudt, D. N.; Möller, M. *J. Chem. Eur.* **2002**, *8*, 3808–3814.

(12) Acuna, G. P.; Bucher, M.; Stein, I. H.; Steinhauer, C.; Kuzyk, A.; Holzmeister, P.; Schreiber, R.; Moroz, A.; Stefani, F. D.; Liedl, T.; Simmel, F. C.; Tinnefeld, P. *ACS Nano* **2012**, *6*, 3189–3195.

(13) Chhabra, R.; Sharma, J.; Wang, H.; Zou, S.; Lin, S.; Yan, H.; Lindsay, S.; Liu, Y. *Nanotechnology* **2009**, *20*, 5201.

(14) Clayden, J.; Greeves, N.; Warren, S.; Wothers, P. *Organic Chemistry*; Oxford University Press: New York, **2001**; p. 295.

(15) Uryga-Polowy, V.; Kosslick, D.; Freund, C.; Rademann, J. *Chembiochem* **2008**, *9*, 2452–62.

Chapter 6

Green fluorescent protein immobilization onto patterned gold nanoparticles templates

In this chapter we have been applying our proposed model composed of nano- and micro-patterned gold nanoparticles on the substrate which obtained in the previous chapters for green fluorescent protein immobilization.

Moreover, synthesis and characterization for thiolated NTA linker molecule that is needed for specific immobilization of green fluorescent protein (as described in chapter 1) will be described here as well.

Green fluorescent protein was chosen as a reliable model for biofunctional molecules in general and his-tag proteins in particular to be immobilized onto our previously prepared gold nanoparticles templates in order to prove the concept of this project.

1. Introduction

Green fluorescent proteins

Green fluorescent protein (GFP) is a protein consists of 238 amino acid residues, it produces green light as a result of energy transfer reactions upon exposure to blue light[1]. GFP has a cylindrical structure where the fluorophore is buried inside. This cylindrical shape composed of 11 strands of β-sheets from outside and α-helix from inside[2]. In general, GFP proteins have a number of attractive properties as being inert, stable and can be immobilized without having issues such as denaturation and consequently losing of its bioactivity[3] but still the most important value of GFP concerning their wide applications in fluorescence microscopy in which they used as specific markers to monitor single molecules / enzymes inside the biological systems. GFP shows dual reversible-switchable conformations either bright fluorescing or dark non-fluorescing conformation[4–6].

Förster resonance energy transfer (FRET)

It is a process for nonradiative energy transfer between two fluorophores; donor and acceptor through which energy transfer from donor fluorophore in its excited state to the acceptor one through dipole-dipole interaction[7,8]. FRET is an efficient technique for determining protein-protein interaction[9] as well as measuring small distances in the range of 1-10 nm inside the biological systems[10]. The performance of FRET technique was highly enhanced when it coupled with FP proteins acting as fluorophore donor-acceptor pair[11]. FRET results in decreasing the intensity of the donor fluorophore and increasing the intensity of the acceptor fluorophore[12]. The efficiency of FRET process is strongly dependent on the distance between donor and acceptor molecules, in which excitation spectra of the donor fluorophore should overlap with emission spectra with the acceptor fluorophore[3].

Fluorescence lifetime

Fluorescence lifetime is defined as the required time for a certain number of excited fluorophores to decrease exponentially to N/e by energy transfer processes. Number of parameters has a certain influence on fluorescence lifetime; such as the fluorophore structure, temperature, viscosity and polarity of the solvent, in addition to the presence of the fluorescence quenchers inside the solution.

These factors have a certain influence on encouraging the excited molecule relaxation through the non-radiative pathways.[10,13]

Fluorescence lifetime can be determined using number of techniques including time domain and frequency domain data acquisition methods[14].

Fluorescence decay kinetics of fluorophores

Fluorophores exhibit different fluorescence decay kinetics. While some fluorophores show single exponential decay kinetics, others show multiexponential decay kinetics.

Fluorophores with known lifetimes are essential tools which they are used as standards in testing and calibrating lifetimes-based instruments[14].

Fluorescence Lifetime Imaging Microscopy (FLIM technology)

This technique measures lifetime decay kinetics of fluorophores, thus, providing information not just on the nature of fluorophores themselves but rather on the fluorophores' environment[16,17]. Moreover, it is a sensitive indicator for a number of biophysical processes inside the biological systems such as conformational changes associated with proteins. FLIM technique coupled with FRET process has been implemented to monitor protein-protein interaction as well as to measure intramolecular distances with high spatial resolution up to few nanometers. This distance is the conventional distance between interacting proteins inside cells.

FLIM method can measure lifetime of individual fluorophores associated with protein molecules. (e.g. donor and acceptor fluorophore pair), therefore, it can efficiently provide quantitative information about their molecular interaction by estimating the efficiency of the energy transfer between the interacting fluorophores by means of measuring the changes in lifetime of both molecules[18].

Motivation for green fluorescent protein (GFP) immobilization onto nano- and micro-patterned gold nanoparticles templates

As described before, GFPs play an important role in fluorescence microscopy through their reversible switchable behavior between bright fluorescing and dark non-fluorescing conformations in addition to their ability to transfer energy among each other through FRET process. Therefore, the driving force behind green fluorescent proteins immobilization can be addressed in the following points:

(1) Allow to position fluorophores on a precise location with defined separation between each other onto a support matrix in order to resolve light coming out of individual fluorophores.

(2) Study the kinetics of single fluorophore attached to each protein molecule.

(3) Study energy transfer mechanism through FRET process between an individual pair of fluorophres.

(4) Probing the sensitivity of FLIM setup to measure fluorescence lifetime decay kinetics coming out of single excited fluorophore.

(5) Measuring the diffraction limit of the fluorophore through variations in the distance that separate each fluorophore from the adjacent one.

(6) The patterned GFP on the support matrix is expected to play a vital and central role in the fabrication of the optical devices. This will be achieved by employing the dual switching conformations of this peculiar protein (the light fluorescing and the dark non-fluorescing conformations).

GFP as a model system for biofunctional molecules immobilization

GFP protein is an excellent model to prove the concept of the current work (see chapter 1; the concept section) by its immobilization on Au NPs patterned substrates that its immobilization could be easily monitored through fluorescence microscopy techniques beside other techniques such as atomic force microscopy (AFM). Furthermore, it is not a hard work to check that the immobilization proceeds through immobilizing a single molecule per nanoparticles which is also one of the potential goals for this project.

Immobilization of GFP will take place through the synthesis of a specific linker molecule NTA-Ni(II) through which two kinds of functionalities are exist; thiol functionality from one side and NTA-Ni(II) complex from the other side.

Thiolated NTA will bind to gold nanoparticles on the substrate by means of thiol functionality. Immobilization of GFP is achieved by complexation reaction between Ni(II) ions with his-tags of GFP[19].

2. Experimental

The NMR spectra were taken using Bruker 400 MHz machine and $CDCl_3$ as a deuterated solvent.

Synthetic protocol for thiolated nitriolotriacetic acid (NTA-thiol linker)

The synthetic procedure for NTA-thiol linker molecule was conducted according to what has been reported before[20]; involving five steps preparation as described below:

*Synthesis of S-Acetyl-mercaptoundecanoic acid **(2)***

(2.5 g, 11.4 × 10^{-3} mol) of 11-mercaptoundecanoic acid was dissolved in (30 ml) of dichloromethane (CH_2Cl_2) before adding another (30 ml) of acetic acid. Right after that, (5.0 g) of zinc was added to the stirred reaction mixture. 20 minutes later, the reaction mixture was cooled down to (0 °C) in an ice bath prior the addition of (12 ml, 1.7 × 10^{-1} mol) of acetyl chloride. 1 hr. later, the ice bath was removed and the reaction was continued at room temperature for another 30 minutes. After that, the reaction was filtrated through celite to remove zinc from the solution. The filtrate was washed twice with (0.1 M) HCl mixed with ice, the organic phase was then separated, evaporated, and the crude product was recrystallized from ethanol to give (2.22 g, 75% yield). Ms (ESI) (m/z): [MH^+] 261.15. ^{1}H-NMR: δ(ppm): 2.79 (t, 2H, J = 0.019 Hz), 2.28 (t, 2H, J = 0.019 Hz), 2.26 (s, 3H), 1.60-1.45 (m, 4H), 1.28-1.20 (m, 12H). ^{13}C NMR: δ(ppm): 195.14, 178.00, 32.84, 29.63, 28.45, 28.34, 28.28, 28.14, 28.03, 28.00, 27.76, 23.65.

*Synthesis of S-Acetyl-mercaptoundecanoic acid-TEG-OH **(3)***

(1.4 g, 5.4 × 10^{-3} mol) of the purified product obtained in the previous step was dissolved in (30 ml) CH_2Cl_2 together with (8.07 g, 5.4 × 10^{-2} mol) triethylene glycol and (0.2 g, 1.62 × 10^{-3} mol) of DMAP under oxygen free atmosphere for 20 minutes. The reaction mixture was cooled to 0 °C in an ice bath before a solution of (1.23 g, 5.94 × 10^{-3} mol) of DCC in (10 ml) CH_2Cl_2 was added dropwise. The reaction was continued for another 1 hr. at 0 °C before ice bath was removed to let the reaction stir at room temperature for 20 hr. The reaction was filtrated and the filtrate was washed first with brine (3 × 35 ml), extracted from water and CH_2Cl_2 and dried over $MgSO_4$, filtrated and finally, evaporated to give a yellow oily crude product. The crude product was purified by silica column chromatography using ethyl acetate as an eluent and

the solvent was evaporated to give (2.08 g, 79% yield) as an oil product. Ms (ESI) (m/z): [MH^+] 393.23. ^{1}H-NMR: δ(ppm): 4.24 (t, 2H, J = 0.004 Hz), 3.71-3.60 (m, 10H), 2.86 (t, 2H, J = 0.018 Hz), 2.33-2.31 (m, 5H), 1.62-1.36 (m, 4H), 1.34-1.27 (m, 12H). ^{13}C NMR: δ(ppm): 196.06, 173.84, 72.52, 70.55, 70.33, 69. 19, 63.21, 61.71, 34.15, 30.63, 29.47, 29.37, 29.33, 29.20, 29.12, 29.08, 29.06, 28.77, 24.86.

*Synthesis of S-Acetyl-mercaptoundecanoic acid-TEG-imidazolide **(4)***

(0.123 g, 7.59 × 10^{-4} mol) of carbonyldiimidazole (CDI) was added to a stirred solution of (0.15 g, 3.82 × 10^{-4} mol) of S-Acetyl-mercaptoundecanoic acid-TEG-OH that obtained in the previous step dissolved in 10 ml DCM at room temperature. The reaction was incubated overnight. Finally, the solvent was evaporated under vacuum to produce white solid as a crude product. The product was then purified by recrystallization from ethyl acetate to yield 0.2 g (quant) of the desired product. Ms (ESI) (m/z): [MH^+] 487.25. ^{1}H-NMR: δ(ppm): 8.1 (s, 1H), 7.34 (t, 1H, J = 0.003 Hz), 6.96 (d, 1H), 4.44 (t, 2H, J = 0.012 Hz), 4.1 (t, 2H, J = 0.012), 3.72 (t, 2H, J = 0.012), 3.59-3.55 (m, 6H), 2.73 (t, 2H, J = 0.018 Hz), 2.21-2.18 (m, 4H), 1.51-1.42 (m, 4H), 1.24-1.11 (m, 12H)

*Synthesis of S-Acetyl-mercaptoundecanoic acid-PEG-NTA **(6)***

A solution of (0.85 g, 3.24 × 10^{-3} mol) Nα,Nα-methylcarboxy-$_L$-lysine (**5**) was dissolved in 10 ml of water. The pH of the solution was adjusted to 11.3 using concentrated NaOH solution. Another solution of (0.4 g, 8.22 × 10^{-4} mol) of product (**4**) was dissolved in 10 ml of DMF. The combined solution was left under stirring overnight at room temperature. 15 ml of water was added to the reaction mixture then the solution was extracted three times using ethyl acetate. The pH was adjusted to 1.7 for the aqueous phase using 0.1 M HCl. The solution was extracted for four times using ethyl acetate. The organic fractions were washed with saturated solution of NaCl and dried over anhydrous $MgSO_4$. Finally, the solution was filtrated and the organic solvent was evaporated by vacuum to yield 0.8 g (quant) of the product. Characterization results of the product have been currently being performed.

3. Results and discussion

3.1 Synthesis and characterization of thiolated NTA linker molecule

Many studies have been described a number of synthetic routes in order to prepare Ni-NTA molecule specific for binding to his-tag proteins. Here, we selected one of those routes as reported by Swartz *et. al*[20] and as indicated by Figure 76.

NTA molecule in this route was equipped by thiol functionality exploiting the high affinity and the strong interaction between thiol group and gold nanoparticles. Moreover, the molecule has the appropriate carbon chain length to provide the conjugated protein the required orientation to maintain its activity. Details for the individual steps involved in the synthesis will be described below.

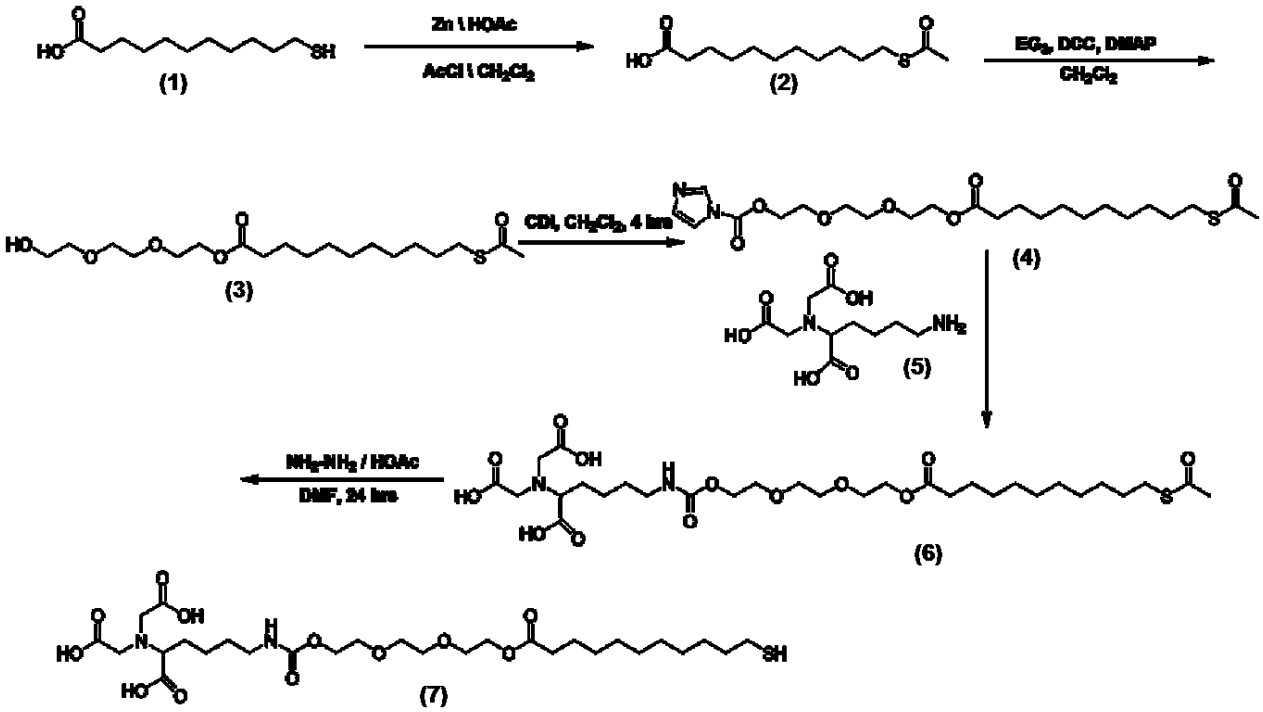

Figure 76: scheme illustrating the synthesis of NTA-thiol linker (7)

Synthesis of S-Acetyl-mercaptoundecanoic acid (2)

In this step, thiol group in the starting material of mercaptoundecanoic acid (**1**) was protected using acetyl chloride to generate the corresponding acetylated product (**2**). The reaction was catalyzed by zinc metal.

Synthesis and characterization of S-Acetyl-mercaptoundecanoic acid-TEG-OH (3)

The product obtained in the previous step was allowed to react with triethylene glycol acting as a spacer composed of three units of ethylene glycol. DCC and DMAP were used in the reaction to assist the coupling reaction between (2) and triethylene glycol spacer.

Synthesis of S-Acetyl-mercaptoundecanoic acid-TEG-imidazolide (4)

Nucleophilic addition reaction was employed between the compound obtained in the previous step and CDI to produce product number 4

The generated products were characterized using mass ^{1}H and ^{13}C NMR (details are given in the experimental part).

Synthesis of S-Acetyl-mercaptoundecanoic acid-PEG-NTA (6)

The reaction was performed as a consequence of nucleophilic addition reaction between Nα,Nα-methylcarboxy-$_{L}$-lysine (**5)** and the product obtained in the previous step. Characterization of this particular step is currently being performed in order to prepare the last step of NTA molecule.

Thereafter, a complexation reaction is supposed to take place between NTA ligand product (7) and Ni metal. The ligand will occupy four coordination sites of the metal.

As mentioned before, the value of NTA molecule will be to anchor GFP through its his-tag moiety guided by the high affinity of the imidazole group present in his-tag toward the metal center.

3.2 Immobilization of green fluorescent protein (GFP) onto nano- and micro-patterned gold nanoparticles surfaces (Outlook)

Essential elements required for GFP immobilization

Nano- and micro-patterned Au NPs templates

Substrates of nano- and micro-patterned Au NPs were prepared as described previously (see chapter 3 and chapter 4). These substrates composed of protein's binding sites (gold nanoparticles) in addition to the background substrates necessary for our immobilization strategy. As mentioned before, patterned Au NPs on the substrates were prepared with highly defined size, shape, position and arrangement, in addition to the extra manipulation of the support matrix (conductive silicon versus polyethylene glycol polymer).

Passivation of silicon substrates using polyethylene glycol (PEG) silane

Gold nanoparticles patterned on silicon substrates are going to be silanized using PEG silane molecules. The aim of this silanization is to prevent unspecific protein or linker molecule adsorption to the background substrate.

Synthesis of specific linker molecule for GFP immobilization

The necessity to synthesize the specific linker molecule as well as the followed synthetic pathway was described above.

Complex formation between NTA and Ni(II)

Chelation reaction is supposed to take place between nickel ions and NTA ligand. The tetradentate (NTA) ligand will occupy four coordinating sites of the metal ion.

GFP immobilization

This strategy of immobilization exploits the high affinity of divalent metal ion (Ni (II)) coupled with NTA spacer molecule toward the electron donor moieties exist in his-tag protein of the GFP (imidazole groups). His-tag protein interacts with Ni(II) through the remaining two unoccupied sites in the metal ion[21–23], thus forming an octahedral complex. Schematic representation of the different stages involved in the immobilization strategy is shown in Figure 77.

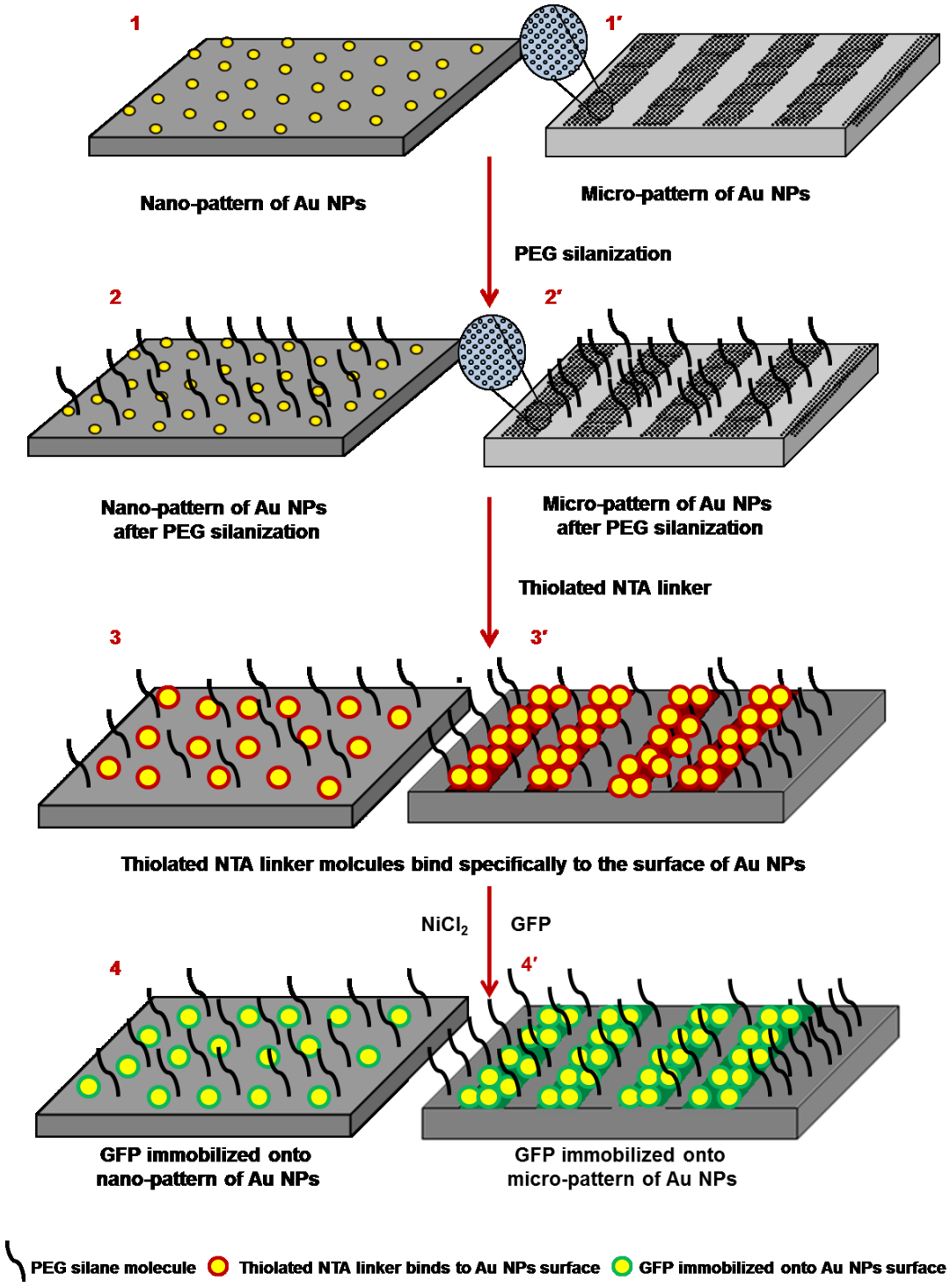

Figure 77: Schematic representation of GFP immobilization onto nano- and micro- patterned Au NPs

3.3 Novelty of green fluorescent protein immobilization onto the patterned gold templates

The novelty of the current work can be addressed in two main directions; the first direction involves the application of this immobilization strategy as a new technique for biofunctional molecules immobilization in general and GFP in particular (as mentioned in the concept part of this thesis).

The value of this strategy as mentioned before is to provide a platform where GFP can be immobilized specifically by its cofactor to the linker molecule that is conjugated to specific binding sites (gold nanoparticles) that reside on the support material. Moreover, the specific anchoring points on the substrate can protect the protein's active site by preventing the crowding effect which might influence on the spatial orientation of the biofunctional molecule and hence on its activity.

The second one will be addressed toward the potential applications of the immobilized GFP onto a support matrix (see the motivation of GFP immobilization in the introduction part of this chapter). These potential applications can encourage a large number of research work that would be performed based on this strategy.

4. Conclusion

Green fluorescent protein has been selected to represent biofunctional molecules in general and his-tag proteins in particular to be immobilized onto our previously prepared micro- and nano-patterned gold templates to prove the validity of our proposed immobilization strategy.

Thiolated Ni-NTA linker molecule specific for binding to his-tag proteins through Ni-NTA from one side and to gold nanoparticles through thiol functionality from the other side has currently been synthesizing in order to immobilize GFP onto our nano- and micro- gold templates.

Future outlook was addressed in GFP immobilization onto support matrix to be the first step toward a large number of potential applications and further research works exploiting the expected vital role of the immobilized GFP.

5. Bibliography

(1) Chalfie, M. GREEN FLUORESCENT PROTEIN. *Photochem. Photobiol.* **1995**, *62*, 651–656.

(2) Yang, F.; Moss, L. G.; Phillips, G. N. The Molecular Structure of Green Fluorescent Protein. *Nat. Biotechnol.* **1996**, *14*, 1246–1251.

(3) Takanishi, C. L.; Bykova, E. a; Cheng, W.; Zheng, J. GFP-Based FRET Analysis in Live Cells. *Brain Res.* **2006**, *1091*, 132–139.

(4) Weißenborn, J. Photon Emission of Nanostructures : Investigations on the Switching Behavior of the Protein rsTagRFP, 2012, p. 1,8,9.

(5) Brakemann, T.; Stiel, A. C.; Weber, G.; Andresen, M.; Testa, I.; Grotjohann, T.; Leutenegger, M.; Plessmann, U.; Urlaub, H.; Eggeling, C.; et al. A Reversibly Photoswitchable GFP-Like Protein with Fluorescence Excitation Decoupled from Switching. *Nat. Biotechnol.* **2011**, *29*, 942–947.

(6) Dedecker, P.; Hotta, J.; Flors, C.; Sliwa, M.; Uji-i, H.; Roeffaers, M. B. J.; Ando, R.; Mizuno, H.; Miyawaki, A.; Hofkens, J. Subdiffraction Imaging through the Selective Donut-Mode Depletion of Thermally Stable Photoswitchable Fluorophores: Numerical Analysis and Application to the Fluorescent Protein Dronpa. *J. Am. Chem. Soc.* **2007**, *129*, 16132–16141.

(7) Duncan, R. R. Fluorescence Lifetime Imaging Microscopy (FLIM) to Quantify Protein-Protein Interactions Inside Cells. *Biochem. Soc. Trans.* **2006**, *34*, 679–682.

(8) Festy, F.; Ameer-Beg, S. M.; Ng, T.; Suhling, K. Imaging Proteins in Vivo Using Fluorescence Lifetime Microscopy. *Mol. Biosyst.* **2007**, *3*, 381–391.

(9) Hanson, M. R.; Köhler, R. H. GFP Imaging: Methodology and Application to Investigate Cellular Compartmentation in Plants. *J. Exp. Bot.* **2001**, *52*, 529–539.

(10) Berezin, M. Y.; Achilefu, S. Fluorescence Lifetime Measurements and Biological Imaging. *Chem. Rev.* **2011**, *110*, 2641–2684.

(11) Subach, F. V; Zhang, L.; Gadella, T. W. J.; Gurskaya, N. G.; Lukyanov, K. A.; Verkhusha, V. V. Red Fluorescent Protein with Reversibly Photoswitchable Absorbance for Photochromic FRET. *Chem. Biol.* **2010**, *17*, 745–755.

(12) Ingenieurwissenschaften, D. Der. Long-Term Observation of Living Cells by Wide-Field Fluorescence Lifetime Imaging Microscopy. **2011**.

(13) Hrdlovic, P.; Donovalova, J.; Stankovicova, H.; Gaplovsky, A. Influence of Polarity of Solvents on the Spectral Properties of Bichromophoric Coumarins. *Molecules* **2010**, *15*, 8915–8932.

(14) Boens, N.; Qin, W.; Basaric, N.; Hofkens, J.; Ameloot, M.; Pouget, J.; Lefevre, J.; Valeur, B.; Cedex, F.-P.; Gratton, E.; et al. Fluorescence Lifetime Standards for Time and Frequency Domain Fluorescence Spectroscopy. *Anal. Chem.* **2007**, *79*, 2137–2149.

(15) Kuwana, E.; Sevick-muraca, E. M. Fluorescence Lifetime Spectroscopy in Multiply Scattering Media with Dyes Exhibiting Multiexponential Decay Kinetics. *Biophys. J.* **2002**, *83*, 1165–1176.

(16) Suhling, K.; French, P. M. W.; Phillips, D. Time-Resolved Fluorescence Microscopy. *Photochem. Photobiol. Sci.* **2005**, *4*, 13–22.

(17) Bravaya, K. B.; Khrenova, M. G.; Grigorenko, B. L.; Nemukhin, A. V; Krylov, A. I. Effect of Protein Environment on Electronically Excited and Ionized States of the Green Fluorescent Protein Chromophore. *J. Phys. Chem. B* **2011**, *115*, 8296–8303.

(18) Krishnan, R. V.; Masuda, A.; Centonze, V. E.; Herman, B. Quantitative Imaging of Protein-Protein Interactions by Multiphoton Fluorescence Lifetime Imaging Microscopy Using a Streak Camera. *J. Biomed. Opt.* **2003**, *8*, 362–367.

(19) Lukac, R.; Kauerova, Z.; Masek, J.; Bartheldyova, E.; Kulich, P.; Koudelka, S.; Korvasova, Z.; Plockova, J.; Papousek, F.; Kolar, F.; et al. Preparation of Metallochelating Microbubbles and Study on Their Site-Specific Interaction with rGFP-HisTag as a Model Protein a a. *Langmuir* **2011**, *27*, 4829–4837.

(20) Swartz, J. D.; Gulka, C. P.; Haselton, F. R.; Wright, D. W. Development of a Histidine-Targeted Spectrophotometric Sensor Using Ni(II)NTA-Functionalized Au and Ag Nanoparticles. *Langmuir* **2011**, *27*, 15330–15339.

(21) Patel, J. D.; O'Carra, R.; Jones, J.; Woodward, J. G.; Mumper, R. J. Preparation and Characterization of Nickel Nanoparticles for Binding to His-Tag Proteins and Antigens. *Pharm. Res.* **2007**, *24*, 343–352.

(22) Celia, H.; Wilson-Kubalek, E.; Milligan, R. a; Teyton, L. Structure and Function of A Membrane-Bound Murine MHC Class I Molecule. *Proc. Natl. Acad. Sci. U. S. A.* **1999**, *96*, 5634–5639.

(23) Mattiasson, B.; Kumar, A.; Ivanov, A. E.; Galaev, I. Y. Metal-Chelate Affinity Precipitation of Proteins Using Responsive Polymers. *Nat. Protoc.* **2007**, *2*, 213–220.

Abstract

The current project comprises the synthesis and characterization of different morphologies of metal nanoparticles (e.g. gold nanoparticles). These morphologies range from spherical nanoparticles to more complex one, such as one, two and three dimensional nanostructures, in addition, to hollow urchin-like nanoparticles.

The different morphologies of metal nanostructures possess interesting physical properties indicated by the position of their localized surface plasmon resonance (LSPR) peak which appears in the visible to near IR region depending on the size, shape and composition of the nanostructure. Furthermore, metal nanoparticles show high chemical affinity toward specific chemical functionalities namely; thiol and amine. While thiol functionality tends to form strong and stable binding to metal nanoparticles, amine shows weak and reversible binding.

The characteristic chemical features of those nanoparticles allow them to self-assemble onto amino functionalized silicon substrate. Further functionalization of those nanoparticles with specific linker molecule through thiol moiety from one side and double bond from the other side to be crosslinked with polyethylene glycol prepolymer under UV-light, allows their facial transference from silicon surface to the surface of PEG polymer. This strategy aims to create specific binding sites composed of different morphologies and compositions of nanostructures to anchor biofunctional molecules on a protein repellent background.

The ultimate objective of this work is to generate a number of nano- and micro-patterned gold nanoparticles templates for controlled and selective immobilization of biofunctional molecules.

Nano-pattern of gold nanoparticles was fabricated onto two dimensional conductive silicon substrate by “Block copolymer micelle” nanolithography with highly defined size, position and interparticle distances. The nano-pattern was then transferred to the surface of PEG polymer using simple bench top technique and without aid of any linker molecule by employing the swelling property of PEG hydrogel as a driving force for the transference process.

Moreover, micro-pattern of gold nanoparticles on silicon was achieved by a novel method that combines μ-contact printing approach with self-assembly to produce

micro-stripes of gold nanoparticles. While, the coverage of the nanoparticles is high within the micro-pattern, the nanoparticles were rarely found in the areas in between.

Furthermore, micro-pattern of a composite material composed of Au NPs and PEG beside other areas of PEG was fabricated using Fill Molding In Capillaries of a PEG replica mold to obtain a micro-pattern of gold nanoparticles in three dimensional substrate. While gold nanoparticles serve as protein's binding sites within the composite matrix, PEG hydrogel in the adjacent areas act as protein's non-adhesive surface.

As a model of fluorophore's containing biofunctional molecules, an organic dye composed of fluorescein moiety were functionalized with an appropriate linker molecule. The linker shows selective binding to the surface of gold nanoparticles through thiol functionality, where the length of the linker was carefully adjusted to decrease fluorescence quenching that would result as a consequence of direct binding between the fluorophore and gold surface. The model aims to investigate our ability to resolve fluorescence light coming out of the adsorbed fluorophore on the nanoparticles.

Green fluorescent protein was selected to represent biofunctional molecules to be immobilized onto our nano- and micro-patterned gold nanoparticles surfaces by getting the advantage that its immobilization event could be monitored through fluorescence microscopy. To achieve this goal thiolated nitrilotriacetic acid molecule (NTA) is being synthesized for specific binding to gold nanoparticles through thiol group. NTA-Ni(II) will reside at the other end of the linker for selective binding to his-tag protein in GFP. This concept of GFP immobilization is currently being worked on.

Acknowledgements

I would like to express my deepest gratitude and sincere appreciation to my supervisor Prof. Marga C. Lensen for her direct supervision, encouragement, support and endless patience throughout the course of my Ph.D. Thanks also for the members of the examination committee for their valuable discussion.

Love and thanks to my parents, brothers, sisters and my friends either here in Germany or in Jordan for their encouragement and support.

I should like to express my gratitude to Dr. Axel Löbus for his valuable instructions and contribution in the AFM imaging and Gonzalo de Vicente Lucas for his intensive collaboration as well as his fruitful discussion.

Moreover, I owe thanks to my master student Cigdem Yesildag for her significant contribution throughout the course of this work.

Special thanks go to Mr. Christoph Fahrenson for his big effort in performing SEM measurements.

Great thanks are also extended to the following:

- Dr. Anna Fischer and her group for their intensive support and collaboration.

- All the people who helped in the instrumental measurements throughout the course of this work.

- Casey Daniels and Maysoon Saleh for their help in the English corrections.

- Yilmaz Aksu for his valuable support.

- All LLab members for their wonderful friendship during the past three years.

I would like also to address my gratitude and appreciation to UniCat, BIG-NSE office, and “Durchstarterstipendium” for their financial support, in particular, Prof. Reinhard Schomäcker for his tremendous support as a former head of BIG-NSE as well as to Dr. Jean-Philippe Lonjaret as a managing director for BIG-NSE.

List of Publications

[1] Raid J. Abdel-Jalil*, **Manar M. Arafeh**, Sirin A. I. Adhamc and Wolfgang Voelter, Synthesis of 2-(aryl diazenyl)-[1H]-3-methylbenzo[g]indoles and their Activity Against Various Tumor Cell Lines (submitted to Monatshefte fuer chemie)

[2] Raid J. Abdel-Jalila*, Musa S. Shongwea, **Manar M. Arafeh**, Cäcilia Maichle-Mößmerc, Gabriele Kociok-Köhnd, and Wolfgang Voeltere, 1-(Naphthylamino)-1-(p-chlorophenylhydrazono)-2-propanone and 2-(p-tolyldiazenyl)-[1H]-3-methylbenzo[g]indole: Crystallographic and Spectroscopic Elucidation of the Cyclisation of an Arylamidrazone (submitted to the Journal of Molecular structure).

[3] Jingyu Chen, **Manar Arafeh**, Diana Felkel, Axel Loebus, Susan Kelleher, Anna Fischer, Marga Lensen*, Hybrid Hierarchical Patterns of Gold Nanoparticles and Poly(Ethylene Glycol) Microstructures, *J. Mater. Chem. C*, **1**, 7709-7715 (2013)

[4] Zhenfang Zhang‡, Axel Loebus‡, Gonzalo de Vicente, **Manar Arafeh** and Marga C. Lensen*, In situ Formation of Novel Poly(ethyleneglycol)-based Hydrogels via Amine-Michael type Addition with Tunable Mechanics and Chemical Functionality (submitted to chemistry of materials)

[5] Jingyu Chen, Vera Schulte, Yibing Hu, **Manar Arafeh**, Amandine Guiet, Axel Loebus, Petra Mela, Diana Felkel, Anna Fischer, Susan Kelleher, Marga Lensen*, Adhesion and Spreading of Cells on PEG with Imbedded Patterns of Gold Nanoparticles (*Manuscript in preparation*).

[6] **Manar Arafeh**, Gonzalo de Vicente, Axel Loebus and Marga C. Lensen*, Embedded Micro-pattern of PEG – Gold Nanoparticles Composite Hydrogel for Biomedical Applications (*Manuscript in preparation*)

[7] **Manar Arafeh**, Cigdem Yesildag and Marga C. Lensen*, Transference of Different Shapes of Gold and Silver Nanoparticles from Silicon Substrate to the Surface of Polyethylene Glycol Hydrogel (Manuscript in preparation)

[8] **Manar Arafeh**, Marga C. Lensen, Synthesis and Characterization of Fluorescein-based Derivatives (in preparation)

[9] Cigdem Yesildag, **Manar Arafeh** and Marga C. Lensen*, Micro-pattern of gold nanoparticles on silicon using micro-contact printing approach. (in preparation)

[10] Loebus A+, Zhang Z+, Li Q, Strehmel C, Wisniewski W, **Arafeh M**, Rüssel C, Su Z, Lensen M. C. 3D Patterned Reactive Mineralized Poly(ethylene glycol) Derived Hydrogels. (in preparation)

Contribution to Scientific Conferences

Poster contributions

[1] Micro- and Nano-patterned Surfaces for Selective Immobilization of Enzymes. Manar Arafeh, Jingyu Chen, Amandine Guiet, Axel Löbus, Diana Felkel, Zhenfang Zhang, Gonzalo de Vicente Lucas, Susan Kelleher, Anna Fischer and Marga C. Lensen. 13th Dresden Polymer Discussion and 8th Max Bergmann Symposium– "MOLECULAR BIOENGINEERING MEETS POLYMER SCIENCE" 2012, Dresden.

[2] Micro- and Nano-patterned Surfaces for Selective Immobilization of Enzymes. Manar Arafeh, Amandine Guiet, Axel Löbus, Gonzalo de Vicente Lucas, Diana Felkel, Zhenfang Zhang, Anna Fischer and Marga C. Lensen. Tag der Chemie 2012, Berlin.

[3] Transference of Different Shapes of Gold and Silver Nanoparticles from Silicon to the Surface of Polyethylene Glycol Hydrogel. Manar Arafeh, Cigdem Yesildag and Marga C. Lensen. WE-Heraeus-Seminar on Micro- and Nano-structured Interfaces for Biological and Medical Research 2013, Bad Honnef.

Manar M. Arafeh

Address: Haus Nr. 220302- Willdenow Straße 23 –Wedding 13353- Berlin-Germany
Mob: +49 1782542747**;** e-mail: manararafeh@yahoo.com, manar@mailbox.tu-berlin.de
Date and place of Birth: 8. January. 1983, Amman - Jordan

Education:

Dates	Description
Apr. 2011-Jan. 2014	**Ph.D student:** Technische Universität Berlin, BIG-NSE - UniCat Group of Prof. Lensen "Micro-and Nano-patterned gold structures for Selective Immobilization of Proteins''
Oct. 2005-Aug. 2007	**M.Sc. Organic Chemistry:** Hashemite Univ.-Zarqa-Jordan Group of Prof. Abdel-Jalil Synthesis of some 2-(aryldiazenyl)-[1H]-3-methylbenzo[g]indoles
Oct. 2001-June 2005	**B.Sc. Chemistry:** Hashemite Univ.-Zarqa-Jordan
Sep. 1999- Aug. 2001	**High School Diploma** "Tawjihi" Sukayna Bent Al-Hussain Secondary School

Work Experience:

Dates	Job description	Place
Nov. 2007 – Feb. 2008	Research assistant in organic chemistry laboratory	German - Jordanian Univ.
Nov. 2008 – Sep. 2009	Lab supervisor	Jarash Private Univ.
Sep. 2009 – Sep. 2010	Chemical analyst	Water Authority drinking water dep.

Teaching Experience:

October 2005 – August 2007

Chemistry labs supervision (organic, analytical and inorganic chemistry labs, Hashemite University, Zarqa, Jordan

November 2008 – September 2009

Chemistry labs supervision (organic, analytical and physical chemistry labs), Jarash Private Univ, Jarash, Jordan